The Effect of Fluid Viscosity on Hydrocyclone Performance

Design and Commissioning of an Experimental Rig and Results

Svein-Arne Marthinussen

Master Thesis Process Technology

Department of Physics and Technology
University of Bergen

July 2011

Acknowledgements

First I would like to thank my supervisor Professor Alex C. Hoffmann for his guidance through this thesis, and Dr. Weiming Peng from Aker Process Systems for his guidance with the experimental setup. I also want to thank PhD student Yu-Fen Chang for providing the initial equipment that was necessary to start the assembly of the experimental setup.

Thank to Associate Professor Jarle Sidney Diesen at Bergen University College for the help with equipment and materials, and thank to Therese Fjæreide from FMC BioPolymer for providing the alginate used in this thesis.

During the assembly of the experimental setup, Leif Egil Sandnes at the Mechanical Workshop at the University of Bergen provided excellent help, and his effort is highly appreciated. I also want to thank my dad, Atle Marthinussen, who helped me with some of the assembly, and also provided some of the equipment needed for the experiments.

I want to thank my fellow Master students at the University of Bergen. Especially the discussions with my fellow student Daniel Gilje Fonnes were highly appreciated.

Finally I would like to thank my fiancé Carina Sandnes who has been a great support during this thesis, taking extra care of our two children at home, and for encouragement when needed.

Abstract

Hydrocyclones are used in the process industry for a variety of applications. The product streams from the wells in the oil and gas industry include produced sand, which have to be removed as it interferes with control and instruments. There is also an environmental concern, which includes regulations for the content of hydrocarbons in the disposed sand.

The existing knowledge of sand separation by cyclonic technology is largely limited to the separation from pure water. The future oil industry, however, faces challenges with heavy oil and non-standard particles. If the oil is heavy, the water-oil separation is poor and the sand therefore needs to be removed from a liquid phase with a considerable content of heavy oil. How the oil content will affect the cyclone performance is not understood or theoretically described.

This thesis is mainly focused on solid removal from viscous liquids. An experimental rig has been designed and commissioned, and results from both experiments and CFD are presented. The results from this thesis include not only the affection of the fluid viscosity on the separation performance. It includes results for the pressure drop, and also the flow split distribution that we have when the hydrocyclone is operated with an underflow.

As the viscosity of the carrier fluid increase, the separation efficiency decreases. The same is the situation with the pressure drop across the cyclone. When the viscosity of the fluid increase the pressure drop is reduced which is the opposite of what we would expect related to normal pipe flow. The by-pass ratio, which is the amount of suspension that exits through the apex of the cyclone, is increased at higher viscosities.

The results from this thesis are highly valuable for the process industry. Even though more experiments are needed to fully understand the phenomena's described in this thesis, it is a leap in the direction of applying cyclonic technology in new areas. If the sand can be removed in a controlled and automated manner, the process systems can be operated with better control and safety. The lifetime of the equipment can be prolonged and allowing more sand to enter the production train can speed up the production.

Contents

List of Figures

List of Tables

List of Symbols

$\mathbf{a}$	acceleration vector; components a_i	m s^{-2}
a	width of tangential inlet	m
b	height of tangential inlet	m
c	velocity of sound in fluid	m s^{-1}
c	concentration	varies
C	constant	varies
C_D	drag coefficient	
D	diameter	m
D_i	inlet diameter for cylindrical cyclone inlet	m
D_o	overflow diameter, vortex finder diameter	m
D_u	underflow diameter, apex diameter	m
d_{50}	cut size	m
E	optimum efficiency	
Eu	Euler number, $\Delta p / (1/2 \rho \langle v_z \rangle)$	
f	frequency	s^{-1}
F	cumulative undersize distribution function	
$f(\cdot)$	differential density distribution function	m^{-1}
$\mathbf{F}_D$	drag force vector; components F_i	N
$\mathbf{g}$	gravitational acceleration (abs. value g)	m s^{-2}
h	height	m
H	height, distance below surface of suspension	m
I	length of cylindrical section of cyclone body	m
k	number of samples being combined	
K_1	constant	
L	length of cyclone body	m
L	length of path, ultrasonic signal	m
m	mass	kg
M	mass of solids	kg
n	number of experiments	
p	pressure	Pa
Q_s	volumetric rate of solids	m^3 s^{-1}
Q	volumetric flow rate	m^3 s^{-1}
r	radial coordinate	m
R_f	underflow-to-throughput ratio	
Re_p	particle Reynolds number, $\rho_l \lVert \mathbf{U}' \rVert x / \mu$	
s	empirical standard deviation	varies
s^2	empirical variance, pooled variance with subscript p	varies
S_f	relative density of fluid	

Stk	Stokes number $(\Delta\rho x^2 v_{ch})/(18\mu D)$	
t	time	s
T	temperature	°C
$T_{BA,AB}$	transit time from B to A and A to B	s
U	underflow rate	$m^3\ s^{-1}$
u	fluid velocity	$m\ s^{-1}$
$\mathbf{U}'$	particle velocity relative to fluid; components U'	$m\ s^{-1}$
v	fluid velocity	$m\ s^{-1}$
v_θ	tangential velocity	$m\ s^{-1}$
v_t	tangential velocity	$m\ s^{-1}$
v_t	terminal velocity	$m\ s^{-1}$
v_r	radial velocity	$m\ s^{-1}$
v_z	axial velocity	$m\ s^{-1}$
$\langle v_z \rangle$	mean axial velocity	$m\ s^{-1}$
x	particle diameter	m
x_{50}	cut size	m
$x_{25,75}$	reference to 0.25, 0.75 fractional efficiencies, respectively	
$\bar{x}$	mean value	varies
y	wall distance	m
z	axial coordinate	m
ε	porosity	
$\dot{\gamma}$	shear rate	s^{-1}
η	overall fractional separation efficiency	
η	Kolmogorov length scale	m
$\eta\,(\cdot)$	grade-efficiency	
$\eta'\,(\cdot)$	reduced grade-efficiency	
η'	reduced fractional separation efficiency	
λ	particle size, diameter	m
μ	viscosity	$kg\ m^{-1}\ s^{-1}$
θ	tangential coordinate	
θ	gap angle	◦
ρ	fluid density	$kg\ m^{-3}$
ρ_l	liquid density	$kg\ m^{-3}$
ρ_p	particle density	$kg\ m^{-3}$
σ	true standard deviation	varies
σ^2	true variance	varies
τ_v	shear stress	$N\ m^{-2}$
Ω	angular velocity	s^{-1}
$\|\cdot\|$	absolute value	

Part I

Background and Introductory Material

Chapter 1

Introduction

1.1 Relevance

The oil and gas industry supplies oil and gas to a world depending on hydrocarbons. Different factors like increased oil recovery has made it possible to operate the wells much longer than what was possible back in the days when the production had just started. Another important thing that has changed is the way we protect our environment. The limits of discharge are becoming stricter and will continue to do so in the coming years.

Disposal to the sea is restricted by international agreements and national laws and regulations (OSPAR, EU regulations, White Papers, Pollution Control Acts etc). For sand discharge to the sea, the amount of oil in the sand is defined by the Petroleum Safety Authority. On the Norwegian continental shelf, the content of formation oil in the solid particles discharged must be less than 10 g per one kg of dry mass [1].

The presence of solid particles in the process effects more than the environmental concerns. Produced solids create a number of problems for the process industry, which will be discussed later in this thesis. These problems get worse as the wells gets older.

Finding a way to automatically remove sand and other solids from the organic liquids in a controlled manner will make a difference concerning the problems present today. It opens a possibility for washing the sand for environmentally friendly disposal, prolonging equipment lifetime and reduces the downtime. In addition it avoids health problems related to the manual removal of sand from vessels.

1.2 Technological Background

Cyclones are used for a various number of applications in the process industry. The cyclone itself has no moving parts, and for operation there is only need for an external pump. Further advantages are that it is cheap, compact and versatile. The cyclones that are specially designed for liquids are often referred to as hydrocyclones, hydraulic cyclones or hydroclones.

This thesis is a part of a research project called “Solid Separation from Highly Viscous Liquids by Cyclone Technology”, also referred to as the “CLEANSAND” project. The CLEANSAND project is a part of the Petromaks Programme, “Environmental Technology for the future”.

The existing knowledge about sand separation by the use of cyclonic technology in the oil and gas industry is largely limited to the separation from pure water. The on-

going research project aims to apply basic knowledge about the separation of sand from liquids such as heavy crude oil and Mono-ethylene glycol, also for the case when mixed with water. This thesis aims to get knowledge about the separation performance on such systems. If the separation performance in these systems are known and is satisfactory, the current technology for sand washing can be applied for a much wider range of applications. The CLEANSAND project is a co-operation between the University of Bergen (UoB) and Aker Kværner Process Systems (AKPS).

The problems caused by sand will increase in the future as the wells get older and more sand is produced. In addition to the environmental concerns and restrictions, the sand creates a variety of problems for the oil and gas industry. Some examples are mentioned below:

- The solids interfere with control and instruments, reducing safety and reliability of the system significantly.
- Erosion reduces the lifetime of the equipment. Substantial risk is faced if combined corrosion-erosion problems occur.
- Valves are clogged, reducing the operational capability, safety and reliability.
- Separation tanks are filled with sand, reducing firstly the retention time for the separation and eventually resulting in a shutdown of the separators for manual sand removal.
- Sand can create problems for injection wells and injection pumps.

The possibility to remove sand in a controlled and automated manner will grant the process systems with better control and safety. It will increase the lifetime of the equipment and allowing more sand to enter the production train can speed up the production rate. If the sand is washed it can be discharged to the sea without affecting the surrounding ecosystem. The wells produce more water and sand as they get older, and as a consequence the sand issue will be a big problem for the oil industry in the future.

Current technology available for sand washing can reach the required purity by using produced water with approximately 2000 ppm oil in water. The common practice today is to neglect the oil content and perform calculations and testing for the sand separation from pure water. This limits the liquids from which sand separation can be achieved to water with small oil content and light oils. The problem with this is that the oil industry faces challenges in the future with heavy oils and non-standard particles. If the oil is heavy and has a density close to that of water, the water-oil separation is poor and the sand therefore needs to be removed from a liquid phase with a considerable content of heavy oil. The effect of the heavy oil content on the cyclone performance is not understood or theoretically described. The effect of different types of solids on the separation performance of a cyclone will be investigated in the CLEANSAND project.

Sand is present in the gas processing industry. To avoid problems with hydrates in gas production, hydrate inhibitors such as Mono-ethylene glycol (MEG) is injected in the pipelines [2]. Sand enters the production train for MEG separation together with the water-MEG phase. To remove sand and/or corrosion products from the water-MEG phase, the cyclone performance on such systems needs to be studied, and this is one of the targets in this thesis.

1.2.1 Approaches, Hypotheses and Choice of Method

The CLEANSAND project is divided into two experimental setups. This thesis includes experimental work on a full-scale hydrocyclone rig with abilities to measure velocity, pressure distribution and particle distribution in the feed and the two product streams. The other setup consists of a smaller and simpler rig, namely a "PET rig", where the main objective is to find the particle trajectory through the cyclone. The PET (Positron Emission Tomography) rig has the possibility of measuring pressure and velocity in the system. Experiments done on the PET rig are made in collaboration with Haukeland University Hospital and their Centre of Nuclear Medicine / PET, Department of Radiology.

Centrifugal separation of sand from viscous liquids is a complex process, and the research group working on this project is of that opinion that the research can best be empirically driven. To gain representative results for this thesis an experimental setup is used to predict the cyclone performance.

1.2.2 Industrial Applications

Hydrocyclones have a wide number of applications in the industry, and it belongs among the most applied separation equipment in current technology. They are used to separate two phases in a liquid medium in different industries like mineral processing [3], chemical industry [4], environmental industry [5], sewage treatment [6], food engineering [7] and others. It is employed in liquid clarification, slurry thickening, solids washing, liquid degassing, solids classification or sorting based on density or particle shape. The simple design and low investment cost together with low cost for operation and maintenance makes it favorable for many applications in today's industry.

1.2.3 Cyclone History

Bretney [8] obtained the first cyclone patent in 1891, and this cyclone was the forerunner to the de-sanders used today to separate sand from water in pressurized systems. Even though a number of patents were obtained in the following years, the first recorded use of a cyclone was by a U.S. phosphate plant in 1914 [9]. Since then the cyclone has been introduced to a number of new applications, and this thesis is aiming to extend the applications even further.

Chapter 2

Theory

2.1 Forces in Swirling Flow

"Swirling flow, or vortex flow, occurs in different types of equipment, such as cyclones, hydrocyclones, spray dryers and vortex burners." [10] Two types of ideal swirling flows are:

1. Forced vortex flow, i.e. swirling flow with the same tangential velocity distribution as a rotating solid body.

2. Free vortex flow, i.e. the way a frictionless fluid would swirl. "The tangential velocity in such a swirl is such that the moment-of-momentum of fluid elements is the same at all radii." [10]

If we first imagine that the swirling fluid has an infinite viscosity, no shearing motion exists between fluid layers at different radii. For this case, the fluid elements at all radial positions are forced to have the same angular velocity, Ω. The angular velocity is measured in radians per unit of time and, and therefore has units s^{-1}. It equals v_θ/r, with v_θ the tangential velocity, measured in m/s. Swirl with constant angular velocity is called forced vortex flow or solid body rotation:

$$v_\theta = \Omega r \tag{2.1}$$

For the other extreme, we will assume that the swirling fluid has no viscosity. In this case neighboring elements at larger and smaller radii does not influence the motion of a given fluid element. Bringing an element to a smaller radius will increase its tangential velocity in order to conserve its moment-of-momentum (mass times tangential velocity times radius of rotation, $mv_\theta r$ [10]). A vortex where the moment-of-momentum is conserved in this way is called a loss free- or frictionless- vortex. For this case we have $rv_\theta = C$, with C as a constant, so that:

$$v_\theta = \frac{C}{r} \tag{2.2}$$

The quantities v_θ, Ω and r are actually vectors since they have both magnitude and direction. In this section, however, we are only interested in their magnitudes. For that reason we dispense with the vectorial notation.

In the previous mentioned, we had a look on two ideal flow patterns derived from the fundamental equations of fluid mechanics [10]. A real fluid will have some finite viscosity. This will cause transfer of moment-of-momentum between layers at different radii. Transport of moment-of momentum will also be caused by any turbulence present, due to exchange of fluid elements between the layers.

In a real swirling flow, there is normally a core of near solid-body rotation surrounded by a region of near loss-free rotation, as sketched in Figure 2.1. A vortex that behaves like this is called a Rankine vortex.

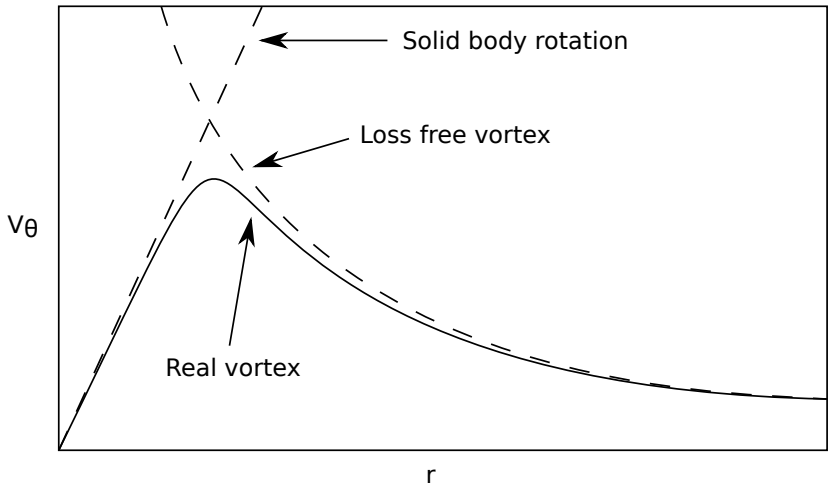

Figure 2.1: Sketch showing the two ideal vortex flows, and the tangential velocity distribution in a real vortex.

2.1.1 Centripetal Force

If we consider a fluid element in a swirling flow using a cylindrical coordinate system (r, θ, z) with the axis of rotation pointing out of the paper, the element will accelerate towards the center as it rotates [10]. An illustration of the forces acting is shown in Figure 2.2. If the fluid element did not accelerate it would continue in a linear path tangent to the orbit toward the axis of rotation. The acceleration towards the center of rotation is known as the centripetal acceleration.

The conclusion from this is that there is a velocity change, i.e. acceleration, and therefore a force acting towards the center of rotation, which is known as the centripetal force [11].

2.1.2 Centrifugal Force

If we then observe the fluid element from a coordinate system, which is not fixed in space by rotating with the element, the centripetal acceleration mentioned before will not longer be observed [10]. It will appear as an apparent force directed away from the axis of rotation and the force is known as the centrifugal force. The centrifugal force is similar to the gravity force and has a magnitude equal to the mass of the element times the centripetal acceleration. Since Newton's equation of motion only applies on a coordinate system that is not accelerating, the centrifugal force is strictly speaking not a real force. However, for mathematical simplicity an accelerating coordinate system is

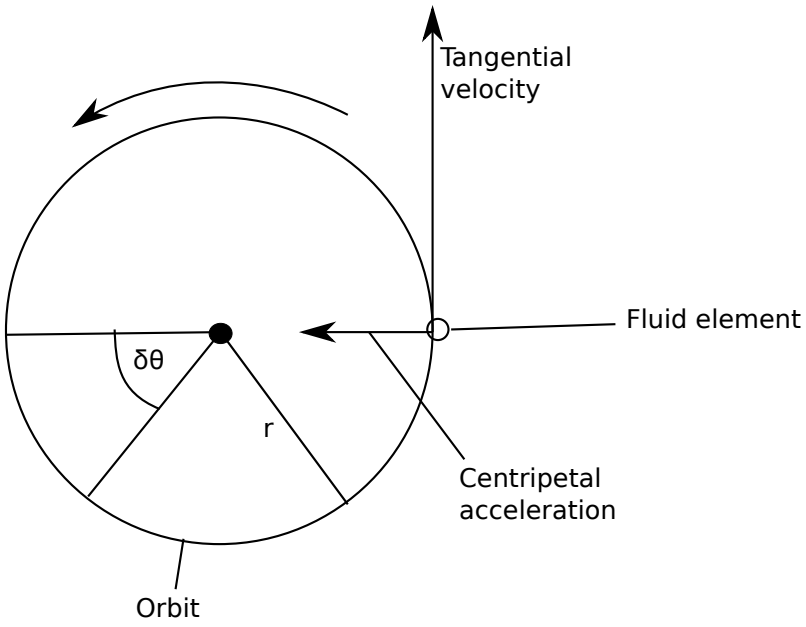

Figure 2.2: The centripetal acceleration acting on a fluid element in orbit around an axis z.

used in order to apply or preserve the equation of motion. We are then speaking of a non-physical or a pseudo force such as the centrifugal force.

For a fluid element, the centrifugal force is balanced by a force created by a gradient in the static pressure. The pressure gradient force is pointing towards the center of rotation and an illustration of the forces acting on the element is given in Figure 2.3.

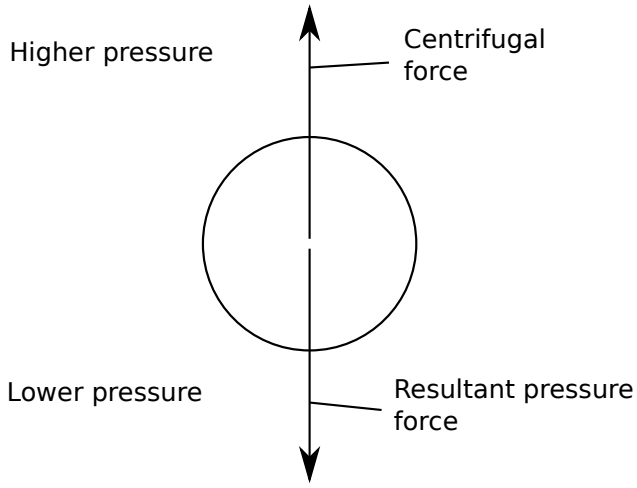

Figure 2.3: Forces acting on a rotating fluid element in a rotating coordinate system.

2.2 How Hydrocyclones Work

Hydrocyclones work as a result of the centrifugal forces acting on suspended particles in the swirling liquid stream [11]. Unlike centrifuges, which use the same principle, the hydrocyclones separates without the need of mechanically moving parts. The only equipment needed is a pump, and the necessary vortex motion is induced by the fluid itself. If the particles have a higher density than the liquid, they move outward to the hydrocyclone wall, at which they are transported downwards to the apex of the hydrocyclone. The cleaned liquid together with some of the finest particles is discharged through the vortex finder, which acts as an outlet tube for the overflow.

A typical hydrocyclone consists of a cylindrical section at the top, and a lower part shaped like a cone. These parts are joined together, and the suspension of particles in the liquid is injected tangentially through the inlet opening in the upper part. Because the suspension enters tangentially, a strong swirling motion is developed within the cyclone. This action contributes to the development of the inertial forces that enables classifications of the particles within the hydrocyclone [12]. The suspension is then further accelerated in the conical part and due to this a low-pressure vortex appears in the center of the hydrocyclone. The relatively light particles might migrate into this vortex, and are removed with the overflow stream by an upward swirling flow through the vortex finder. The heavier particles are as mentioned before removed by the downward swirling flow through the apex of the hydrocyclone. A sketch of a hydrocyclone of conventional design is given in Figure 2.4:

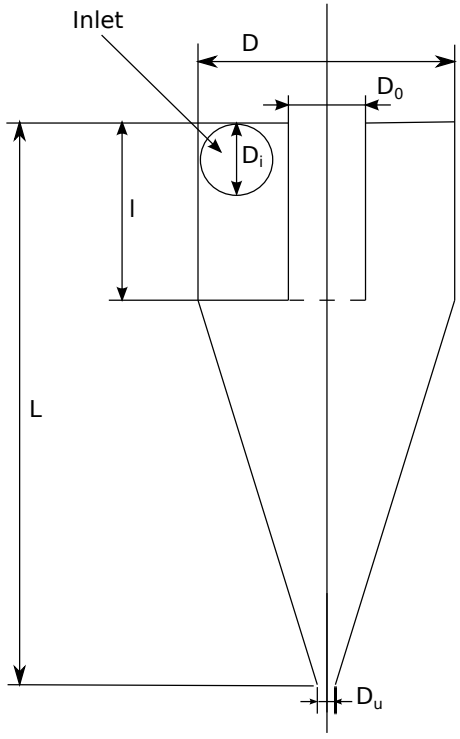

Figure 2.4: A hydrocyclone of conventional design, where L is the length of the cyclone body, I is the length of the cylindrical section, D is the diameter of the cylindrical section, D_i is the inlet diameter and D_o and D_u is the diameter of the overflow and underflow outlets respectively.

2.2.1 Merits and Disadvantages

As stated by Svarovsky [13]: "The relative merits of hydrocyclones can be summarized as follows:

1. they are extremely versatile in application in that they can be used to clarify liquids, concentrate slurries, classify solids, wash solids, separate two immiscible liquids, degas liquids or sort solids according to density or shape;

2. they are simple, cheap to purchase, install, and run, and require little in the way of maintenance and support structures;

3. they are small relative to other separators, thus saving space and also giving low residence times, which gives them an advantage in terms of the speed of the sedimentations classifiers for example;

4. the existence of shear forces in the flow is an advantage in classification of solids because it breaks any agglomerates, and also in the treatment of thixotropic and Bingham plastic slurries.

The disadvantages of hydrocyclones may be listed as follows:

1. they are somewhat inflexible once installed and operated, giving low turndown ratios due to the strong dependence of their separation performance on flow rate and feed concentration; they are also inflexible due to their general sensitivity to instabilities in feed flow rate and solids concentration;

2. there are limitations on their separation performance in terms of the sharpness of the cut, the range of the cut size, dewatering performance or the clarification power; some of these characteristics may be improved in multistage arrangements, but at additional costs of power and investment;

3. they are susceptible to abrasion but steps can be taken to reduce abrasive effects;

4. the existence of shear may sometimes turn into a disadvantage because flocculation cannot be used to enhance the separation as in the case of gravity thickeners (as most flocs do not survive the shear)."

2.3 Liquid Flow Pattern

The swirling motion that is induced inside the hydrocyclone due to the tangential feeding position gives a downward pointing vortex in the outer region and an upward pointing vortex in the inner region. This phenomena has led to some misunderstanding regarding the direction of the rotation for the downward going and the upward going vortices respectively. Some people claim that the spirals rotate in opposite directions, which is not correct. The reversal only applies to the vertical component of the velocity and the spirals are therefore rotating in the same direction [14].

With the exception of the region in and just around the tangential inlet duct, the flow pattern inside a hydrocyclone has a circular symmetry [13]. The velocity of the flow

can at any point within the cyclone be resolved into three components. They are known as the tangential velocity ν_t, the radial velocity ν_r and the vertical or axial velocity ν_a, and all three of them can be investigated separately. Experimental data from literature with values obtained by Kelsall as quoted by Svarovsky [13] are shown in Figures 2.5, 2.6 and 2.7.

Keeping in mind that the flow pattern inside a hydrocyclone varies with many factors regarding the geometry, it is important to stress that the following short account of velocity profiles in a hydrocyclone is only qualitative. The flow patterns in a hydrocyclone are highly complex, and it may be incorrect to assume that precisely similar profiles occur in cyclones with a considerably different geometry or for liquids of high viscosity.

2.3.1 Tangential Velocity

Below the rim of the vortex finder, the tangential velocity ν_t increases considerably with decreasing radius down to a given radius, which is smaller than the exit radius of the vortex finder [13]. This is displayed in Figure 2.5. The relationship can be described by:

$$\nu_t r^n = \text{constant} (\text{where } n \text{ is normally } 0.6 \leq n \leq 0.9) \tag{2.3}$$

As the radius is further decreased, the tangential velocity decreases and is proportional to r. This relationship holds until the cylindrical air column (which normally forms in a hydrocyclone discharging at atmospheric pressure [14]) is reached. Above the rim of the vortex finder, the break in the rise of ν_t occurs at a larger radius than below the rim. This can be seen in Figure 2.5. Apart for this phenomenon and wall effects, the tangential velocity is independent of the vertical position. This gives envelopes of constant tangential velocity as cylinders coaxial with the cyclone.

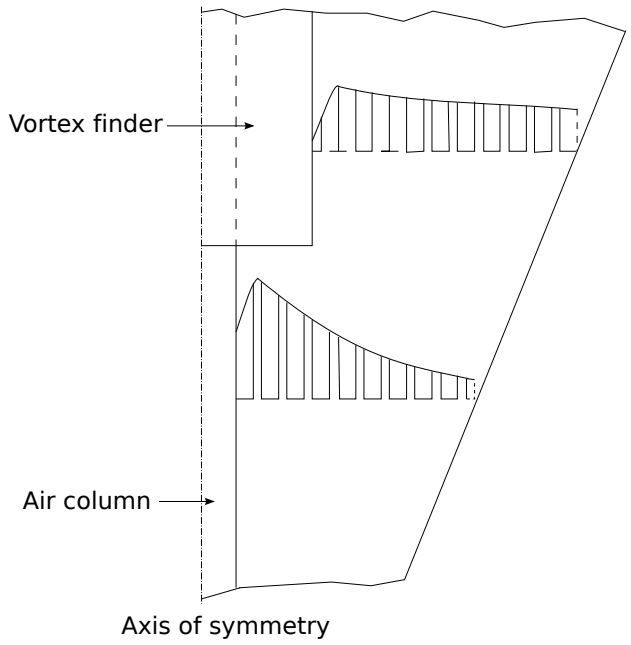

Figure 2.5: Tangential velocity distribution in a hydrocyclone.

2.3.2 Axial Velocity

Figure 2.6 shows that there is a strong downward flow along the outer walls of the cyclone. This is essential for the separation since it is the dominant mechanism for removing the collected particles that have been separated into the underflow orifice [10]. For this reason it is not essential to build the cyclone with the apex pointing downwards and the efficiency of the cyclone is only very little influenced by its position relative to the gravity field.

The downward flow is partially counterbalanced by an upward flow in the core region [13]. This is depending on the underflow-to-throughput ratio, which we will get back to later. Figure 2.6 shows a well-defined locus of zero vertical velocities (LZVV), which follows the profile of the cyclone. The latter is further described in section 2.3.6.

Above the rim of the vortex finder the largest downward velocities are located near the cyclone wall as for the lower part. The axial velocity becomes upward at a radii between the cyclone wall and the vortex finder. Figure 2.6 also show that strong downward flow can be found around the vortex finder. This is due to wall-induced flow, which runs inward along the top of the cyclone.

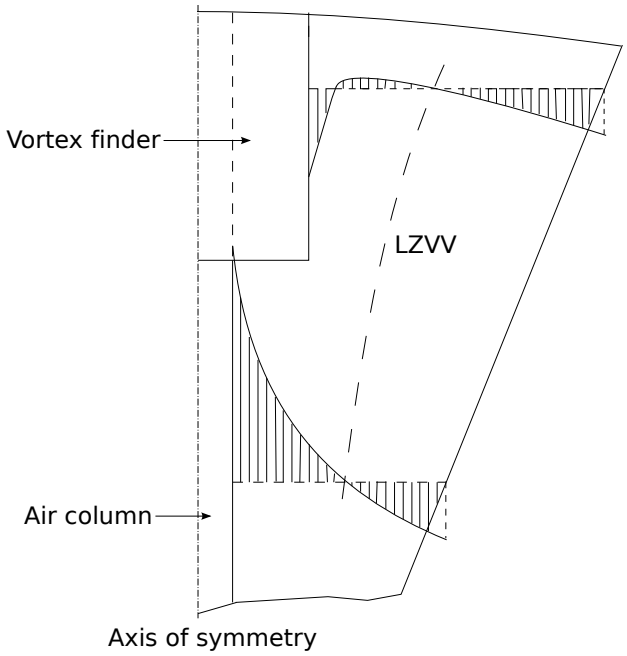

Figure 2.6: Vertical (axial) velocity distribution in a hydrocyclone. LZVV, the locus of zero vertical velocity.

2.3.3 Radial Velocity

The radial velocity components are difficult to measure accurately as they are much smaller than the other two components [13]. The radial velocity is inward and as Figure 2.7 shows its magnitude decreases with decreasing radius. Since the radial velocity is difficult to measure, the position of zero radial velocity is not known.

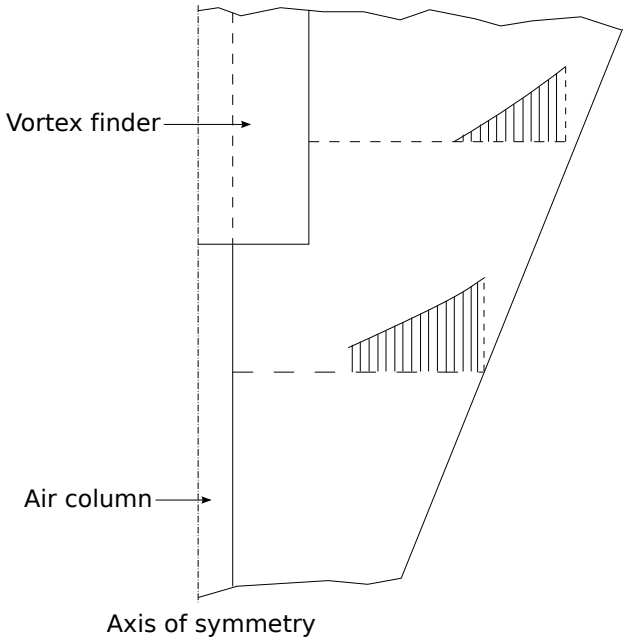

Figure 2.7: Radial velocity distribution in a hydrocyclone.

2.3.4 Short Circuit Flow

Some of the feed that enters the cyclone can pass directly across the roof of the cyclone and into the overflow stream within the vortex finder [14]. The flow path across the roof exists due to obstruction of tangential velocity and happens due to regions of lower pressure near the cyclone walls together with the lower pressure in the inner regions. The flow that follows this pattern is called short circuit flow. Because of this phenomenon there is need for a pipe that enters some distance into the cyclone as an outlet for the overflow. An illustration of this phenomenon can be found in Figure 2.8.

2.3.5 Eddy Flows

The flow inside the hydrocyclone is divided into the inner and outer vortex. This is brought into detail in section 2.3. Some of the flow in the inner vortex will recirculate [14]. This happens because the vertical flow upward in the cyclone can exist in the region outside of the outer wall of the vortex finder. The flow that passes the outer wall of the vortex finder exist in the form of a recirculating eddy or eddies. Eddy flows can be caused by the inability of the vortex finder opening to cope with the natural up flow in the vortex. An illustration of Eddy flows can be found in Figure 2.8.

2.3.6 The Locus of Zero Vertical Velocity

Inside the cyclone there is a flow going downward in the outer region and a flow going upward in the inner region [14]. Since these flows moves in opposite vertical direction, there is a position between these flows where there is no vertical velocity. The locus of zero vertical velocity can be traced, and applies throughout the majority of the cyclone. An illustration of the locus of zero vertical velocity is given in Figure 2.6.

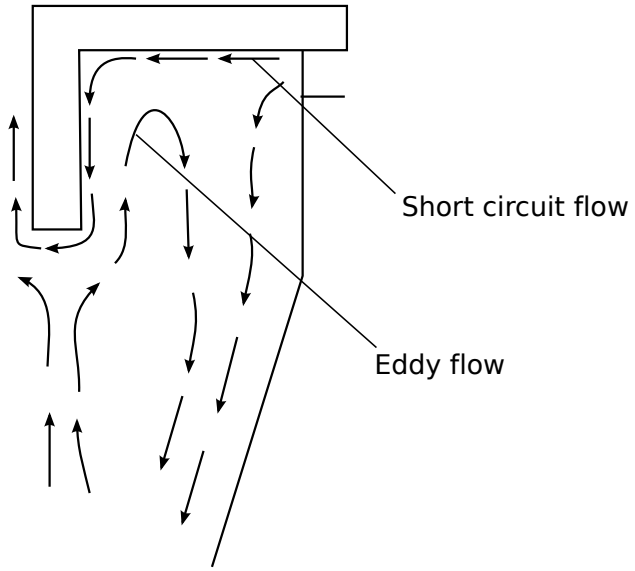

Figure 2.8: Schematic representation of the short circuit and eddy flows.

2.3.7 The Air Core

Rotation of the fluid in a cyclone creates an axial core of low pressure. In the case of the hydrocyclone, this normally results in a free liquid surface, and according to Bradley [14] the formation of the air core is an indication of vortex stability. If the core in the cyclone communicates directly with atmosphere at either of the outlets, the core becomes air filled. In the case where there is no communication with atmosphere the core can still exist in form of vapor and gases from components in the liquid.

2.4 Cyclone Pressure Drop

The most used method for measuring a pressure drop in the process industry is to measure the static pressure at the wall in the upstream and downstream piping [10]. For a hydrocyclone case this is complicated because there is a swirling flow pattern in the exiting liquid. The swirling flow causes the static pressure at the wall to be higher than the cross-sectional average, and we need to think of how to deal with the dynamic pressure stored in the swirling motion. To understand the pressure drop we therefore need to have a closer look on the two pressure contributes, namely the static and the dynamic pressure.

We can recognize the static and the dynamic pressure from the well-known Bernoulli equation for a steady flow of a frictionless fluid [15] given in Equation (2.4):

$$\frac{p}{\rho} + gh + \frac{1}{2}v^2 = \text{constant along a streamline} \tag{2.4}$$

The first term on the left hand side represents the static pressure while the third term represent the dynamic pressure where the latter is often called the velocity head. In the Bernoulli equation they are both divided by the fluid density. We know the static pressure as p and the dynamic pressure as $1/2\rho v^2$. Equation (2.4) shows that the static and the dynamic pressure can be interchanged in the flow field. That means that in

areas where the velocity is high the static pressure will be low and the opposite the other way.

As the liquid moves inward from the outer to the inner region of the vortex inside the cyclone body, it is accelerated in order to conserve the moment-of momentum or angular momentum, as someone would call it [10]. This makes the static pressure lower, while the dynamic pressure increase. For a given velocity at the wall, a smaller frictional loss gives a more intense vortex. The more intense the vortex is, the more efficient is the conversion and it gives a lower central static pressure with which the liquid enters the vortex finder. A smooth walled cyclone therefore produce the highest spin in the vortex, and gives the greatest decrease in static pressure within the core.

The permanent pressure drop over the cyclone is just like in normal pipe flow due to dissipation of mechanical energy. Energy stored as dynamic pressure in the tangential velocity component in the liquid entering the vortex finder is dissipated there and in the downstream piping. This happens without much recovery of the static pressure. Normally the pressure drop over the cyclone is subdivided into three contributions:

- Losses at the inlet
- Losses in the cyclone body
- Losses in the vortex finder

For a cyclone with a tangential inlet the losses at the entry are often negligible compared to the other contributions. The losses in the cyclone body are higher, but its main contribution is reduction of the swirl intensity, as we will come back to later. Losses at the walls in the cyclone do therefore not dominate the overall pressure drop.

The losses in the vortex finder are the largest for the tangential inlet cyclones [10]. It may be in the order of magnitude larger than the contributions from the inlet and the cyclone body due to the dissipation of the mechanical energy mentioned earlier. There are however some exceptions to this, where one of them is the case with a high solid loading. At that case frictional drag at the walls can become a significant contribute to the pressure drop at the expense of losses in the vortex core, and the vortex finder.

Increased solid loading and wall friction are expected to increase the pressure drop over the cyclone as our experience with normal pipe flow indicates that increased wall friction leads to increased frictional loss and a higher pressure drop. This is not the case for a cyclone. By using some of the previous mentioned about the cyclone pressure drop contributions it can be seen that this is expected.

To describe why an increased wall friction leads to a decreased pressure drop we will look at two extremes for the flow pattern in the cyclone body:

- An intense vortex with very low frictional wall loss, and
- High wall losses due to wall friction in the body causing almost complete attenuation of the swirling motion.

For the first case a large amount of static pressure is transformed into dynamic pressure. This leads to a high swirl dynamic pressure that dissipates in the vortex finder and the downstream piping. For the other case, friction at the walls takes away all the dynamic pressure from the inlet reducing the spin to almost zero in the cyclone body.

The dissipation in this case can be in the order of magnitude less than for the first case and the fluid will therefore enter the vortex finder at a much higher static pressure. From this it can be seen that the dissipation of mechanical energy, and therefore also the pressure drop is higher for the first case.

This means that rougher walls gives a lower pressure drop in a cyclone. Using this it is therefore not that difficult to understand that wall solids, in cases where the solid loading is high, also reduces the overall pressure loss relative to the cases where the solid loading is negligible. When the fluid contains a large amount of solids, drag between the solid and the fluid robs the fluid for much of its energy. This gives reduction in both the velocity of the core spin and the static pressure loss.

To sum up some of the above, it can be said that increased wall friction leads to a reduction in core spin velocity and a reduction of the overall pressure drop. However, as a general rule we want to keep the walls as smooth as possible since this leads to the highest core spin velocity, and the best separation performance due to a higher centrifugal force exerted on the particles.

The factors mentioned above contribute to the challenge of interpretation of the cyclone pressure drop. For the inlet pressure there is normally not a problem as the static pressure is fairly uniform over the cross section, and can be measured by a pressure tapping in the wall. Interpreting the pressure measured at the outlet is what causing the challenge due to any swirl still present at the point of the pressure tapping. Hoffmann and Stein [10] states that: "One way out of these difficulties is the observation that the static pressure at the wall is close to the cross-sectional mean of the static pressure plus the dynamic pressure stored in the swirl." This means that it is equal to the static pressure that would be measured after a flow straighter device that would convert all the dynamic swirl pressure into static pressure.

In the absence of a pressure recovery device the pressure measured at the wall at the outlet piping minus the static pressure measured at the inlet gives the true dissipative losses in the cyclone body. We still need to remember that the dynamic swirl may dissipate also after this point due to friction at the walls, bends and more.

2.4.1 Euler Number

For process equipment with turbulent flow the pressure drop is proportional or at least close to proportional to the volumetric flow rate [10]. Hydrocyclones are no exception to this rule, and to obtain a characteristic measure for the pressure drop in a given cyclone, the pressure drop is often reported in a dimensionless form known as the Euler number. The definition of the Euler number is given in Equation (2.5):

$$Eu := \frac{\Delta p}{\frac{1}{2}\rho \langle v_z \rangle^2} \tag{2.5}$$

Where $\langle v_z \rangle$ is the mean axial velocity in the cyclone body, i.e. the volumetric flow rate divided by the cross-sectional area of the cylindrical section of the cyclone body [10]. The Euler number is useful to plant engineers who wish to estimate the pressure drop through a cyclone in their system at conditions that differs from the design conditions. This number can be obtained from dimensional analysis, and it is used in empirical relationships to relate the quality of separation achieved relative to the cost. The last detail is further described in section 2.8.2, Stokes-Euler Relationships.

2.5 Motion of Suspended Particles

We will here start with a general discussion on the motion of solid particles in a fluid and focus on the particle motion in swirling flows towards the end of this section.

In a hydrocyclone, the particles of interest are almost always moving relative to the liquid at their terminal velocity, and the terminal velocity of a given particle determines whether the particle will be captured or lost. The terminal velocity that we are talking about here is exactly analogous to that of a particle settling in the earth's gravitational field, g, under steady state conditions [10]. There is however one exception. For a hydrocyclone, the radially directed centrifugal force, mv_θ^2/r replaces the gravitational one.

Applying Newton's law to a particle moving in a fluid, equating its mass times acceleration to the sum of the forces acting on it, gives:

$$\begin{pmatrix}\text{mass}\\ \text{times}\\ \text{acceleration}\end{pmatrix} = \begin{pmatrix}\text{body}\\ \text{force}\end{pmatrix} + \begin{pmatrix}\text{fluid}\\ \text{drag}\end{pmatrix} + \begin{pmatrix}\text{unsteady}\\ \text{force}\\ \text{terms}\end{pmatrix}$$

where the body force is normally due to a gravitational field and/or a centrifugal force. As mentioned earlier, the term centrifugal force is strictly speaking not a real force. That means that the above force balance is being performed in a reference coordinate system that is rotating with the particle. The fluid drag represents the drag acting on a particle that moves with a steady velocity relative to the fluid, while the unsteady terms account for the effect of acceleration of the particle relative to the fluid [10]. By making appropriate substitutions in the above expression, the general equation of motion for a particle in a Newtonian fluid becomes [16]:

$$\left(\frac{\pi x^3}{6}\right)\rho_p\frac{d\mathbf{U}'}{dt} = \left(\frac{\pi x^3}{6}\right)(\rho_p-\rho_l)\,\mathbf{a} - C_D\left(\frac{1}{2}\rho_l\mathbf{U}'\left\|\mathbf{U}'\right\|\right)\left(\frac{\pi x^2}{4}\right) - \begin{pmatrix}\text{added}\\ \text{mass}\end{pmatrix} - \begin{pmatrix}\text{Basset}\\ \text{term}\end{pmatrix} \tag{2.6}$$

where $\mathbf{U}'$ is the velocity vector of the particle relative to the fluid with cylindrical coordinate components (U_r', U_θ', U_z'). $\mathbf{a}$ is the acceleration vector of an external force field, ρ_p and ρ_l are the densities of the particle and the liquid respectively, and t is time. $\|\cdot\|$ denotes the absolute value of the vector, i.e. the length of the vector. The diameter of the particle is denoted by x.

The first term on the right-hand side represent the body force, while the second term represents the drag $\mathbf{F}_D$ acting on a particle when the flow around it is fully developed. C_D is the drag coefficient. The unsteady forces due to acceleration of the relative velocity can be divided into two parts: the virtual mass effect and the Basset force [17]. These are the two last terms on the right-hand side of Equation (2.6).

When a body is accelerated through a fluid, there is a corresponding acceleration of the fluid surrounding the body. This appears to add mass to the particle. The Basset term accounts for the viscous effects. It addresses the temporal delay in the boundary layer development as the relative velocity changes with time [17]. The added mass and the Basset term are zero in steady movement.

Clift et al. [16] showed that ignoring these unsteady terms can lead to errors for a rapidly changing motion in a liquid. According to Hoffmann and Stein [10], it turns

out that these unsteady terms can be ignored both for the case of a gas cyclone and a hydrocyclone, as practical plant experience with their design and operation indicates that it is not necessary to include either of the terms.

The particle Reynolds number is given by [10]:

$$Re_p := \frac{\rho_l \, \|\mathbf{U}'\| \, x}{\mu} \tag{2.7}$$

where μ is the viscosity of the fluid. When the particle Reynolds number is low, the equations of motion for the fluid moving around the particle can be solved, and $\mathbf{F}_D$ calculated. If there is no slip between fluid and particle surface, i.e. the fluid velocity is equal to the velocity of the surface at the surface [10], the result is Stokes drag law [15]:

$$\mathbf{F}_D = -3\pi x \mu \mathbf{U}' \tag{2.8}$$

By using Equation (2.7) and comparing the expression for the fluid drag in Equation (2.6) and (2.8), we see that $C_D = 24/Re_p$, which is the particle's drag coefficient in laminar flow. Ignoring the unsteady terms and substitution for the fluid drag in Equation (2.6) gives the following equation of motion for the particle:

$$\left(\frac{\pi x^3}{6}\right) \rho_p \frac{d\mathbf{U}'}{dt} = -3\pi x \mu \mathbf{U}' + \left(\frac{\pi x^3}{6}\right) (\rho_p - \rho_l) \, \mathbf{a} \tag{2.9}$$

When the particles enter near the cylindrical wall they can be dispersed inwards because of the intensive turbulent mixing in the feed section. There is, however, very little information of the behavior of the liquid in the cylindrical section of the cyclone. This portion of the cyclone is normally treated as a preliminary separation zone, and the main separation are thought to be performed in the conical lower section of the cyclone [13].

Particles that enter the separation space are influenced by an inward directed drag and an outward directed centrifugal force. The separation space starts at the point where the incoming fluid first experiences rotation and the solids carried along by the fluid first experiences a centrifugal force acting radially outwards [10]. Where the separation space starts is influenced by the design of the inlet and it may for example start at the leading edge of an inlet scroll. This is further described later under design variations.

The size of the particles is very important when describing how they will be influenced by the rotational flow pattern. The centrifugal force is proportional to the particle mass, and therefore also the cube of the particle diameter:

$$m = \rho \times \frac{\pi}{6} \times x^3 \tag{2.10}$$

The drag force, which is due to the flow of liquid from the outer to the inner part of the vortex, is when Stokes law applies proportional to the particle diameter. Stokes law often applies in practice and for this reason the largest particles are therefore the easiest to separate.

It is not easy to study the particle flow pattern inside a hydrocyclone experimentally. Particle trajectories are therefore often described as a result of CFD simulations where the particles are injected from different locations at the inlet into a precalculated flow field.

2.5.1 Particle Size

The motion of the particles flowing inside a hydrocyclone obviously depends on its size among the other important things such as density and tangential velocity. Since size plays such an important role, it is important to have some knowledge about how the particle size is defined before moving on to the separation efficiency which clearly is depending on which method used.

The shape of the particles is often irregular, and to obtain a general size that is independent of the particle shape, the size of the particles are often defined as one of the following [10]:

- The volume equivalent diameter, i.e. the diameter of a sphere with the same volume as the actual particle.
- The surface equivalent diameter, i.e. the diameter of a sphere with the same surface area as the actual particle.
- The surface/volume equivalent diameter, i.e. the diameter of a sphere with the same surface to volume ratio as the actual particle.

Choosing the correct dynamically equivalent diameter is very important when the performance of a hydrocyclone is to be evaluated. There is a challenge to this when we are in the range of intermediate Reynolds numbers, or when the Cunningham correction is significant. In regions where Stokes' drag law is valid it is called the Stokesian diameter. Stokes' law often applies in practice, and when it does it can relate the particle size to the Stokes' diameter. The Stokes' diameter is defined as:

$$Stk := \frac{\Delta\rho x^2 v_{ch}}{18\mu D} \tag{2.11}$$

2.6 Separation Efficiency

When using a hydrocyclone to separate a mixture of two phases, where the liquid phase is the most abundant, the cyclone is generally operated with a certain underflow [18]. This means that if a certain hydrocyclone is operated with a given suspension, there will still be two variables. That is the throughput and the ratio of underflow-to-throughput. Increasing the throughput leads to increase in the pressure drop. This again usually leads to improved separation while the separation curve shifts to smaller particle sizes.

The ratio of underflow-to-throughput influences the separation efficiency for two reasons. If the ratio is very small while the concentration of solids in the feed is high, the underflow may not have the capacity to remove all solids. This leads to an increase of the solid concentration within the cyclone, and the solids are entrained partly with the overflow. Tengbergen and Rietma [18] states that: "The minimum total amount of underflow necessary is equal to the amount of solids separated plus the total amount of liquid which is entrained in the pores between the solids even when these solids are closely packed". From this the optimum efficiency obtainable is limited by:

$$E = \frac{U(1-\varepsilon)}{Q_s} - \frac{U\varepsilon}{Q - Q_s} \tag{2.12}$$

Where U is the underflow rate, Q_s is the volume rate of solids in the feed, ε is the minimum porosity of the concentrated solids and Q is the throughput of the cyclone.

In the case where the cyclone does not separate at all, there will still be a certain amount of solids that are removed by the underflow. The ratio of the solids removed is equal to that of underflow to throughput. The result form this is that there always exist a by-pass with a quantity of solids equal to the amount of original feed corresponding to the liquid underflow. Therefore the optimum efficiency which, can be obtained is also limited by:

$$E = 1 - \frac{U - Q_s}{Q - Q_s} \tag{2.13}$$

2.6.1 Total Efficiency

There are three particle fractions that we are concerned with in hydrocyclone operations. That is the feed, the collected or underflow and the lost particles in the overflow. The overall efficiency is calculated as the mass fraction of the feed solids captured by the cyclone [10, 19]. There are three material streams involved, and if there is no accumulation of solids in the separator, an overall mass balance is applicable. If we represent the feed, the underflow and overflow by the symbols M_f, M_u and M_o respectively the mass balance for solids over the cyclone is:

$$M_f = M_u + M_o \tag{2.14}$$

The total efficiency η can therefore be calculated as the mass fraction of feed solids captured by the cyclone:

$$\eta = \frac{M_u}{M_f} = 1 - \frac{M_o}{M_f} = \frac{M_u}{M_u + M_o} \tag{2.15}$$

The efficiency is calculated by collecting samples and weighing two of the fractions. The total efficiency is usually what counts the most in an industrial process, though it does not give a good measure for characterizing the intrinsic separation performance of a particular cyclone. For example it tells nothing about the ability to separate particles of a given size.

2.6.2 Reduced Total Efficiency

As already stated in section 2.6, certain applications in solid-liquid separation include the effect of flow splitting. In the case of a hydrocyclone the feed is divided into an underflow and an overflow. Since this guaranteed efficiency is present it is desirable to consider the separation effect alone. Referring to Svarovsky [19] the best and most widely used definition for this is the so-called reduced efficiency η':

$$\eta' = \frac{(\eta - R_f)}{(1 - R_f)} \tag{2.16}$$

where R_f is the underflow-to-throughput ratio. R_f is defined as:

$$R_f = \frac{U}{Q} \tag{2.17}$$

Equation (2.16) satisfies the requirement that the efficiency for the separation is zero, when no separation takes place ($\eta = R_f$), and unity for complete separation.

2.6.3 Grade-Efficiency

For a hydrocyclone the separation efficiency is depending on the particle size. The Grade-efficiency is defined in a similar way as the total efficiency, but it differs in the way that it corresponds to one particle size only, or a narrow range of particle sizes [10, 19]. The grade-efficiency curve is a continuous function of particle size x. The following derivation is a reproduction from Hoffmann and Stein [10] and shows how the grade-efficiency is determined.

If the differential volume or mass density distributions of the feed, the underflow and the overflow fractions are $f_f(x)$, $f_u(x)$ and $f_o(x)$ respectively, the mass balance for particles with the diameter between $x - 1/2dx$ and $x + 1/2dx$ is:

$$f_f(x)dx = \eta f_u(x)dx + (1-\eta)f_o(x)dx = dF_f(x) = \eta dF_u(x) + (1-\eta)dF_o(x) \tag{2.18}$$

To simplify this, let us approximate the particle size differential with a finite, yet small value for dx, and substitute in some numbers obtained from a hypothetical hydrocyclone performance measurement:

We assume:

- 10% of the feed solids (by wt. or vol.) lie within a 5-micron (Δx) band centered about some particular particle size, x.
- Measurements show that 80% of the particles within this particular 5-micron band are collected and that they comprise 6% of the collected material.
- 20% of the particles are lost and they comprise 26% of the emitted solids.

The finite approximation to the left three terms of Equation (2.18) then reads:

$$0.10 \times 5 = 0.80 \times 0.06 \times 5 + (1 - 0.80) \times 0.26 \times 5 \tag{2.19}$$

cancelling the Δx's (i.e. the 5's):

$$0.10 = 0.048 + 0.052 = 0.10 \tag{2.20}$$

Equation (2.18) can be integrated term-by-term to provide a mass balance for the particles with a size less than a given size x:

$$F_f(x) = \eta F_u(x) + (1-\eta)F_o(x) \tag{2.21}$$

Given that the grade-efficiency is defined as the fraction of the feed solids with a diameter between $x - 1/2dx$ and $x + 1/2dx$ that is captured in the hydrocyclone:

$$\eta(x) = \frac{M_u f_u(x)dx}{M_f f_f(x)dx} \tag{2.22}$$

Using Equation (2.15) and the mass balances in Equations (2.18) and (2.21) gives:

$$\eta(x) = \eta\frac{f_u(x)}{f_f(x)} = 1 - (1-\eta)\frac{f_o(x)}{f_f(x)} = 1 - (1-\eta)\frac{dF_o(x)}{dF_f(x)} \tag{2.23}$$

The grade-efficiency curve can be obtained by feeding the separator with mono-sized solids in several batches [19], or by using a feed of polydisperse material containing particles in the required size range. The latter is the quickest and cheapest way. Regardless of what method chosen the total efficiency must me calculated and for the case with the polydisperse material the size distribution from two of the material streams must be analyzed.

When calculating a grade-efficiency curve from the total efficiency and the cumulative size distributions of the feed and the overflow for the case with polydisperse material, one option is to fit model distribution functions to the data, and then use Equation (2.23) directly to determine the grade-efficiency performance. To make this work the data need to be extremely well fitted in the fine end. The alternative is to use the discrete equivalent of Equation (2.23) on the data as they are and then calculate the separation efficiency in a series of size intervals. The discrete equivalent of Equation (2.23) is:

$$\eta\left(\frac{x_i + x_{i+1}}{2}\right) = 1 - (1-\eta)\frac{(F_o(x_{i+1}) - F_o(x_i))}{(F_f(x_{i+1}) - F_f(x_i))} \tag{2.24}$$

A working principle is included in "Gas Cyclones and Swirl Tubes: Principles, Design and Operation" by Hoffmann and Stein [10].

For an ideally sharp separation within the hydrocyclone, the grade-efficiency curve would be a vertical line at the cut size, x_{50}. Due to a number of reasons this is not so, and for these reasons we obtain a smooth, s-shaped grade-efficiency curve as shown in Figure 2.9. Some reasons for this can be listed as follows:

- Depending on their entry position at the inlet, particles of the same size may be captured or lost.
- Particles greater than the cut size, x_{50}, which were already separated, may be retrained low in the cyclone geometry if the lower section is not carefully designed.
- Particles that are smaller than the cut size, x_{50}, may agglomerate into larger ones and then be separated.

2.6.4 Reduced Grade-Efficiency

As for the case with total efficiency, also the grade-efficiency curve is being influenced by the effect of flow splitting. For a hydrocyclone the effect makes the performance better than it really is. Figure 2.9 shows a typical difference between the grade-efficiency and reduced grade-efficiency curve.

The curve for the grade-efficiency does not start from the origin as it would for inertial separation. Instead it has an intercept. The value for the intercept is usually equal to the underflow-to-throughput ratio R_f and the reason for this is that the finest particles simply follows the flow and are split in the same ratio.

In the same way as the total efficiency, the grade efficiency can also be modified so that the inertial separation goes through the origin [20] by using Equation (2.25):

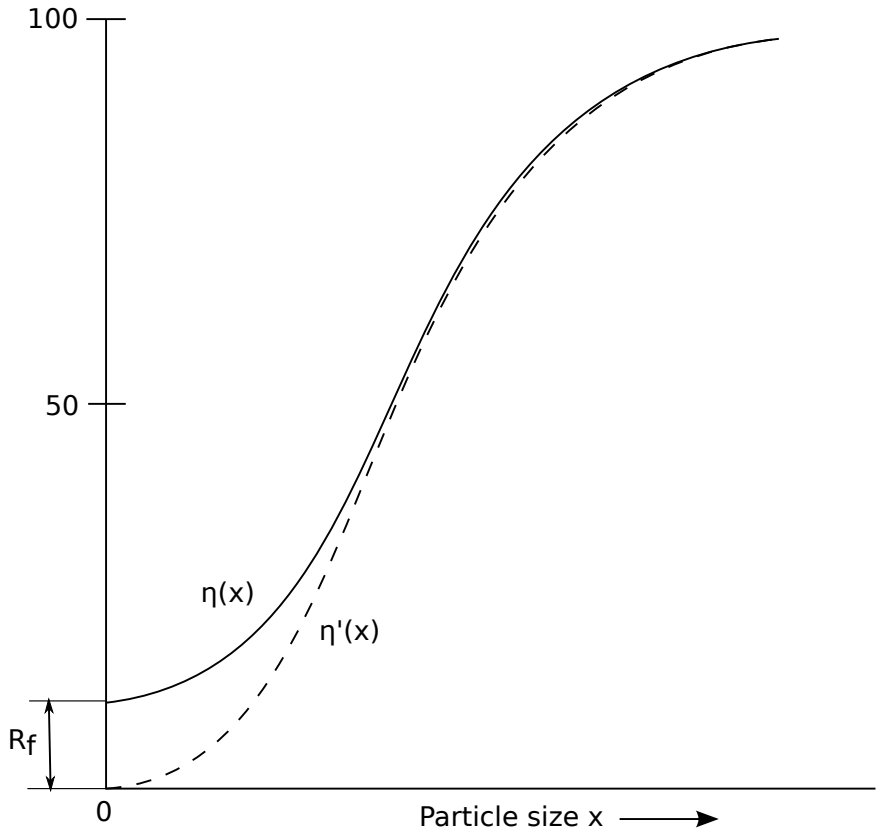

Figure 2.9: Typical grade-efficiency curve for a hydrocyclone (full line) and the reduced grade-efficiency (dashed line).

$$\eta'(x) = \frac{\eta(x) - R_f}{1 - R_f} \tag{2.25}$$

2.6.5 Cut Size

The efficiency of a hydrocyclone is often presented in terms of the equiprobable size, x_{50} [11]. At particle size equal to x_{50}, the separation efficiency is equal to 50%. This means that the particle has a 50% chance of entering the overflow or the underflow from the cyclone. According to Svarovsky [13] the best definitions of the cut size are derived from the grade-efficiency curve. Some hydrocyclone manufactures use a 95% size as the cut size [19], but the most accepted and logical definition of the cut size is the 50% size, also called the equiprobable size as mentioned earlier.

Most of the particles in the feed that are smaller than the equiprobable size will follow the overflow, while most of the coarser particles will be separated and leave the cyclone through the underflow. There is more than one definition for the cut size of a hydrocyclone, but according to Svarovsky [13] the equiprobable size x_{50} is the best-suited evaluation method for the cut size and in the same way also the best definition. Physically the cut size can be described as the particle size that gives an equal value for the inward and the outward pointing forces at the locus of zero vertical velocity (LZVV). The LZVV is further described in section 2.3.6, and the forces involved are the inward pointing drag and the outward pointing centrifugal force.

2.6.6 Sharpness of Cut

When performing a separation it is desirable to minimize the amount of misplaced material. A sharper cut means that less material is misplaced. The sharpness of the cut is related to the general slope of the grade-efficiency curve and it is defined in various ways [13]. For an ideally sharp separation the grade-efficiency curve would be a vertical line at the cut size x_{50} [10]. One way to measure the sharpness of the separation is simply to find the gradient of the grade-efficiency curve at x_{50}. Another way is to find the ratio of the diameters corresponding to two specific fractional efficiencies, for instance 0.25 and 0.75 as x_{25}/x_{75}.

2.7 Design Variations

There are many different configurations available for hydrocyclones applied in the industry. In this section the focus will be on four of the main design variables, namely the included cone angle, the inlet configuration, vortex finder design and apex design. Those who are interested in further information on design variables are referred to the article "Hydrocyclone Selection for Plant Design" [12] by Olson and Turner.

2.7.1 Cone Angle

There are two basic design configurations [13] for the conventional hydrocyclone with a single tangential inlet duct. The feature that separates the two types is the included angle of the cone. The difference in design is presented in Figure 2.10. The long cone, in the narrow-angle design, provides a thicker underflow concentration, while the design with the long cylinder gives a sharper cut [11]. The narrow-angle design has angles up to about 25 degrees, while the wide-angle design vary from 25-180 degrees [13].

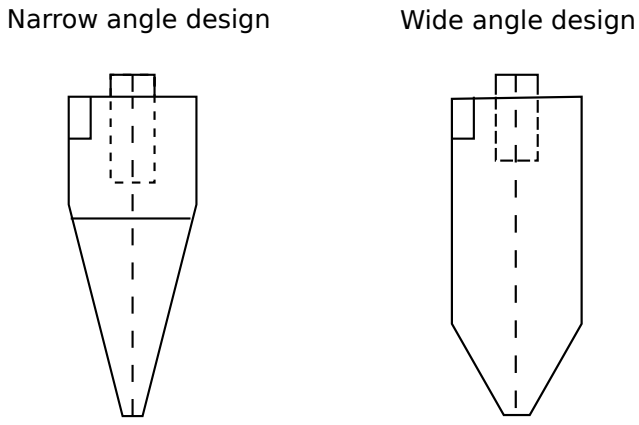

Figure 2.10: Narrow-angle and wide-angle configurations of a conventional hydrocyclone.

The length of the cylindrical section in a hydrocyclone is typically equal to the hydrocyclone diameter [12]. The longer cylindrical section provides a longer residence time and capacity at the cost of a lower tangential velocity.

2.7.2 Hydrocyclone Inlet Design

As mentioned earlier in section 2.5 the start of the separation space depends on the inlet configuration. The separation space start where the liquid carrying the solids first experience rotation and for this reason the inlet of the hydrocyclone should be carefully designed. There are several ways to vary the inlet. The shape of the inlet can be circular or rectangular [13] and the inlet opening, i.e. cross-sectional area can be varied in size. In general the capacity is higher for a larger inlet and the situation is the same for the cut-size [12]. Some different types of single inlet configurations are shown in Figure 2.11.

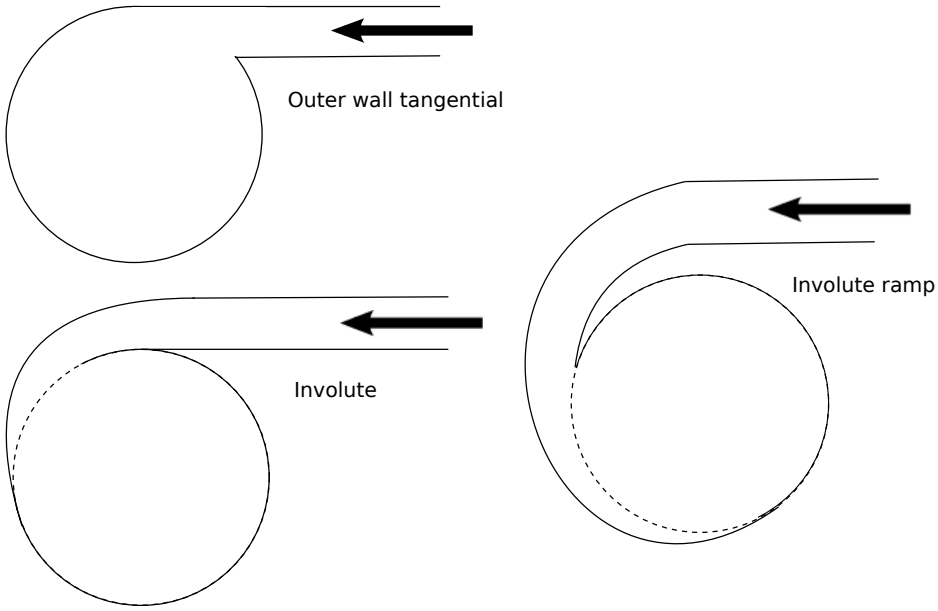

Figure 2.11: Design variations for single-inlet Hydrocyclones.

Prior to 1950, hydrocyclones featured outer wall tangential feed entry [12]. Today most of the manufactures have redesigned their inlets to include some form of involutes as they have showed to have a better performance than the previous mentioned. The new design features have also been combined with more than one inlet entry, but there is not a total agreement whether or not more than one inlet is necessary. Svarovsky [13] states that: "There is little advantage in using multiple entry which would complicate the design of the manifolding". Others have done experiments that show that two inlets give a better performance than the single inlet. Tue Nenu and Yoshida [21] have done an experimental study that shows that under the same pressure or flow rate conditions the dual inlet cyclone both provides a higher particle collection efficiency and a smaller cut size than the single inlet design. An example of an outer wall tangential dual inlet is shown in Figure 2.12.

2.7.3 Vortex Finder Design

The design of the vortex finder is important as it tells something about the hydrocyclone capacity. Larger diameter vortex finders give a higher capacity and at the same time a relatively coarser separation [12]. For a smaller diameter vortex finder the reverse effect occurs. The length of the vortex finder can also be varied. An experimental study from Martinez et al. [22] show that the depth at which the vortex finder tip is placed has a

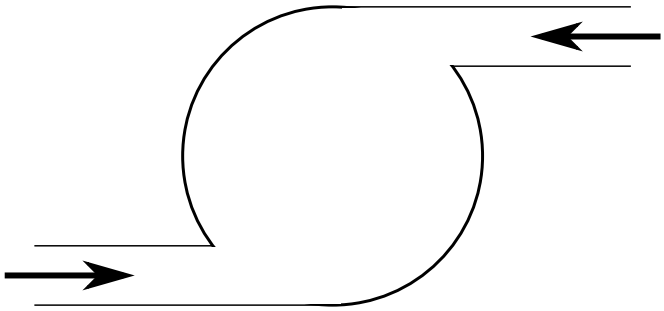

Figure 2.12: Outer wall tangential dual inlet entry.

big influence on the hydrocyclone efficiency. When the depth of the vortex finder is too small, it results in short circuit flow as described in section 2.3.4. For the case when the depth of the vortex finder is excessive, a decrease in efficiency occurs due to swirls generated at the bottom of the hydrocyclone.

2.7.4 Apex Design

The apex design and angle have a large effect on the performance [12]. Choosing the correct opening is important to maximize the underflow density and to ensure that that the apex can handle the estimated amount of solids in the underflow. When changing the apex opening, the apex angle is in most cases also varied and for that reason the apex size effects the cut-size.

The discharge pattern of an apex can provide information about what size the apex should be. A wide spray pattern indicates that there is a dilute underflow and that the apex is too large for the application. When the apex is too small, there will be a very narrow and tight discharge. One way to determine the correct opening is to sample the underflow to determine the concentration of solids. A concentration of 50% by volume is normally a good target [12].

2.8 Hydrocyclone Models

A various number of theories and models have been presented over the years. These models and theories are used in design and construction of the cyclones used today. The following sections are given to provide the reader some understanding of the design process. It is important that the reader views the following for what it is, and understands that theory and models is not a complete solution to the design and construction, and in the same way not a substitute for real test results.

2.8.1 The Simple Fundamental Theories

There are two main groups that cover the simple fundamental theories [13], namely the equilibrium orbit theory and the residence time theory. The equilibrium orbit theory and the residence time theory have in common that they both predict that the product between the Stokes number and the Euler number, $Stk_{50}Eu$, should be constant for geometrically similar hydrocyclones [23].

The equilibrium orbit theory is based on the concept of equilibrium radius. It assumes that particles of a given size will attain an equilibrium radial orbit position in the cyclone, where the particles terminal settling velocity is equal to the radial velocity of the liquid [13, 23]. According to this, the larger particles will attain a radial orbit position near the cyclone wall. There the axial fluid velocity is downward, and the particles will therefore leave the cyclone through the underflow. For the smaller particles, the radial orbit position will be located near the centre of the cyclone. In this region the axial fluid velocity is upwards, and the particles will therefore exit the cyclone through the overflow.

The residence time theory was first proposed by Rietema [13]. It assumes non-equilibrium conditions and considers whether or not a particle will reach the cyclone wall in the residence time available. Rietma [24] assumed homogeneous distribution of all particles across the inlet. The cut-size would then be the particle size which, if entering the cyclone inlet precisely in the center of the pipe will just reach the wall in residence time T. Rietma's theory does not take the radial fluid flow into account, and it does not account hindered settling at higher concentrations. It neglects any inertia effects, and assumes that any influence of turbulence is negligible.

2.8.2 Stokes-Euler Relationships

In the engineering work considering hydrocyclone performance, the general point of view is that an improved separation or purification is achieved at a correspondingly higher cost. The quality is related to the cut size of the separation, x_{50}, or the dimensionless cut size, Stk_{50}, and the cost is the pressure drop required to achieve this. The dimensionless pressure drop is as mentioned earlier in section 2.4.1, the Euler number, Eu.

Empirical relations that relate the quality of the separation to the cost have been developed. By dimensional analysis it can be shown that both the dimensionless cut size, Stk_{50} and the dimensionless pressure drop, Eu, is a function of the Reynolds number [10]:

$$Stk_{50} = f\left(Re\right) \tag{2.26}$$

$$Eu = f\left(Re\right) \tag{2.27}$$

It follows from Equation (2.26) and (2.27) that:

$$Stk_{50} = f\left(Eu\right) \tag{2.28}$$

Several correlations have been presented over the years. As quoted by Hoffmann and Stein [10], Svarovsky found that for all reasonable cyclone designs:

$$Eu_b\sqrt{Stk_{b,50}} = \sqrt{12} \tag{2.29}$$

Equation (2.29) is signified with the subscript b to explain that the mean axial velocity in the cyclone body, $\langle v_z \rangle$, evaluates the Reynolds and Euler numbers. Svarovsky also made a plot featuring the line in Equation (2.29) where some results supporting his relationship are plotted. The plot is shown in Figure 2.13:

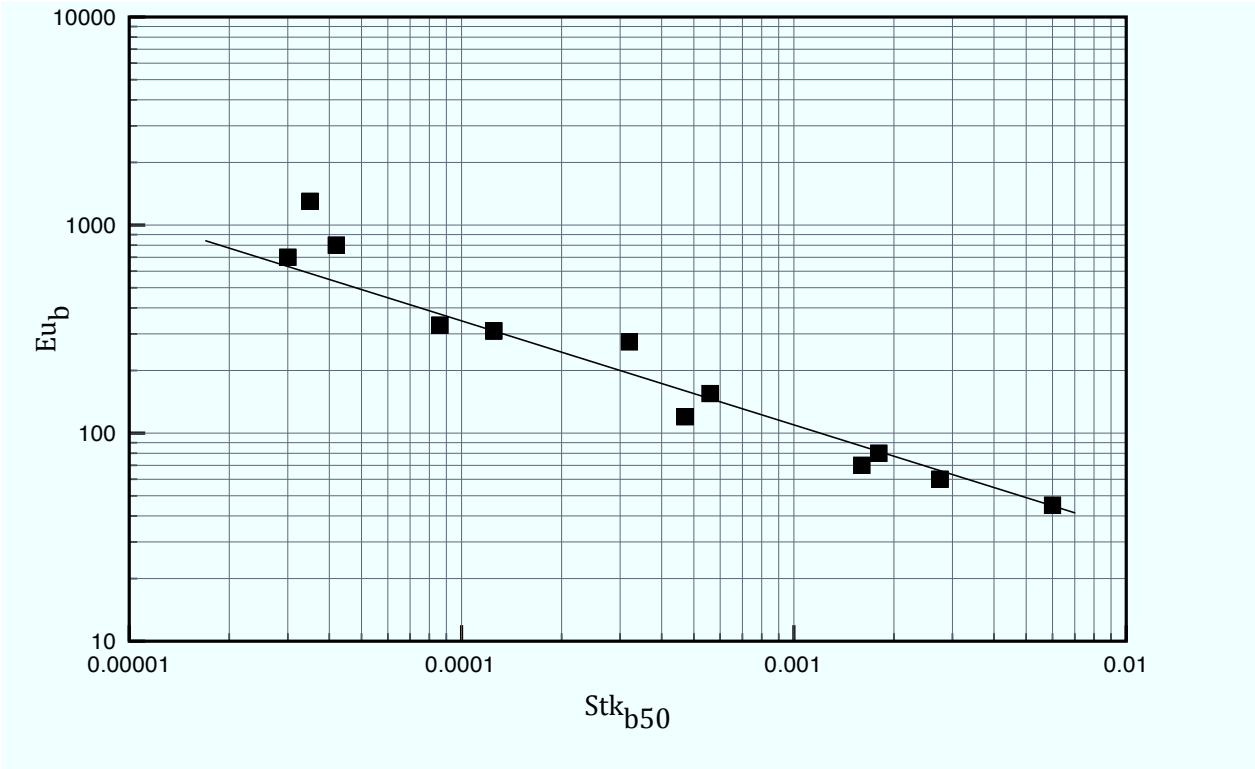

Figure 2.13: Eu_b vs. Stk_{b50} for a variety of cyclones according to Svarovsky. The line represents Equation (2.29).

Others have presented similar correlations as the one above. Karpov and Saburov have as quoted by Hoffmann and Stein [10] presented a relationship given in Equation (2.30):

$$Eu_b Stk_{b50} = 0.8 \tag{2.30}$$

which lies considerably above the line of Svarovsky.

2.8.3 Crowding Theory

The crowding theory brings up the effect of the underflow orifice capacity. Tests performed on hydrocyclones shows that there is a strong influence of underflow orifice control on the cut size [13]. This will then also influence the cyclone performance.

2.8.4 The Regression Models

The regression models are mathematical models, which almost entirely are based on regression analysis of test data [13]. The main concerns in these models are the two main performance characteristics of hydrocyclones. For a hydrocyclone that would be the capacity, or in some cases the pressure drop, and the separation efficiency in form of the cut size.

2.8.5 The Dimensionless Group Model

The dimensionless group model is based on the fundamental theory [13]. It combines the theory with dimensional analysis, giving the necessary correlations. For determination of the required constants, tests results are used rather than the ones derived from theory.

2.8.6 Analytical Flow Models

The analytical flow models are used to model the flow patterns inside the hydrocyclone. It is based on mathematical solutions of the basic flow mechanisms [13]. Possible models would be of the particle trajectories, flows in the top boundary layer and the side boundary layers. Today these models have to a large extend been abandoned in favor of the numerical simulations.

2.8.7 Numerical Simulations of the Flow

Today numerical simulations are a common way to design and predict the performance of a hydrocyclone. Many commercial software's providing computational fluid dynamics (CFD) are available for performing numerical simulations of the flow inside the cyclone.

2.9 Rheology

The rheology describes the deformation of a phase under the influence of stress. If the fluid is ideal, it deforms irreversibly under influence of stress, and the energy required to do so is transformed into heat, which cannot be recovered when the stress is removed [25]. Real liquids are both elastic and viscous to some extent. These viscoelastic fluids will deform under the influence of shear stress, but after the stress is removed the fluids will slowly recover from some of the deformation.

Since this thesis is about separation from viscous liquids, some basics about the viscosity phenomena will be given in the following section.

2.9.1 Definitions

The viscosity, μ, is a measure for the resistance of a fluid, which is being deformed by either shear stress or tensile stress. In a Newtonian fluid, the shear stress is proportional to the shear rate and the proportionality constant is called the viscosity [25].

$$\tau_v = \mu \frac{du}{dy} \tag{2.31}$$

where u is the fluid velocity and y is the distance from the wall. In SI units, τ_v is measured in Newton's per square meter and μ in kilograms per meter-second or Pascal-second. Viscosity data are generally reported in milliPascal-second or in centipoises. This is done since most fluids have viscosities much less than 1 Pascal-second. The relationship is given in Equation (2.32):

$$\mathrm{cP} = 0.01\,\mathrm{P} = 1\,\mathrm{mPa \cdot s} \tag{2.32}$$

Fluids of different type react in specific ways under influence of increasing shear rate. Normally we talk about shear rate-thinning and shear rate-thickening fluids, but there are also fluids of which the viscosity varies with time. The figure below shows the shear stress versus velocity gradient for both a Newtonian and some non-Newtonian fluids.

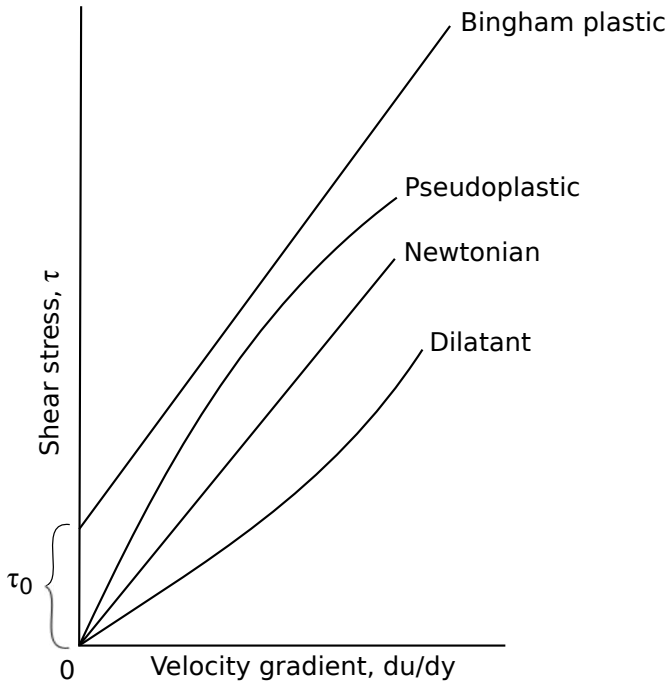

Figure 2.14: Shear stress versus velocity gradient for Newtonian and non-Newtonian fluids.

The curves that are plotted in the figure above shows shear stress versus the rate of shear applied at constant temperature and pressure. The simplest behavior is the line for a Newtonian fluid, which is simply a straight line passing through the origin. Fluids following this simple linearity are called Newtonian fluids. The other lines presented in Figure 2.14 are called non-Newtonian. Some fluids need a certain amount of shear stress applied before they start to flow. This amount of shear stress is denoted as τ_0 in Figure 2.14. After the initial amount of shear stress is applied the fluids flow linearly, or nearly so. Such fluids such as sewage sludge are called Bingham plastics. For a pseudoplastic fluid the curve passes through the origin and is concave downwards at low shear. For high shear it becomes nearly linear. Rubber latex is an example of a pseudoplastic fluid. For a dilatant fluid the curve is passing through the origin like it does for a Newtonian and pseudoplastic but the curve is concave upward at low shear. At high shear it becomes nearly linear. Some sand-filled emulsions such as quicksand behaves as a dilatant fluid.

In Figure 2.14 the lines do not consider the history of the fluids. This assumption is not correct for some of the non-Newtonian fluids, whose curves of stress versus rate depends on the time the shear has been active [25]. Thixotropic liquids break down under continuous shear, and their apparent viscosity decreases with time. The reverse manner is present for the rheopectic fluids where the shear stress increases with time. This is then also the case for the viscosity.

2.10 Liquid viscosity

The viscosity of a liquid is much higher than the viscosity of a gas at the same pressure and temperature conditions. A rule of thumb is that the viscosity increases with molecular weight and decreases significantly with increasing temperature [25]. The decrease in viscosity due to increased temperature happens because the liquid expands as the temperature goes up. This makes it easier for the molecules to slide pass each other.

Since the viscosity of a liquid depends on the temperature, varying the temperature can change the viscosity. The table below shows the temperature dependency on viscosity for water.

Table 2.1: Temperature dependency on viscosity for water.

Temperature T [°C]	Viscosity μ [cP]
0	1.792
10	1.308
20	1.003
30	0.798
50	0.547
70	0.404
80	0.355
90	0.315
100	0.282

Liquid viscosity can also be changed by adding other substances such as salt, sugar or polymers. In different research projects where the viscosity is one of the variables this is necessary to obtain the specific viscosities wanted. One common way to increase the viscosity of water is to add sucrose. Sucrose has a high solubility in water, and it is also cheap compared with many of the other available products. Another advantage by using sucrose is that the solution acts Newtonian for a wide range of concentrations [26]. This is not the case for many other products that are commonly used such as a polyvinyl alcohol and borate mixture. A mixture of PVA and Borate can give a various number of rheological behaviors depending on different variables like the molar weight of the PVA and the mixing ratio [27]. In many cases the rheological behavior is of great importance and therefore it is important to also check this property when modifying liquid viscosity.

2.11 Computational Fluid Dynamics

Computational fluid dynamics, or CFD, is a computational tool that is undergoing significant expansion in terms of courses available for students in the universities and the number of researchers active in the field. Several software packages are available and CFD codes have in the latest years started to be accepted as design tools by the industrial users.

This brief introduction to CFD is mainly focused around the features used in this thesis. CFD is a very broad field, and for those who are interested there are many textbooks available that cover both a general view and also books on specific methods such as Large-Eddy simulations, which is described briefly in this thesis.

By using computational fluid dynamics the separation performance of a hydrocyclone can be evaluated without the need of experiments. In CDF, the equations governing the flow of the fluid, namely the Navier-Stokes equations, are written in a finite difference form, and solved by a computer on a grid of points that covers the volume of the fluid inside the hydrocyclone [10].

2.11.1 Numerical Grid

There are several ways to set up a computational grid. The grid is a discrete representation of the geometric domain on which the problem is to be solved [28]. It defines the discrete locations where the variables are to be calculated and it divides the solution into a finite number of subdomains such as control volumes. The simplest grid structure available is the structured grid. Structured grids are divided into different types based on the shape of the grid lines. It may consist of H-, O-, or C-type. In a block-structured grid there is a subdivision of the solution domain. This is often used when there is need for a finer grid at specific boundaries. The coarse part of the grid contains segments that are relatively large, and their structure may be irregular. In the finer grid section a structured grid is used, and special treatment is necessary at block interfaces. The last grid type mentioned in this thesis is the unstructured grid. This type is often used for very complex geometries and the most common shapes are triangles or quadrilaterals in 2D and tetrahedra or hexahedra in 3D cases. The solvers are normally slower for an unstructured grid than for the structured ones [28].

2.11.2 Turbulent Flows

Many of the flows that we meet in engineering practice are turbulent and require a special treatment. In this thesis two of the most common methods of simulating turbulent flows are briefly described to provide the reader a general knowledge of the similarities and the differences between the models.

Direct Numerical Simulation (DNS)

In direct numerical simulation the Navier-Stokes equations are solved without averaging or approximations other than numerical discretizations. The error from the discretizations can be estimated and controlled and it is the simplest approach from the conceptual point of view [28]. In DNS all the motions contained in the flow are resolved. To ensure that all the significant parts of the turbulence have been captured, the domain on which the computation is performed must be large enough to include the largest turbulent eddy. In a valid simulation all of the kinetic energy dissipation must be captured. This happens on the smallest scales, where the viscosity is active, and because of this a very fine grid is necessary. The size of the grid can therefore not be larger than a viscously determined scale. The length scale of the smallest eddies is called the Kolmogorov scale [29], and it is denoted by η.

For many applications DNS is simply not possible because of the grid requirements. For larger geometries containing a flow of high Reynolds number the amount of grid points are higher than what even the best super computers available today are able to

handle. For the cases where direct numerical simulations are not feasible there are need for other turbulence models such as the one following.

Large-Eddy Simulation of Turbulence (LES)

The Large-Eddy simulation approach relies on the definitions of large and small scale eddies [30]. The larger eddies are in general much more energetic than the small ones and their size and strength make them more effective to transport the conserved properties than the smaller ones. In LES the large turbulent eddies are resolved numerically, while the smaller eddies are modeled.

The most important feature in LES is the low pass filter [28, 30]. This is applied to the Navier-Stokes equations to eliminate the smallest scales. The filter has a length scale associated with it and in practice the eddies of size larger than the length scale are calculated while the smaller ones are modeled. For the modeled eddies we resort to a subgrid-scale model. We will get back to that later.

In general DNS is more accurate than LES and it is preferred whenever it is feasible. LES is preferred for complex geometries with Reynolds numbers to high to use DNS.

Turbulence Modeling, Subgrid Scale Modeling

As mentioned earlier in the previous section the smallest eddies needs to be modeled by a subgrid-scale model. There are several models available, but here only the Smagorinsky subgrid model will be taken into account, as it is the one used in this thesis.

Smagorinsky J. proposed the Smagorinsky subgrid scale model in 1963 [31]. It is the earliest and most commonly used subgrid scale model available, and it is an eddy viscosity model. The model includes a model coefficient, namely the Smagorinsky coefficient and typical values form the literature varies from 0.17 for homogeneous isotropic decaying turbulence to 0.07 for channel flows. Deardorff [32] computed a fully turbulent channel flow using the Smagorinsky model. He lowered the Smagorinsky coefficient to the value of 0.1 from 0.17 to avoid the excessive damping. This value is a compromise between these extremes. Near surfaces there is need to reduce the value even further [28]. One successful way to obtain this is to use the van Driest damping, which purpose is to reduce the subgrid-scale eddy viscosity near the wall.

2.11.3 Lagrangian and Eulerian Formulation

The last subject that is covered here is how to treat particles in a continuous phase. The particles can be treated either as a second fluid, or as individual particles that can be tracked in a precalculated flow field. When the particles are considered as a second fluid it corresponds to the Eulerian approach, while it corresponds to the Lagrangian approach when the particles are considered as individual particles where the movement of a single particle is followed and its equation of motion is solved as it is tracked through the liquid flow field.

In the Lagrangian approach, the particle equation of motion is solved, mostly in a precalculated flow field [10]. Its position and velocity are calculated after successive short time intervals, and using this information the particle is tracked through the hydrocyclone.

Once the particle enters a cell with a given velocity relative to the liquid, its velocity after a short time interval Δt can be calculated from Equation (2.33) [10]:

$$U_i' = \frac{x^2\left(\rho_p - \rho_l\right) a_i}{18\mu}\left(1 - \exp\left[-\frac{18\mu\Delta t}{x^2\rho_p}\right]\right) + U_{i,0}'\exp\left[-\frac{18\mu\Delta t}{x^2\rho_p}\right] \tag{2.33}$$

Knowing the liquid velocity in the cell, the absolute particle velocity can be obtained from its velocity relative to the liquid. By integrating the absolute particle velocity over Δt, the position of the particle can be calculated, since the distance traveled equals $\int_{\Delta t} U \mathrm{d}t$. Applying this for a series of time intervals gives the path of the particle through the hydrocyclone.

Chapter 3

Literature Survey

Hydrocyclones are as mentioned used in a various number of processes. Its advantages makes it favorable for many applications, and because of this it is also interesting to test if it is possible to use this technology in new areas. This chapter contains a review on present research containing some of the same process variables as reviewed in this thesis.

3.1 The Effect of Fluid Viscosity on Hydrocyclone Performance

Separating solids from a viscous liquid is an interesting area that we are going to se more of in the coming years. Since most of the work done on hydrocyclones is limited to the separation from pure water, there is still a long way to go to fully understand the separation performance on such systems.

Emami et al. [33] have presented a study where they compare the separation of starch and protein from chickpea flour in a suspension of isopropyl alcohol and deionized water using a hydrocyclone. The purpose of the separation was to get the smaller particles, in this case the protein, to exit with the overflow, while the coarser starch should exit through the underflow.

They concluded that the separation in deionized water resulted in a higher content of starch and protein in the underflow and overflow, respectively, compared to the case with isopropyl alcohol. They relate the difference in separation to the difference in centrifugal and drag force exerted on the particles. The centrifugal force was higher for the case when the medium was deionized water, while the drag force was greater in the case where isopropyl alcohol was used.

In both cases the inlet pressures were the same. This resulted in a higher tangential velocity for the case with isopropyl alcohol than for the deionized water. The expected result from this was that the higher tangential velocity of the isopropyl alcohol would give a higher centrifugal force. This did not happen because the starch - protein separation process in isopropyl alcohol resulted in smaller particle size than in deionized water. The isopropyl alcohol had a lower starch separation efficiency and a higher protein separation efficiency than the deionized water.

Liancheng et al. [34] have done some research that is close to what is reviewed in this thesis. They have made a comparative study of the flow field of a high viscosity media in a conventional and in a rotary hydrocyclone. In their work, they have used computational fluid dynamics (CFD) to describe the difference in separation performance for the liquid medias they describe.

Their results show that the conventional hydrocyclone could effectively separate sand from water, but could not separate sand from high viscosity water/oil emulsions. For separation of sand dispersed in a high viscous water/oil emulsion the rotary hydrocyclone had a better performance than the conventional design, with a more favorable flow field distribution.

The conclusion from their work is that the viscosity of the continuous phase has a great influence for both the separation performance and the flow field distribution in the conventional hydrocyclone. This makes the rotary hydrocyclone favorable for separation of sand from high viscosity water/oil emulsions.

Guo et al. [35] have also presented a study concerning separation of sand particles from crude oil. They bring up the concern that the present sand removal by sedimentation due to gravity fails to meet the demands on removing very fine particles.

In their study they used a two-stage hydrocyclone separation setup. The results from their work shows that applying centrifugal separation is an effective way to separate sand particles of small diameters, and that it is a good alternative to the gravitational sedimentation used today.

Wang et al. [36] have also published some work regarding separation of solid particles from water/oil mixtures. To make their results easier to understand, a sketch of their setup is provided in Figure 3.1:

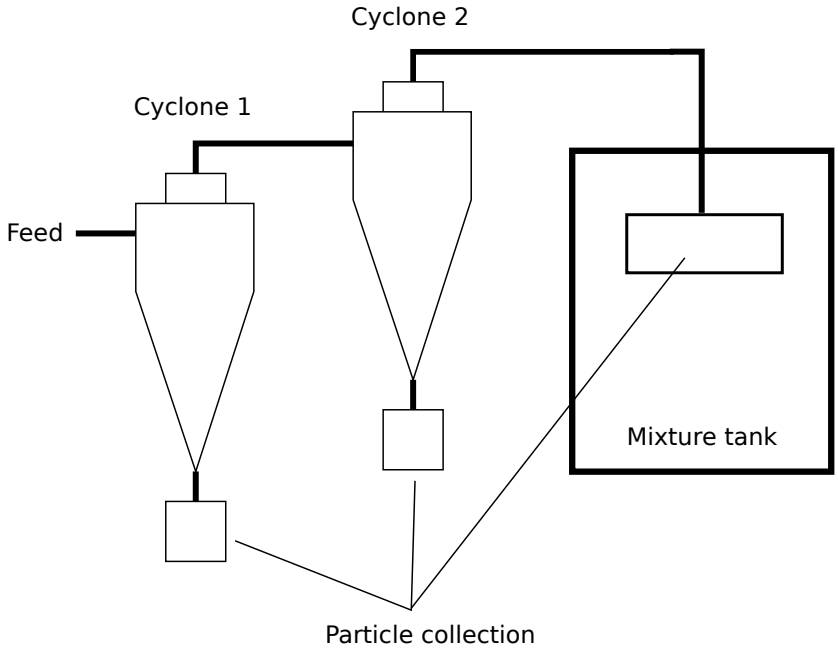

Figure 3.1: Experimental setup with two cyclones in series.

Their work consists of a number of experiments that describes the relationship between the separation efficiency and inlet velocity, oil/water ratio and the number of cyclones. The conclusions of their work can be listed as follows:

- Since the liquid/solid hydrocyclone is a compact and highly efficient separator, it is suitable to be applied on oil platforms.
- For a certain hydrocyclone, the separation efficiency mainly depends on the inlet velocity, the oil/water ratio and the size distribution of the particles.
- An increase in the inlet velocity or a decrease in oil/water ratio can improve the separation efficiency of a hydrocyclone.
- Installing a second hydrocyclone does not affect the case of low liquid viscosity significantly. If the oil/water ratio increases, more and more sand particles are separated at the second hydrocyclone.
- Small particles are more sensitive to the changes of parameters. That is the inlet velocity, oil/water ratio and the number of hydrocyclones.
- From dimensional analysis, the separation efficiency is a function of the Reynolds number and the Stokes number. When the Reynolds number is in the range between $1.0 \cdot 10^4$ and $2.5 \cdot 10^4$, there is a reasonable fit between experimental values and the calculated ones found by regression equations.

Agar and Herbst [37] have also done a study on the effect of the fluid viscosity on hydrocyclone performance. Their setup is in many ways similar to the one used is our experiments, but it differs in some areas such as capacity and measurement abilities. In their work they used sugar to modify the viscosity in the range from 1 to 35 cP corresponding to 0 to 58% by weight sucrose in water.

By using such a wide range of weight percent sucrose they also vary the apparent density of the solution. This also contributes to the separation efficiency as the difference in specific gravity is also decreased as the viscosity increase. As expected the cut size in their different experiments increase with the increase in fluid viscosity. They found that the separation size of a cyclone can be calculated by the formula:

$$d_{50} = K_1 \frac{D_c^{1.4}}{Q^{0.55}} \frac{\mu^{0.58}}{(\rho_s - \rho_l)^{0.5}} \tag{3.1}$$

where d_{50} represents the cut size, K_1 is a constant, D_c is the diameter of the cylindrical section of the hydrocyclone and ρ_s is the density of the solid particles.

Kawatra et al. [38] studied the effect of the slurry viscosity on the cut size of hydrocyclone classifiers. They used an online measurement of slurry viscosity in a test rig for a 10.2 cm diameter hydrocyclone. The viscosity was changed by varying both the solid content and the temperature of the samples. Samples from both the over and underflow streams were collected at regular intervals to obtain data for calculation of the cut size, x_{50}.

They observed that the cut size was proportional to the 0.35th power of the slurry viscosity. It was also determined that an increased slurry viscosity led to an increase in the by-pass fraction, R_f. The latter effect was explained by an increased fluid drag in the hydrocyclone as the viscosity increased.

3.2 The Effect of Fluid Viscosity on Hydrocyclone Pressure Drop

The pressure drop over a hydrocyclone is as mentioned a complex thing to describe. There is not a lot of work done on this subject, but some of the published literature is provided in this section.

Trinh et al. [39] have done a study on a 10-mm Dorr-Oliver hydrocyclone. The feed stream contained 5 wt% particles and the liquid flow rate varied from 0.9 to 4.4 l/min. Experiments were done in a viscosity range between 1 and 85 cP.

The results from their work showed that the pressure drop across the hydrocyclone was depending on the flow rate and the viscosity of the fluid. At low flow rates, the pressure drop appeared to increase with viscosity and at high flow rates the pressure drop decreased with viscosity. The overall centrifugal efficiency was found to increase with flow rate and decrease with viscosity.

Work done by Agar and Herbst [37] mentioned earlier in this chapter also show some interesting results regarding the pressure drop across the hydrocyclone. Even though it is not one of their focuses in their article, tabulated data show that an increase in viscosity leads to a decrease in pressure drop.

3.3 Water Viscosity Modification

One of the challenges in this thesis was to find an appropriate substance to increase the viscosity of water. There is a lot of information on this issue, and some of the work done is presented in this section.

Galmarini et al. [40] have done a study where they present the rheological behavior of sucrose at various temperature and concentrations. They found that sucrose has a viscosity independent of the shear rate, which means that it has a Newtonian behavior. The viscosity of the sucrose solution increased in an exponential way as the concentration increased, and an increase in temperature gave a lower viscosity, as we would expect from theory. In their study they compared the viscosity of sucrose with the viscosity of trehalose, which behaved in the same manner as sucrose. Trehalose is a naturally occurring disaccharide with the same chemical formula as sucrose but with some differences is the structure. The trehalose solution showed a higher viscosity than sucrose for all temperatures and the difference in viscosity increased with concentration and became less noticeable when raising temperature.

Several studies on the rheological behavior of aqueous solutions of sodium alginates are also available. Bogun and Mikolajczyk [41] have published a study where the rheological behavior of to different types of Sodium Alginate, one with high molecular weight and one with low molecular weight, are described. For the alginate with a high molecular weight they used a 7,0% concentration and for the lower molecular weight alginate they used a 9,2% concentration. Both solutions showed a shear thinning behavior with an increase in shear rate.

3.4 Computational Studies of Hydrocyclone Separators

Computational fluid dynamics is a common tool used for investigating the hydrodynamics in different process equipment. Some of the work done is presented in this section.

Mousavian and Najafi [42] have done a numerical study on the influence of geometry on separation efficiency in a hydrocyclone. They use three models of turbulence, the RNG $k-\varepsilon$ model, the Reynolds stress model and Large-Eddy simulation, where their presentation is mainly aimed at identifying an optimal method to study effective parameters, that affects the separation performance.

The turbulence models were compared for the predictions of air-core dimensions, mass split and axial and tangential velocities. Large-Eddy simulation was found to better predict the experimental data than the other two models. To investigate the separation performance, they used size-classification curves predicted by particle tracking in the three models. The results show that the size classifications predicted by the Reynolds stress model and Large-Eddy simulation are almost similar and that they are more precise than the RNG $k-\varepsilon$ model.

Lim et al. [43] have studied the multiphase hydrodynamics in a hydrocyclone separator using computational fluid dynamics and experiments. The flow patterns within the hydrocyclone was studied experimentally using particle image velocimetry (PIV) and computationally via Large-Eddy simulation. They collected detailed flow field information in the form of velocity vector maps of entire planes experimentally and reproduced them computationally. Good qualitative agreements between velocity vector fields, air core structure and averaged velocity distributions in their highly turbulent multiphase system were achieved. They conclude that their results provide a strong justification for the adequacy of the Large-Eddy simulation methodology for modeling the turbulent liquid flow and complex hydrodynamic interactions between the air core and surrounding liquid in a hydrocyclone separator system.

Brennan et al. [44] have worked with a model for estimation of the cut-size of a hydrocyclone. The model approach uses the Mixture model with the granular option and Large-Eddy simulation to resolve the turbulent mixing of the particles. Simulations done on a "Hsieh cyclone" in Fluent, was used to predict classification and the distribution of limestone inside the cyclone. The model predicted an efficiency curve with good accuracy even for coarse grids, while refining the grid and using a higher discretization scheme improved the predictions, by reducing the simulated short-circuiting of the larger sized limestone fractions.

Part II

Work, Results and Discussion

Chapter 4

Design and Commissioning of the Experimental Rig

The design process started in January 2009 together with the design of the PET rig, which is the other area of interest in the CLEANSAND project. At this time, the PET rig was the main priority and the experimental rig in this project was placed on hold. The purpose of the design made for this project at this stage was to be able to collect all the particles to avoid the uncertainty that you will have when you perform sampling analysis.

In this chapter, the previous design is presented together with modifications that were needed to get the system up and running. The modifications were made both during the assembly and after preliminary testing of the rig. The new design presented by the author is also presented here.

4.1 Previous design

The experimental setup was designed to perform batch runs with collection of all the captured particles. A sketch of the design is showed in Figure 4.1. It was originally planed to have online sampling of the particle size distribution of the feed and the overflow together with the collection of all the captured particles in the underflow to obtain the grade efficiency curve for different configurations.

Since the setup was planed to be operated with a certain underflow, the collection chamber below the cyclone was connected to the overflow piping to take advantage of the pressure difference for increasing the rate of the underflow. To be able to do this the collection chamber was designed with a filter that should stop the captured particles from going into the downstream tank. Both the upstream and the downstream tanks had a volume of 500 liters to ensure that the system could have a significant runtime at the required flow rates.

The piping material after the pump was planed to be out of steel (SS316L) to withstand the increase in pressure. A recirculation loop was designed to be able to adjust the flow rate in the system. The flow rate was planed to be measured by both a venturi flowmeter before the pump, and an ultrasonic flowmeter designed for suspensions after the pump. This was done to ensure that the flow rate in the system could be measured accurately. A second ultrasonic flowmeter was planed on the underflow to obtain a mass balance for the liquid media used. A control valve after the flowmeter on the underflow

should grant the possibility to adjust the underflow rate.

The downstream tank was designed with a mixer to obtain a uniform suspension of the lost particles. This was done to grant the possibility to check the size distribution manually after a batch run.

To inject particles, there was made a screw feeder, which is a device that "injects" particles by rotating a large screw connected to the piping. The feeder had an engine with an adjustable speed so that the concentration could be varied.

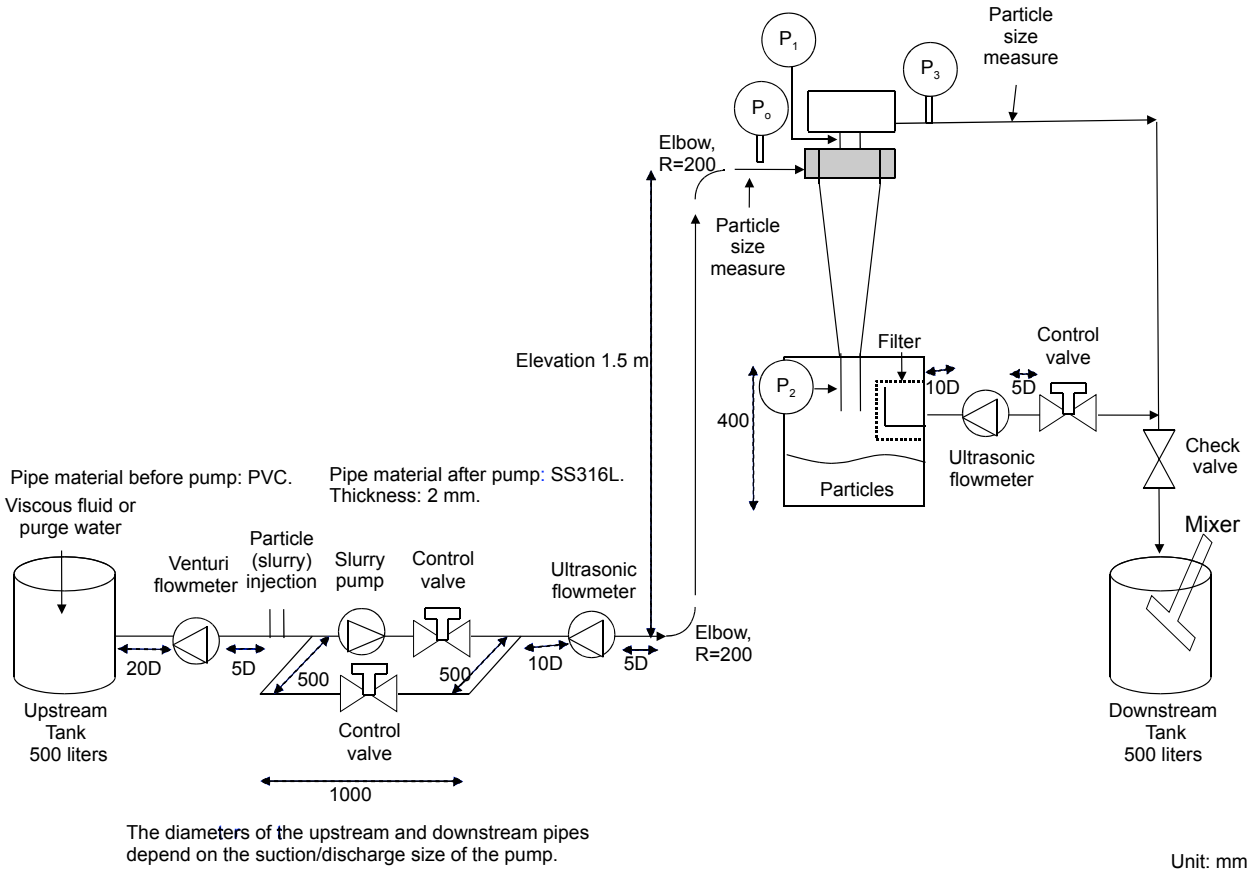

Figure 4.1: Schematic drawing of the original design for the experimental rig at the University of Bergen.

4.2 Modifications Done for Commissioning

Some of the planed design had to changed due to the budget. The online size measurements were far too expensive for the planed budget, and had to be removed. The steel piping after the pump was also replaced due to cost, as the PVC piping was evaluated to withstand the pressure. Because of this the measurement of the size distribution of the feed and the overflow streams had to be done manually. The tanks that were bought for the project were also replaced to smaller ones to ease the change of fluid and to make it possible to clean the tanks in an easy and controlled way at the rig location. The new tanks were both 200 liters.

The underflow chamber was designed with a filter to stop the captured particles. It was decided that the filter had to be able to stop particles with a size as small as 5 microns, and that the particles could be retrained from the filter so that an accurate mass balance for the system could be calculated. Several companies were contacted and none of them could deliver a filter that met our requirements. A solution with a filter paper used for filtration was tried out, but even with a metal grid to support the filter, the filter could not withstand the pressure. Because of this a new design for the collection chamber had to be made. In agreement with Aker it was decided to disconnect the underflow from the overflow piping and get a separate smaller tank for the underflow. This solution made the need for a filter redundant.

More changes were made during the assembly. It turned out that the total length of the rig was exceeding the length of the room available. The flow meters needed a certain amount of straight piping both upstream and downstream, and because of this the venturi flowmeter was removed. The venturi flowmeter was at this stage mounted on the PET rig, so that removing this saved some time in the assembly process at the same time as the length of the setup was reduced. Doing this removed the ability to control the flow rates given by the venturi and ultrasound flowmeters respectively, but the ultrasonic flowmeters was calibrated from the producer and at this stage it was the best option. More on this later in the further work chapter.

After these modifications the rig was ready for preliminary tests. The setup used at this stage is shown in Figure 4.2.

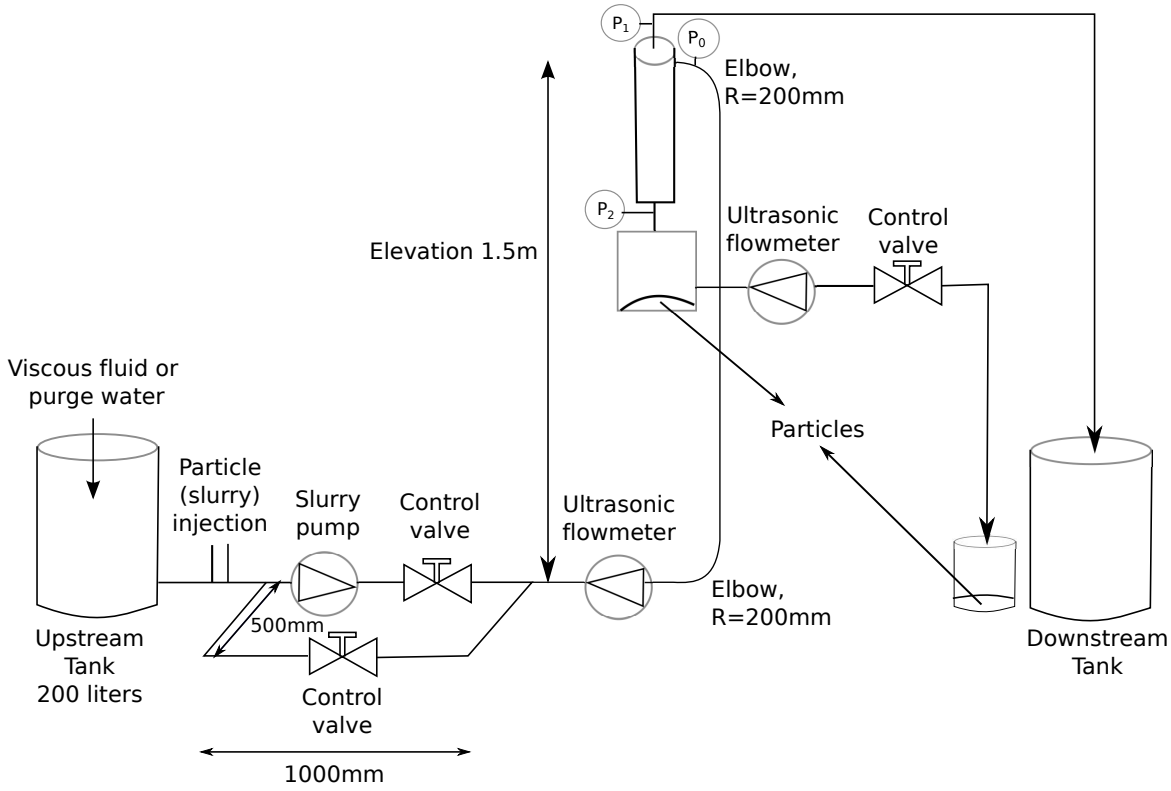

Figure 4.2: Schematic drawing of the experimental rig used during initial testing.

After fixing the leakages that was present during the first runs, the ultrasonic flowmeter on the underflow, failed to deliver a stable value. The water used during the tests was flowing into the underflow tank, but the flowmeter failed to get a good signal. After

being in contact with the manufacturer of the flowmeter different mounting angles were tried out with limited effect. A transparent hose was mounted on the pipe segment before the flowmeter on the underflow, and it turned out that pockets of air was gathered during start up of the system. The pressure in the underflow chamber was not sufficient to remove the air pockets, and some valves were mounted on the collection chamber so that the air could be removed before the system was started. This solved the problem with the flowmeter and particle injection could be tested.

The screw feeder that was designed for the setup was open to atmosphere and that caused water to rise inside the screw feeder when the system was running. The level of this effect varied with the water level in the upstream tank, and several options were tried to solve this problem. A solenoid valve was placed between the upstream tank and the screw feeder to avoid that the water rose inside the screw feeder before the pump started. This moved the problem to the pump that failed to get the water flowing because of an air section between the valve and the pump. It was tried to make a better seal between the screw feeder and the piping, but since it always will be some opening the problem was still there although it was reduced to some extent.

The performance of the feeder was then tested, and it turned out that it was very difficult to get a controlled and predictable particle loading in the system. At this stage it was decided to mix the particles in the upstream tank as that provided the possibility to use higher particle concentration and in the same time control the loading more accurately.

To avoid that particles settled in the upstream tank during the run of the system, the particle suspension was continually mixed during the run. It was assumed that the concentration and size distribution in the upstream tank was close to uniform, and the total amount of particles used for the mass balance was calculated from the differential volume in the upstream tank. The final setup which was used for the first couple of experiments is shown in Figure 4.3.

After three test runs on the setup it was very clear that the system was not very convenient to operate. It was preferable to reuse the particles so that the feed would remain the same for all the runs performed on the system. Because the underflow was going through a certain amount of piping some of the particles would remain in the piping as the system was shut down. This made need for flushing through the piping in the underflow section, which again led to an increase in volume of the suspension. After some time the increased volume had to be removed from the top layer where the particles had settled from to obtain the original concentration of particles.

Another very important concern was the low run time on the system. Since the original tanks were evaluated to big the run time with the new ones reduced the run time to about 1 minute and 30 seconds. This gave close to no opportunity to tune in the system, i.e. adjusting the flow rates, and also gave problems regarding taking the pressure and flow readings during the experiments. Knowing that it takes some time to obtain a fully developed flow inside the cyclone this problem led to the idea that a rebuild of the rig was necessary to be able to produce some good and reasonable results.

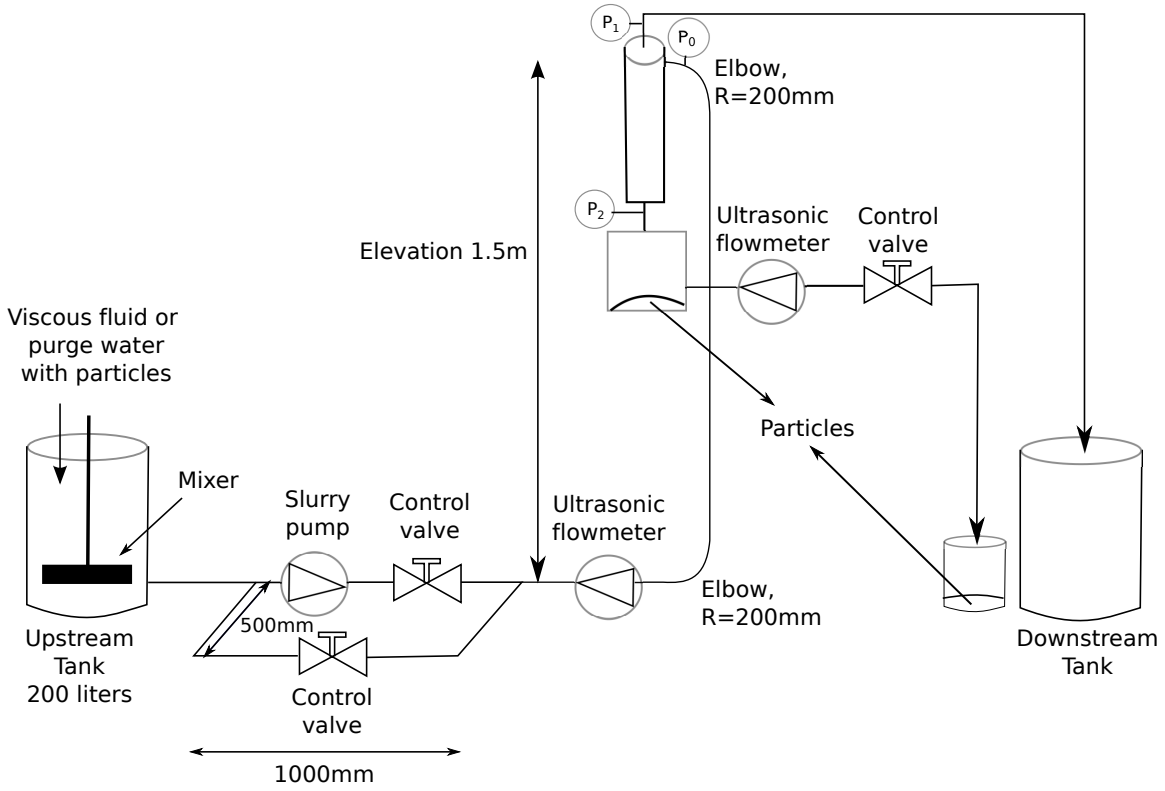

Figure 4.3: Schematic drawing of the experimental rig used during preliminary testing.

4.2.1 New Design

Since the preliminary tests performed on the system showed problems both regarding the operation and validity of the results a new design process was started. The idea for the new design was that the system should be able to run continuously and that samples from the underflow and overflow could be used to evaluate the performance. To ensure that the samples taken from the system should give a good representation of the flow, total capture of the overflow and underflow should be able to be withdrawn simultaneously to give a result representable for the separation process at the given time of separation.

The new design is shown in Figure 4.4, and a picture of the rig is given in Figure 4.5. When the samples are not collected the over and underflow is recycled back to the feed tank, and the system can run for as long as preferred before samples are collected. The new design totally removes the problem with low running time and required flushing of the piping in the underflow section. A conical collection chamber in transparent material allows visualization of the mass transport from the apex of the cyclone, and the extended area below the apex will ensure that the vortex in the cyclone dissipates as it reaching this chamber, avoiding that particles that are already separated will be caught by the upward pointing vortex and then be transported back into the cyclone body.

Compared with the setup used during the tests runs the new system was very easy to operate and it was very visible that the run time available in the previous design was far to low. With the new transparent collection chamber below the cyclone it was possible to see the particles being transported downwards from the apex of the cyclone and it was clear that it took some time to get a stable flow inside the cyclone.

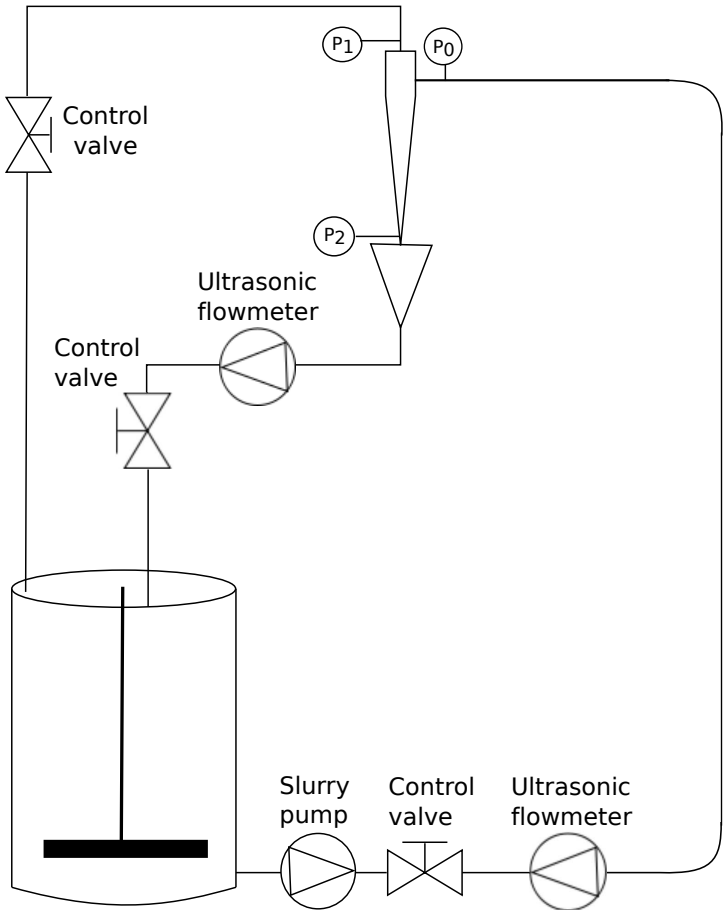

Figure 4.4: Schematic drawing of the experimental rig used for experiments.

Figure 4.5: Picture of the experimental rig used for experiments.

4.3 Equipment and Materials

The main equipment needed for this research was funded by Aker Kværner Process Systems. For flow measurement two ultrasonic flowmeters from Sierra Instruments, of model SIERRA206 were used. The piping in the rig was made from PVC material with standard fittings and bends. The feed tank had a capacity of 200 liters. Two different cyclones are used in this project. One of them is an industrial cyclone from AKPS, and the other one is a cyclone fabricated for this project.

For the experimental and numerical results the fabricated cyclone was used. The industrial cyclone was used in the preliminary testing of the rig, while the fabricated one was under construction. Experiments on the cyclone from AKPS will be performed in the continuation of this project.

The particles used in the experiments were Arizona Test Dust. The particles had a density of 2650 kg/m^3 and a size distribution in the range 0–60 μm.

4.3.1 Aker Cyclone

The Aker cyclone is made out of a ceramic material and is used to remove sand from water. Because of the ceramic material a special container had to be made to be able to connect the cyclone to the rig. The cyclone was placed inside this cylindrical container to ensure that the fluid could enter the two inlets. Since the Aker cyclone is protected by a patent, Aker require that some details about the geometry remains confidential. Figure 4.6 shows how the Aker cyclone is assembled, and together with Table 4.1 some size characteristics for the cyclone is given.

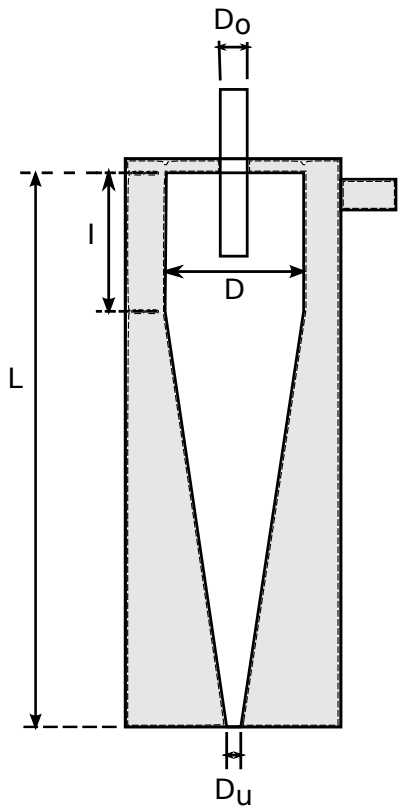

Figure 4.6: Schematic drawing showing how the AKPS cyclone was assembled.

Table 4.1: Some size characteristics for the AKPS cyclone.

Symbols	L	I	D	D_u	D_o
Cyclone [mm]	419	57	40	6.4	12.5

4.3.2 University Cyclone

The other cyclone used for this project is identical to the one used in the hospital rig for later comparison. The design is done with respect to Starimand High Efficiency design [45], with some modifications to serve or purpose which is de-sanding. The hydrocyclone body is made out of glass fiber, and the inlet and overflow pipes are made out of PVC material. The specific design with all the size characteristics is given in Figure 4.7 and Table 4.2:

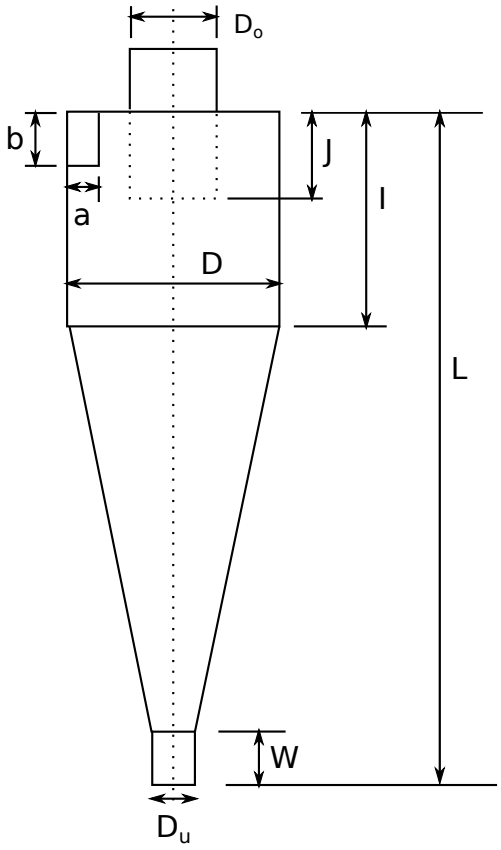

Figure 4.7: Schematic drawing of the University Cyclone.

Table 4.2: Size characteristics for the University Cyclone.

Symbols	L	I	D	D_u	W	D_o	J	a	b
Cyclone [mm]	440	65	40	10	25	20	35	9	29

4.4 Operation

Prior to each run the suspension was mixed for 30 minutes to ensure that all the particles in the feed tank was uniformly dispersed. Then the pump was started and the system was running for 5 minutes to ensure that a proper separation was present. For the case with pure water as the liquid component, the system was tuned by adjusting the total flow rate and the flow rate of the underflow by checking the values on the flowmeters. For the other cases the flow meter for the total flow rate failed to get a good signal and another method had to be used.

Since the flowmeter used to measure the total flow rate failed to get a signal for the cases with increased viscosity, the volumetric flow was measured by sampling out a volume from the overflow and the underflow over a given time interval. The volumes were added together to obtain the total flow rate, and the underflow rate was compared with the one from the flowmeter. Several measurements were made to ensure that the flow rate were as accurate as possible.

To obtain the total efficiency the density of the underflow was measured. Three measurements were made and the average density was used to calculate the amount of solids in the underflow. The total efficiency was then calculated by taking the amounts of solids captured and divide it by the amount of solids that went through the cyclone during the time the underflow was sampled.

To increase the viscosity of the suspension, sucrose was added between the runs, and to ensure that the solid concentration was the same for each run, water was evaporated from the feed to keep the volume constant. All solids involved in measurements were resuspended in the feed so that the size distribution of the feed would remain the same for all the experiments.

The volumes samples from the overflow taken to measure the flow rate were also used for size analysis of the lost particles. Three samples for size analysis where taken and the third sample was used when the first two did not agree. The samples from the viscous cases were heated to about 70 °C to decrease the viscosity so that the particles would settle faster. After the particles had settled to the bottom the liquid was removed by a syringe and returned to the feed tank. The solids where then resuspended in deionized water and the process was repeated once more to bring the viscosity as close to 1 cP as that decreased the time necessary for the sedimentation analysis significantly.

Chapter 5

Development of Experimental Methods

In this chapter the method used for obtaining the particle size distributions is given together with a brief introduction to the method used to measure the viscosity of the liquid used in the experiments.

5.1 Particle Size Analysis

To obtain the grade-efficiency curve for the different cases studied in this thesis, the size distribution of the particles in the feed and overflow were measured. Both the Andreasen pipette method [46] and the sedimentation method were tested in the preliminary stages of this project, and for experiments the sedimentation method was chosen due to its simple configuration and reliability.

5.1.1 Sedimentation Method

The sedimentation method is performed by recording the sedimentation of solids dispersed in a liquid medium [17]. From the recorded data the size distribution of the particles can be derived from the measured temporal change of the particle concentration. This process is governed by the free-fall velocity of the particles, and from this a free-fall or Stokes diameter can be determined.

There are two methods available to introduce the solids to the liquid. One of them is to apply a thin layer of the solids at the top of the liquid. The other method which is the one used in this thesis is to uniformly disperse the solids in the liquid by shaking, stirring or ultrasonic agitation before measurement.

Two approaches may be used to determine the size distribution of the particles. The first one is the incremental method where the change in solid density or concentration is measured at a given location in the sedimentation column. The second one which is the one applied in this thesis is called the cumulative method. In this approach we measure the rate at which the solids accumulate at the bottom of the sedimentation column.

The cumulative distribution is obtained by normalizing the measured concentration value by the initial concentration c_0 [17].

$$F_m(t) = 1 - \frac{c(t)}{c_0} \tag{5.1}$$

In order to determine the cumulative distribution as a function of particle size, we have to correlate the sedimentation velocity with the particle size. We need an expression for $D(t)$, the particle that has just passed our measuring point at time equal to t, to find $F_m(D)$. Taking only the drag, buoyancy and gravity forces in consideration, the particles equation of motion in the Stokes drag regime is given by Equation (5.2):

$$\frac{dv}{dt} = -\frac{18\mu}{\rho_p D^2} v + \left(1 - \frac{\rho_l}{\rho_p}\right) g \tag{5.2}$$

When the particles reach their terminal velocity, there is no further acceleration and by solving Equation (5.2) for D we obtain:

$$D(t) = \sqrt{\frac{18\mu v_t}{(\rho_p - \rho_l)g}} = \sqrt{\frac{18\mu(H/t)}{(\rho_p - \rho_l)g}} \tag{5.3}$$

Equation (5.3) measures the Stokes diameter, D_{st}, as long as Stokes law is valid, i.e., $Re_p < 1$, which is generally applicable for sedimentation analysis since small particles normally are considered.

One of the most common ways to perform the cumulative method is to use a sedimentation balance where the solids collect on a balance pan and the weight of the particles accumulated is continuously measured. According to the principle of this method the weight of the solids will increase at constant rates. During the initial period, the weight increase at a constant rate until all the particles of the large diameter have accumulated on the balance pan.

When using a sedimentation balance a tray is suspended from an analytical scale at a distance equal to H under the surface of the suspension. The mass accumulated on the tray at a given time t is given by Equation (5.4) [17]:

$$m(t) = m_0 \left[1 - F_m(D)\right] + m_0 \int_0^D \frac{h}{H} f_m(\lambda) d\lambda \tag{5.4}$$

where D is the particle diameter that has just settled out in time t, m_0 is the total mass in the sample and h is the distance that particles of size λ have settled during time t. The first term represents the mass of the particles which have a diameter larger than D, and the second term the mass accumulated on the balance for all particles with a diameter smaller than D. Figure 5.1 shows an example of the temporal change in accumulated mass for three distinct particle sizes which is homogeneously dispersed in the sedimentation column.

The distance h in Equation (5.4) is related to the terminal settling velocity, $v_t(\lambda)$ by the relation given in Equation (5.5):

$$h = v_t(\lambda) t \tag{5.5}$$

Substituting the last quality into Equation (5.4) and dividing by m_0 results in:

$$\frac{m(t)}{m_0} = 1 - F_m(D) + \frac{t}{H} \int_0^D v_t(\lambda) f_m(\lambda) d\lambda \tag{5.6}$$

Continuing by taking derivative with respect to time gives:

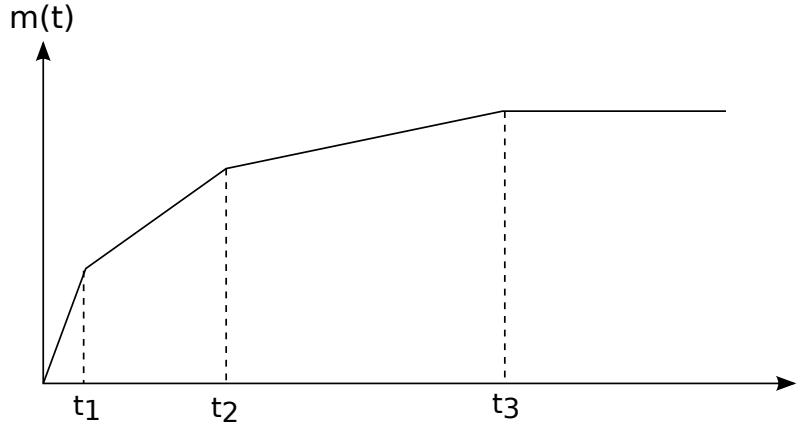

Figure 5.1: Temporal change of accumulated mass on balance pan.

$$\frac{d}{dt}(\frac{m}{m_0}) = -\frac{d}{dt}F_m(D) + \frac{1}{H}\int_0^D v_t(\lambda)f_m(\lambda)d\lambda + \frac{t}{H}v_t(D)f_m(D)\frac{dD}{dt} \tag{5.7}$$

We know that at time t, $H{=}v_t(D)t$ and that by definition $F_m(D){=}f_m(D)dD$. This reduce Equation (5.7) above to:

$$\frac{d}{dt}(\frac{m}{m_0}) = \frac{1}{H}\int_0^D v_t(\lambda)f_m(\lambda)d\lambda \tag{5.8}$$

Using Equation (5.6) to relate the integral to the mass accumulation and cumulative mass fraction we obtain Oden's equation:

$$F_m(D) = t\frac{d}{dt}(\frac{m}{m_0}) - \frac{m(t)}{m_0} + 1 \tag{5.9}$$

Oden's equation can be used to determine the cumulative mass fraction from the slope of the mass accumulation curve, and together with the Equation for the Stokes diameter, (5.3), a size distribution for a given dispersion of particles can be determined.

The main equipment used for the sedimentation was an analytical scale from Sartorius with a density determination kit. To validate the method a test was performed on a particle standard with a size distribution in the same range as the expected size distribution for the particles used in the experiments. To make sure that the particles were properly dispersed an ultra sonic bath was used for 2 minutes, and then the suspension was transferred to a container with a magnetic stirrer to maintain the suspension before it was transferred to the setup. A picture of the setup can be vied in Figure 5.2:

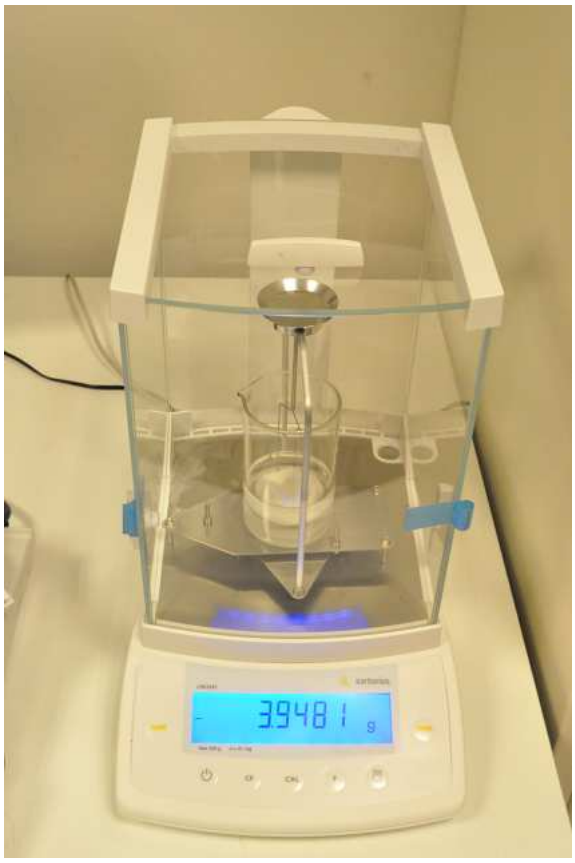

Figure 5.2: Setup used for measuring particle size distributions.

5.2 Viscosity Measurements

Many different configurations are available for measuring the viscosity of a fluid. Here we will cover only the method used in this thesis, namely the Cone and Plate rheometer.

5.2.1 Cone and Plate Rheometer

In the cone and plate rheometer, the liquid is placed on a horizontal plate with a shallow cone placed on top of it, where the angle between the cone and the plate is typically in the order of 1 degree. One of the plates is rotated while the other one is kept in a locked position, and the force applied to obtain a specific rotational speed is measured. A schematic diagram of the cone and plate rheometer is given in Figure 5.3.

If the gap angle θ is small ($\leq 5^o$), the shear rate $\dot{\gamma}$ is approximately constant everywhere within the sample [47], and it is given by Equation (5.10):

$$\dot{\gamma} = \frac{\Omega}{\theta} \tag{5.10}$$

The shear stress τ on the cone is given by Equation (5.11):

$$\tau = \frac{3\,C}{2\pi r^2} \tag{5.11}$$

where r is the radius of the cone and C is a constant depending on the characteristics of the instrument [47].

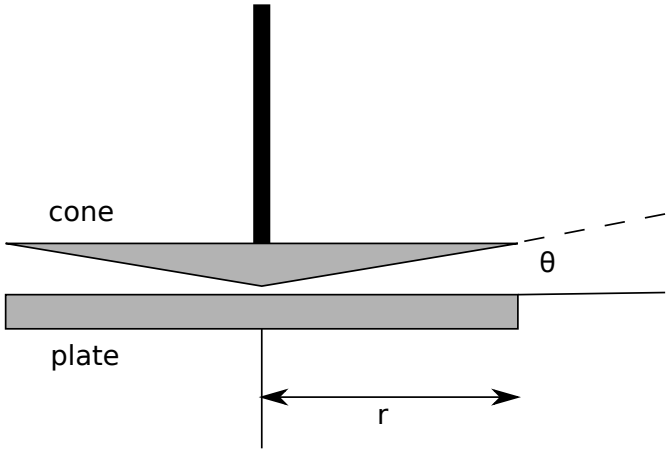

Figure 5.3: Schematic diagram of the cone and plate rheometer.

The instrument used in this thesis was a MCR 300 rheometer from Anton Paar. A picture of the setup is given in Figure 5.4:

Figure 5.4: Anton Paar MCR 300 plate and cone rheometer.

Chapter 6

Computational Setup

Computational fluid dynamics has in the last decades developed to be a very popular, profound and efficient tool for investigating the properties of different flow related systems. The advantage with CFD is that a large number of variables can easily be changed and tested. As a supplement to the experimental work done in this thesis, it was decided to simulate the separation process within the cyclone. This was done using Large Eddy Simulation (LES) together with a Lagrangian Multiphase Model for comparison with the experimental results.

6.1 Software and Simulation Preferences

The commercial CFD software STAR CCM+ v.5.06.010 from CD-Adapco was used for the simulations. This software provides a large number of available models for solving the flow, and it provides a built in CAD-model to build everything from simple to more complex geometries. It also provides a various number of meshing abilities to ensure that the calculations can be made very accurate at important areas such as boundaries.

6.1.1 Computational Domain

The fluid region inside the hydrocyclone body was meshed with a computational grid containing trimmed cells. Near the walls a prism layer was made to get an even finer cell size near the walls. The meshed geometry is shown in Figure 6.1.

To find a suitable cell size for the computational mesh a grid dependency test was made. The coarsest grid that gave negligible differences in the velocity profiles when refining the grid was used for the simulations.

The particles were injected from 234 different positions on the inlet. A total of 936 mono sized particles were injected and the particles that left through the overflow was counted by using a derived part based on its tracks and then using a build in element count report that is available in the program. Several simulations with different mono sized particles were done to obtain a grade-efficiency for the separation. The method used to count the particles was found through trial and error. After first being in contact with the support office for the simulation program there should not be a direct method of doing it. Their suggestion was to find the incident mass flux of the solid particles, but that required a continuous flow of particles. The method found when working with this

Figure 6.1: Meshed geometry used for simulations.

problem was first validated by a number of tests by the author of this thesis, and later also by the support department from CD-Adapco.

6.1.2 Solver Parameters

The computational domain was solved by using an implicit unsteady solver with a time step of 0.001 second with 2nd-order discretization. A segregated flow solver was used to control the solution update for the segregated flow model. The segregated flow model solves the flow equations, which includes one for each of the velocity components and one for the pressure in a segregated, or uncoupled, manner.

6.1.3 Particle Tracking

As mentioned a Lagrangian Multiphase model was used to be able to track the particles in the cyclone body. The particles were treated as solid material particles with constant density. A track file was generated to be able to count the particles that exited through the overflow. Two way coupling was not used, while the drag force was calculated using the Schiller-Naumann drag coefficient.

Chapter 7

Performance Data Obtained, Experimentally and Numerically

To find the best suitable viscosity modifier, several options were tested. The goal was to find a component that increased the viscosity of the water without changing other properties significantly. It was also preferable that it should be easy to mix and that it behaved as a Newtonian fluid.

After some initial testing several of the components that were tried out showed difficulties regarding one or more of the requirements mentioned above. The secure solution would be to use sucrose, as it is a well-known viscosity modifier that behaves as a Newtonian fluid. Since there is need for a significant amount of sucrose to increase the viscosity, the density of the solution is also affected.

To avoid the increase in density some further tests were performed on a sodium salt of alginic acid. The Alginate Scogin LV alginate were tested at low concentrations to see if it was possible to obtain a viscosity up to about 20 mPas without experiencing shear thinning behavior. To evaluate the rheological properties of the alginate the viscosity of three different concentrations were measured over a wide range of shear rates. The measured concentrations were 0.2, 0.4 and 0.6 wt% respectively. Figure 7.1 shows the results from the measurements.

As it can be seen from Figure 7.1 the lowest concentration of alginate, i.e. 0.2 wt%, behaves very much like a Newtonian fluid. For the 0.4 wt% concentration it is visible that shear thinning occurs at a shear rate above 100, while the 0.6 wt% concentration starts to behave shear thinning already at a shear rate around 40.

The resulting shear thinning behavior for the alginate made it unsuitable for our research, and therefore sucrose was found to be the best option for our case.

7.1 Experimental Results

The capacity of the experimental rig was evaluated for the two cyclones available for experiments. The AKPS cyclone had a maximum throughput of 4.4 m^3/h, while the University cyclone had a maximum throughput of 6.8 m^3/h, with water as the liquid component.

Since our purpose was to increase the viscosity, and keep the flow rate constant for the experiments, the target flow rate chosen for the experiments was 5.3 m^3/h. However, it turned out that the capacity of the University cyclone did not decrease with the increase

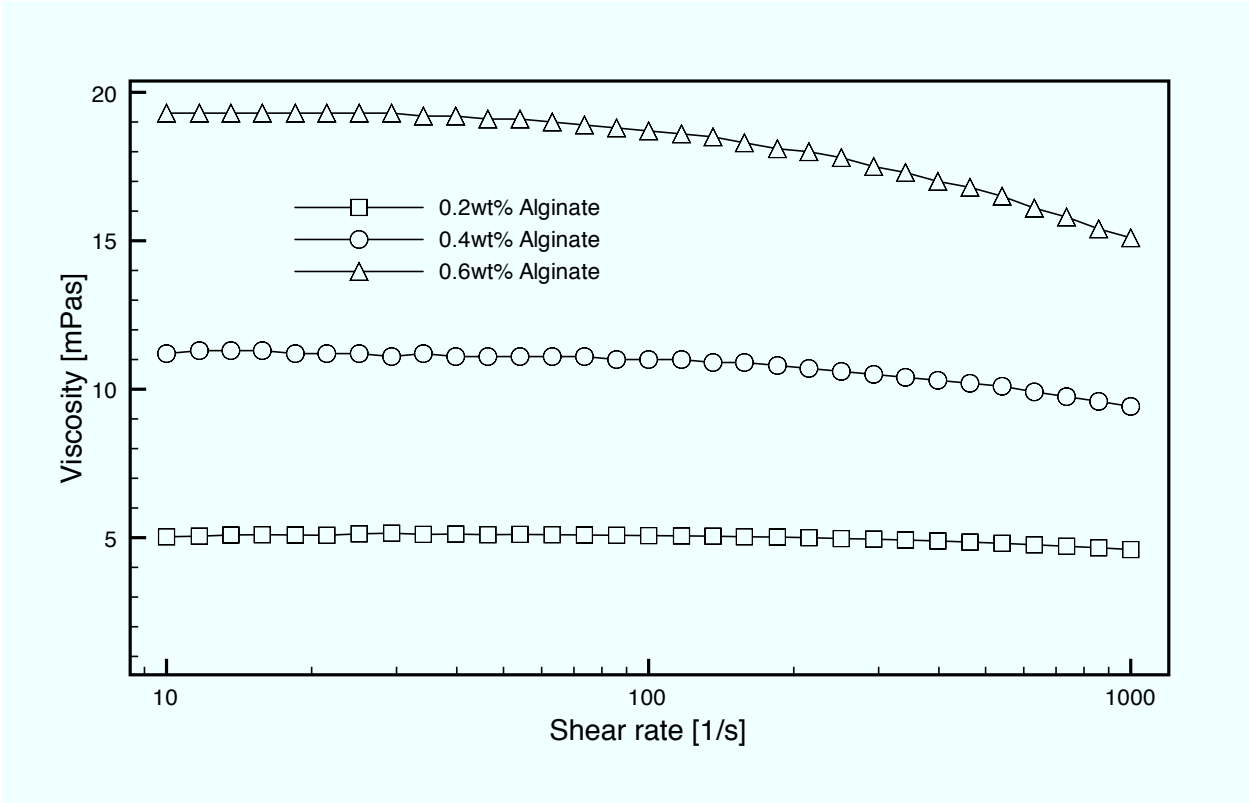

Figure 7.1: Rheological behavior of Scogin LV alginate at low concentrations.

in viscosity as the pressure drop across the cyclone decreased as described later.

To make the water more viscous, sucrose was added to the feed while water was evaporated so that the viscosity increased and the volume was kept close to constant. The viscosity of the continuous phase, i.e. the sucrose solution was measured over a wide range of shear rates and they all behaved Newtonian as we expected. Figure 7.2 shows the measured values of the viscosities.

The parameters used during the different tests are shown in Table 7.1. Test 3 differs significantly from the other tests, as there were some problems with some of the instruments at the time this test was performed. From test number three, new pressure measurements were installed in the rig as the original ones was influenced by the sucrose solution. More on this subject is given under further discussion.

Table 7.1: Parameters used for experiments 1-5.

Test No.	Inlet P [Barg]	Overflow P [Barg]	Underflow P [Barg]	ρ_l [kg/m^3]	Feed loading [vol%]	μ [cP]	Q_{TOT} [m^3/h]	Q_{UF} [m^3/h]
1	2.18	0.79	0.47	1000	1.106	1	5.35	0.30
2	1.95	0.625	0.55	1081	1.106	2.0	5.34	0.35
3	2.2	0.68	0.50	1135	1.106	3.8	6.12	0.42
4	1.5	0.4	0.45	1208	1.08	11.3	5.41	0.401
5	1.25	0.25	0.45	1224	1.08	15.1	5.42	0.36

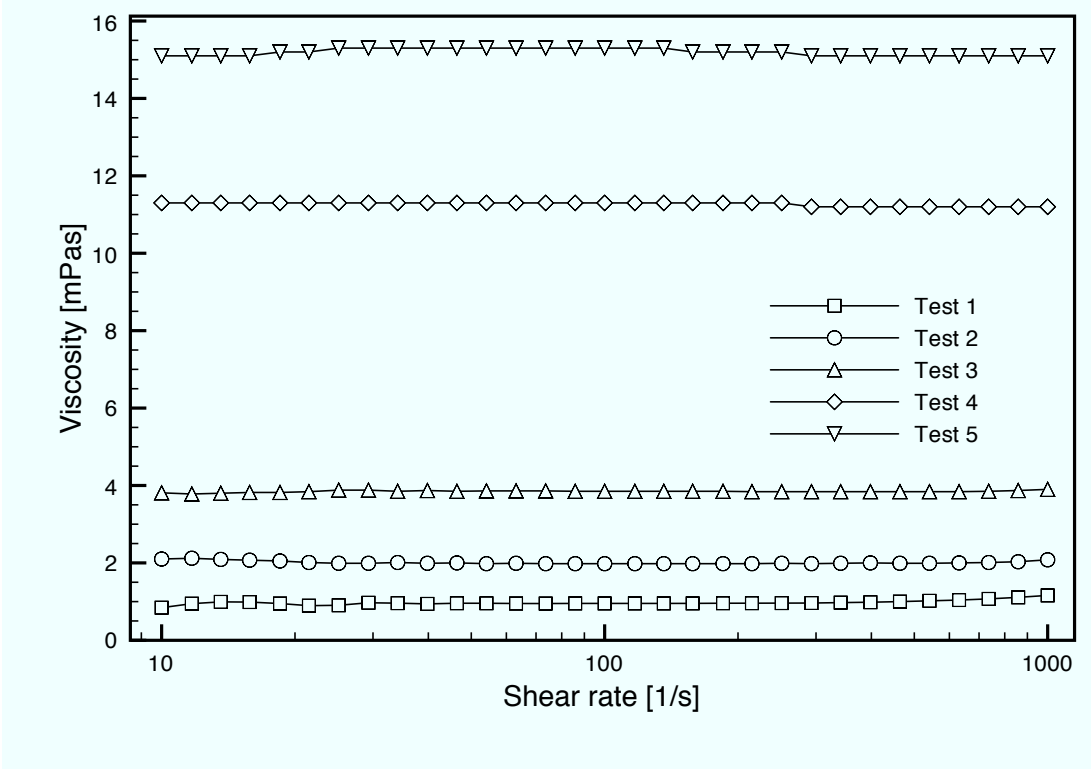

Figure 7.2: Measured viscosities for experiment 1-5.

The total and the reduced efficiencies were found by using Equation (2.15) and Equation (2.16) respectively. Table 7.2 gives the calculated values for the efficiencies.

Table 7.2: Efficiencies for experiments 1-5.

Test No.	η	η'	x_{50} [μm]
1	0.75	0.735	11.1
2	0.65	0.625	15.25
3	0.44	0.399	20.87
4	0.24	0.179	31.63
5	0.18	0.122	34.32

As expected the total efficiencies went down as the viscosity of the sucrose solution increased. The results for the reduced efficiencies show that the tests with the lowest total efficiencies are most influenced regarding the reduction in efficiency. As we can see, the total efficiencies for test number four and five are rather low which results in a overflow size distribution that lies closer to the feed size distributions compared to the other tests. This gives rise to the idea that a coarser feed stream could have been used for evaluating the efficiency for the two highest viscosities in this thesis. Because of the low total efficiencies in the last experiments it was evaluated that a further increase in viscosity would result in a total efficiency so low, that the results would be hard to validate.

The total efficiency was as mentioned earlier calculated from the density of the underflow suspension. If the particle content is very low it will result in an increased uncertainty for the measurements. Our goal was to use the same particles for all the

experiments, and that was succeeded by limiting the highest viscosity used in the experiments.

To obtain a value for the cut size, the size distribution of the feed and the overflow were used together with the total efficiencies to produce a grade-efficiency curve for the experiments. Figure 7.3 gives the size distributions of the feed and the overflow for Test 1. The grade-efficiency curves for the tests are presented in Figure 7.4.

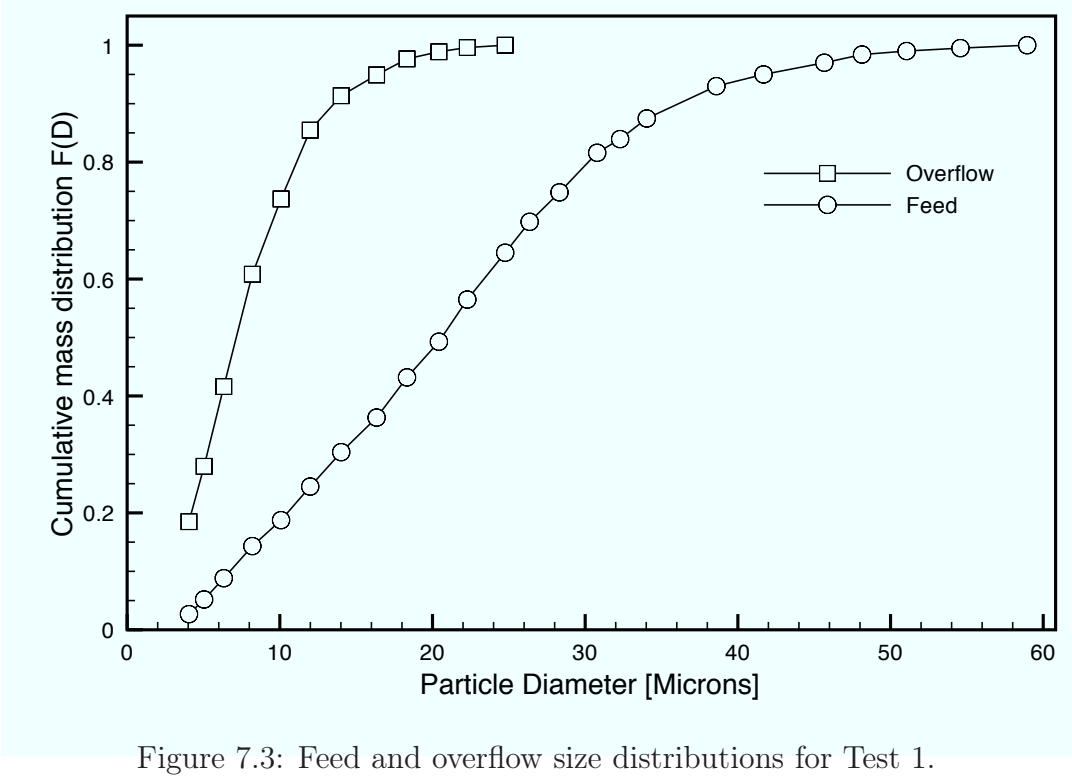

Figure 7.3: Feed and overflow size distributions for Test 1.

The cut size for the experiments were found by interpolation to the 50 % mark on the grade-efficiency curves presented in Figure 7.4. The cut size, x_{50}, for the experiments are shown in Table 7.2. The grade-efficiency curves presented is based on the total efficiency, and therefore ends on a value above 0. The reduced grade-efficiency curves can be obtained by Equation (2.25) and the reduced grade-efficiency curve for three of the experiments are shown in Figure 7.5.

From the grade-efficiency curves it can be seen that the cut size, x_{50}, increases when the viscosity of the liquid carrier fluid is increased. The curves given are obtained without any smoothing of the size distributions. This is a very good achievement as smoothing often is required to avoid scattered grade-efficiency curves.

The key to obtain this is to have good size distributions, and this was emphasized in our work. Many configurations were tested and evaluated before satisfactory results were obtained.

From Figure 7.5 it can be seen that the reduced grade-efficiency curves goes to zero as they are expected to do from theory. However, obtaining this is not easy and it is again a very good indication on the high quality of our results.

Material balances were made for all the tests. To validate the size distributions measured, the feed size distribution was calculated from the two product streams. The solid line in Figure 7.6 represents the measured size distribution of the feed. The calculated ones are denoted by symbols.

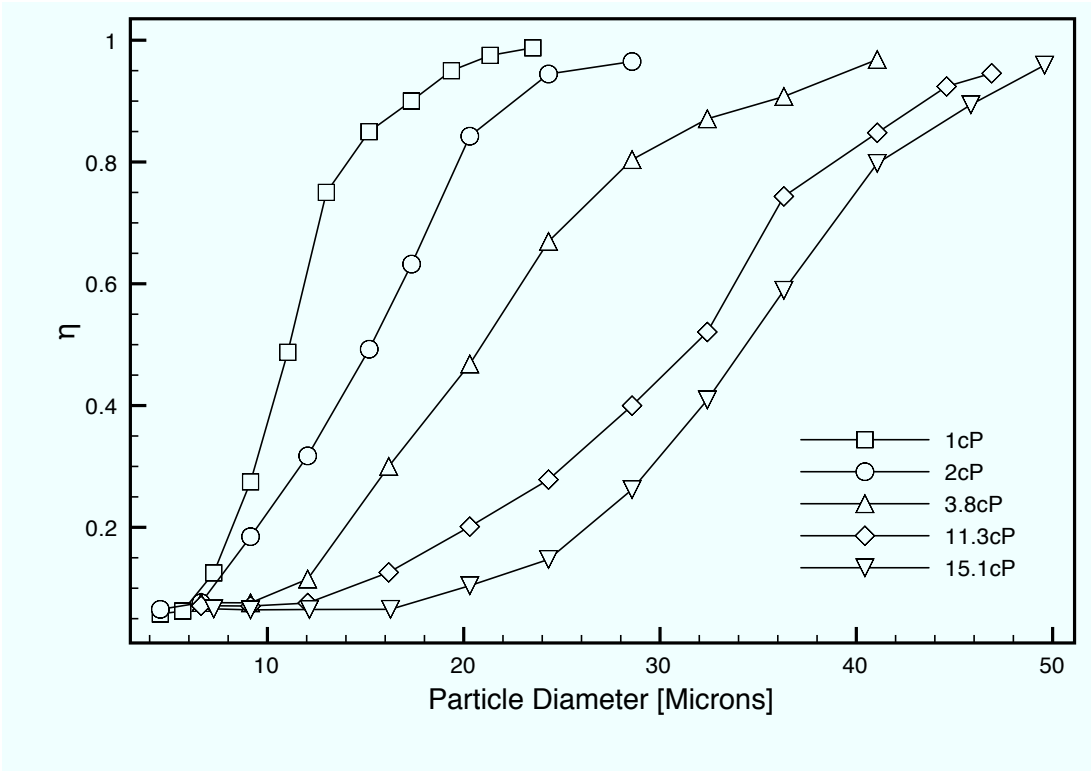

Figure 7.4: Grade-efficiency curves for Tests 1-5.

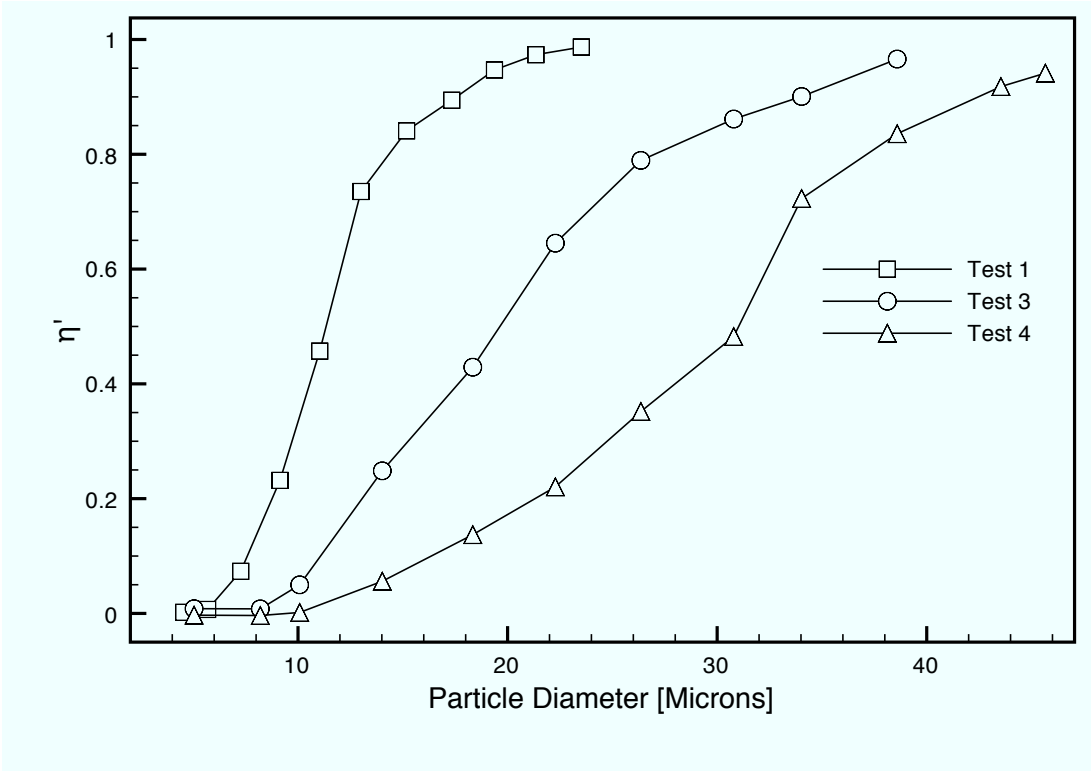

Figure 7.5: Reduced grade-efficiency curves for test 1, 3 and 4.

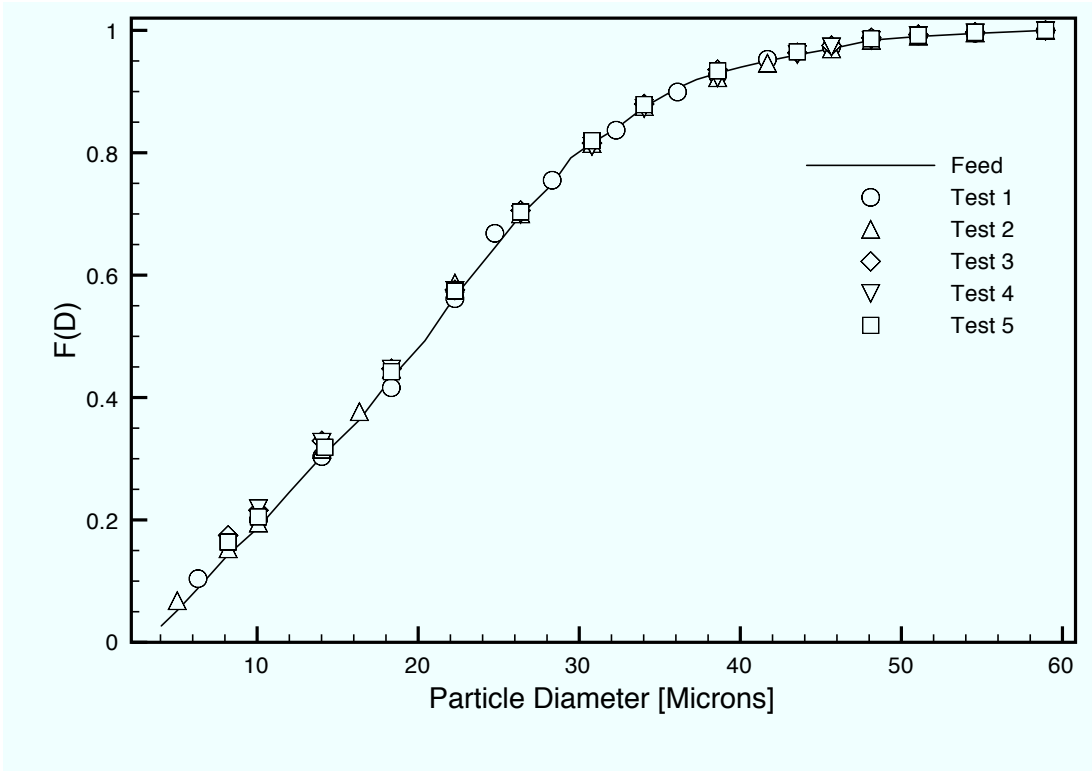

Figure 7.6: Calculated and measured feed particle size distribution.

From Figure 7.6 it can be seen that the calculated feed size distribution fits very well with the measured one. This indicates that the mass balances for the experiments are very good and that the method used for calculation of the efficiencies was suitable.

7.1.1 Reproducibility

In order to check the validity of the results, some of the experiments were done once more to check the reproducibility. Test two and five was done again at the exact same suspension, while test four was redone by removing some of the sucrose solution after the particles had settled from the top layer. The amount of liquid removed was replaced by pure water and the viscosity was measured to be 11.2 cP, which is very close to the original viscosity of that test.

The parameters used in the new tests are shown in Table 7.3:

Table 7.3: Parameters used for the new tests.

Test No.	Inlet P [Barg]	Overflow P [Barg]	Underflow P [Barg]	ρ_l [kg/m^3]	Feed loading [vol%]	μ [cP]	Q_{TOT} [m^3/h]	Q_{UF} [m^3/h]
2	1.96	0.622	0.55	1081	1.106	2.0	5.345	0.349
4	1.5	0.4	0.45	1208	1.08	11.2	5.42	0.40
5	1.25	0.25	0.45	1224	1.08	15.1	5.43	0.36

The new grade-efficiency curves are plotted with the first ones for comparison. The result is shown in Figure 7.7:

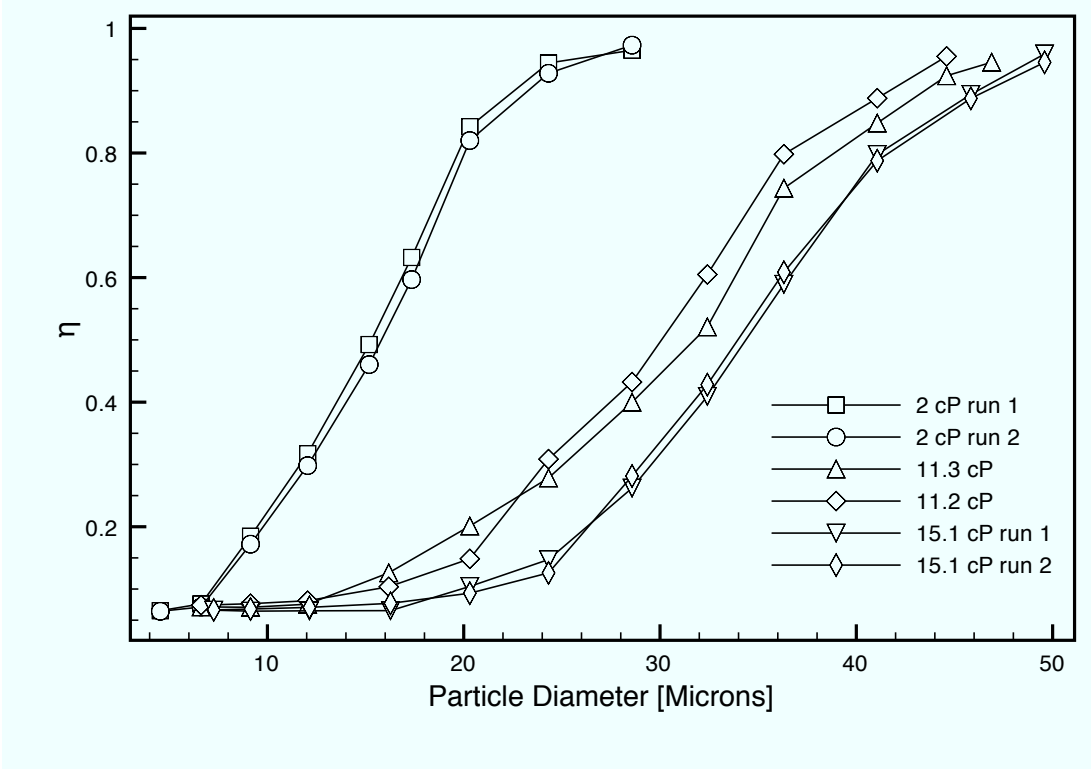

Figure 7.7: Comparison of grade-efficiency curves for reproducibility tests.

From Figure 7.7 it can be seen that the remade experiments fits well with the original ones. The remade experiments for test two and five fits very well, while the second experiment on test four differs some from the original test. Even though the two runs on test four are a little different, the results from this are still very good. At low total efficiencies very small errors in the size distributions make a significant effect when calculating the grade-efficiency curves.

7.1.2 Pressure Drop

The pressure drop over the cyclone was investigated for the experiments. The pressure drops for the experiments are given in Table 7.4:

Table 7.4: Pressure drop from experiments.

Test No.	1	2	3	4	5
Δp [bar]	1.39	1.325	1.52	1.1	1

With exception of test number three, which had a higher flow rate than the other tests, the pressure drop decreased with increased viscosity. When the flow rate increased the pressure drop increased as expected. These are very valuable results for the industry as the expected result when related to normal pipe flow is the opposite of what experienced in this thesis. Comparing these results with the literature survey, it can be seen that the same effect that occurs with increased wall roughness is experienced. The roughness does not contribute directly to an increased wall loss, but it contributes to a reduction in swirl intensity. When the viscosity is increased, the same effect occurs. Reduction of the

swirl intensity leads to a lower amount of static pressure being transformed into dynamic pressure in the cyclone body. The dissipation of mechanical energy in the vortex finder is therefore less for the experiments with high viscosity, and that is the main reason that a lower pressure drop is experienced for those cases.

Increasing the flow rate leads to a more intense vortex in the cyclone body. This leads to more static pressure being transformed into dynamic pressure, and therefore also more dissipation of mechanical energy in the vortex finder. As losses in the vortex finder is the main contribution to cyclone pressure drop, this leads to an increased pressure drop as expected.

7.1.3 Stokes-Euler Relationship

The results from the experiments were plotted in a Stokes-Euler diagram. The result is shown in Figure 7.8:

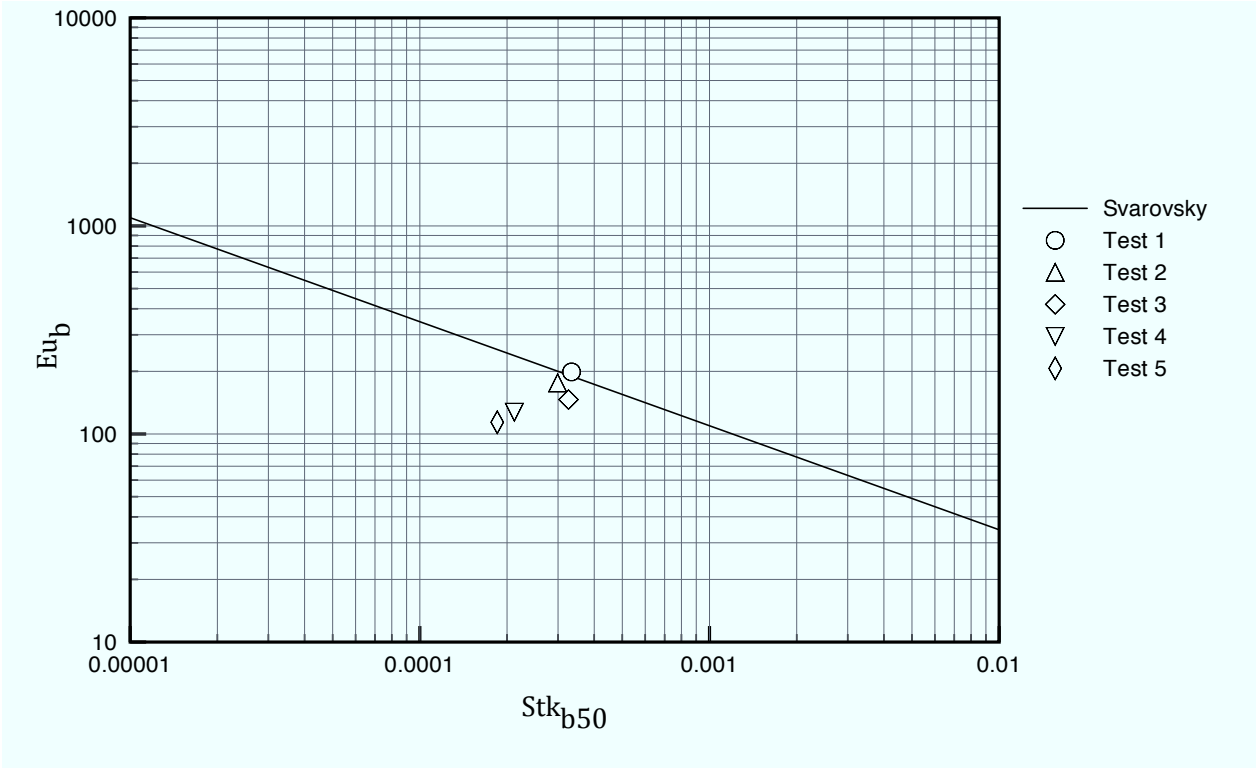

Figure 7.8: Calculated Stokes-Euler relationship for experiments. The solid line represents Equation (2.29).

The first three experiments ends up near the line that represents Equation (2.29), while the two experiments with the highest viscosities ends up below the line. Since the plot represents a quality versus cost evaluation, a point below the line would represent a good separation achievement relative to the cost. The experimental data represented in the plot from Svarovsky in Figure 2.13 does not say anything about at what conditions the results were obtained. More experimental data containing separation from a viscous fluid should therefore be gathered before saying anything about the validity of the model on viscous fluids.

7.1.4 The Effect of Fluid Viscosity on Flow Split

With the geometry from AKPS, the system provided a decent amount of underflow when pure water was used. When the university cyclone, which has a relatively large vortex finder, compared to the Aker cyclone was used all of the flow went to the overflow. As the viscosity increased, the natural split of the product streams varied and different valves had to be adjusted to get the same conditions for the experiments. More of the flow went to the underflow as the viscosity increased. The latter is the same as we saw in the literature survey in the work done by Kawatra et al. [48]. It can therefore be said that it is very likely that increasing the viscosity of the fluid leads to an increase in the natural by-pass fraction, R_f.

7.2 Numerical Results

A grid dependency test was done to find a suitable grid size for the simulations. The velocity profile inside the cyclone body was used when deciding whether the tested grid size was too big. The cell counts and the related cell size used in this test is given in Table 7.5.

Table 7.5: Cell diameter and cell count for grid dependency tests.

Cell diameter [mm]	2	1.8	1.6	1.4	1.2	1	0.8
Cell count	92000	125000	166500	227000	327000	537000	1011000

With a cell size above 1.6 mm there was a significant difference in the velocity profiles in the lower section of the cyclone. Below 1.4 mm the differences where close to negligible and a cell count of 227000 cells was used in the simulations.

7.2.1 Numerical results for test 1 (1 cP)

The grade-efficiency curves from the simulation and the experiment are shown in Figure 7.9.

The simulated grade-efficiency curve ends up rather high compared to the experimental one. The flow split in the simulation was checked, and the underflow rate was found to be around 5% as it should be from the simulation setup. From the simulation the pressure drop was found to be 0.80 bar, which is significantly less than the pressure drop from the experiment that was equal to 1.39 bar. The pressure distribution from the CFD simulation is given in Figure 7.10.

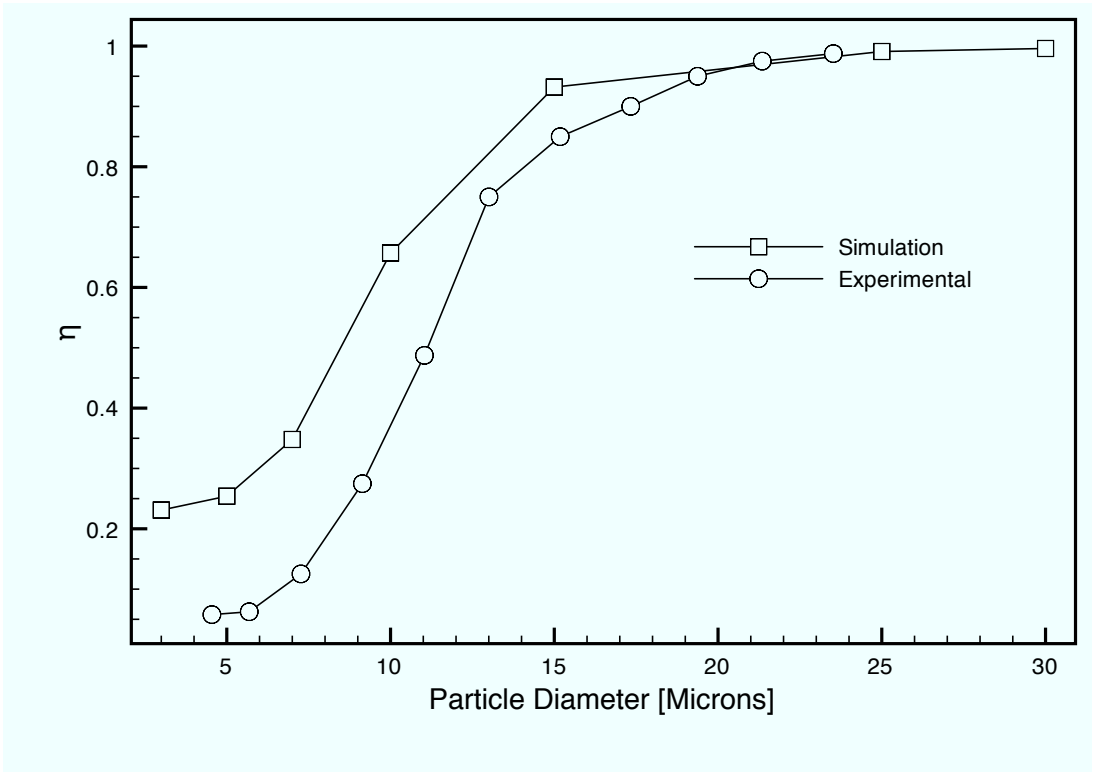

Figure 7.9: Experimental and simulated grade-efficiency curves for Test 1.

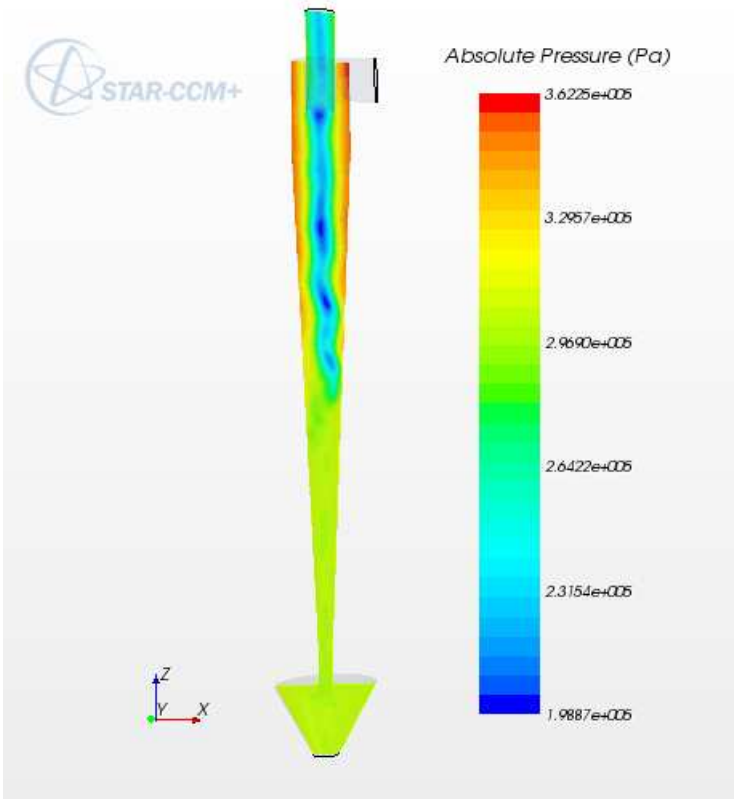

Figure 7.10: Pressure distribution from CFD simulation, 1 cP.

7.2.2 Numerical results for test 2 (2 cP)

The grade-efficiency curves from the simulation and the experiment are shown in Figure 7.11.

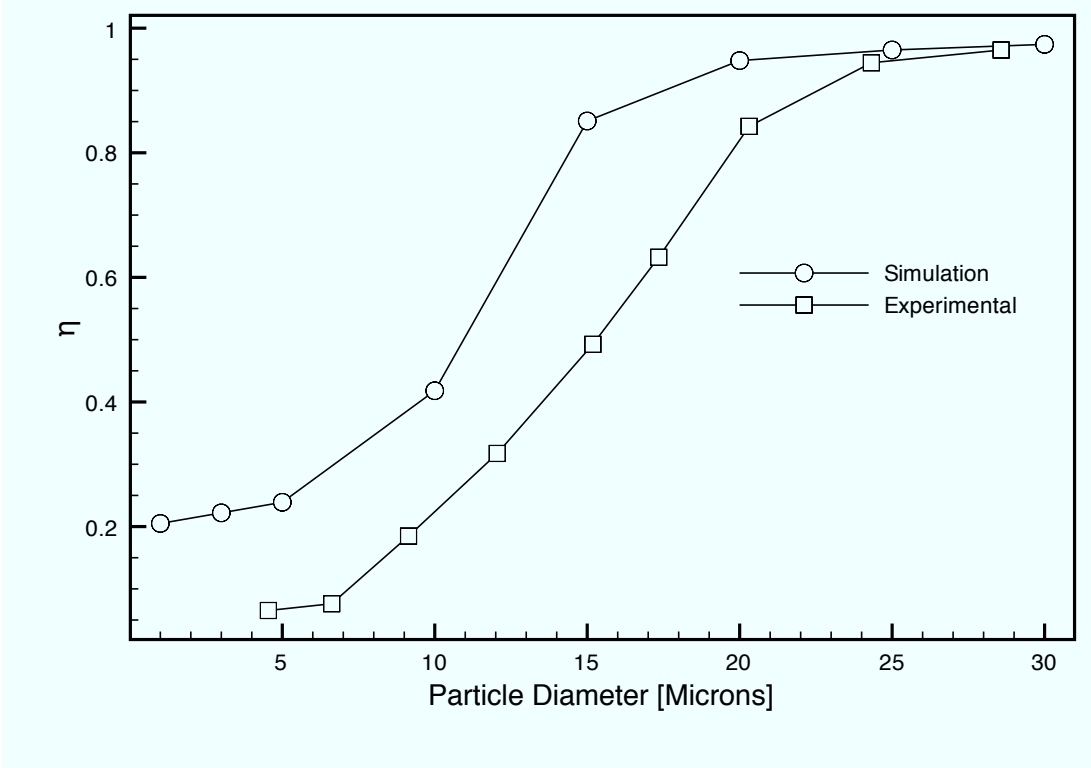

Figure 7.11: Experimental and simulated grade-efficiency curves for Test 2.

In the same manner as test 1, the simulated grade-efficiency curve ends up rather high compared to the experimental one. The flow split was checked also for this case with the same result as for test 1. From the simulation the pressure drop was found to be 0.89 bar, which is both higher than the simulated pressure drop for test 1, and significantly less than the pressure drop from the experiment that was equal to 1.325 bar. The pressure distribution from from the CFD simulation is given in Figure 7.12.

7.2.3 Numerical results for test 4 (11.3 cP)

The grade-efficiency curves from the simulation and the experiment are shown in Figure 7.13.

The grade-efficiency curve from the simulation predicts lower separation efficiency for the largest particles, and significantly higher separation efficiency for the smallest particles. Since also this case ended on a rather high separation efficiency, the flow split was checked for this case as well. The underflow rate was found to be around 5% of the total flow rate. From the simulation, the pressure drop was found to be 0.87 bar, which is less than the pressure drop from the experiment that was equal to 1.1 bar. The pressure distribution from the CFD simulation is given in Figure 7.14.

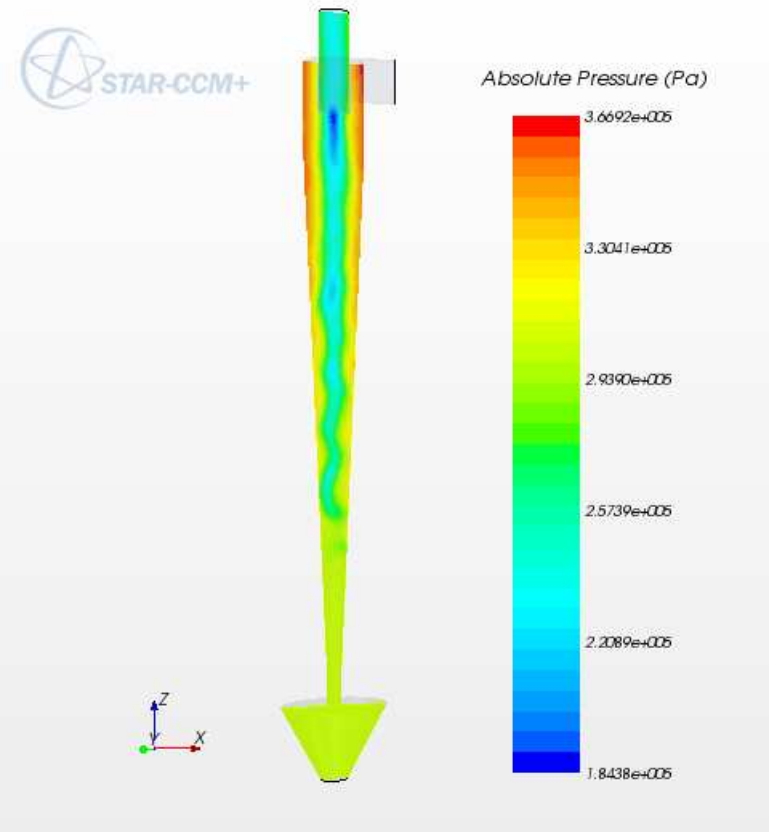

Figure 7.12: Pressure distribution from CFD simulation, 2 cP.

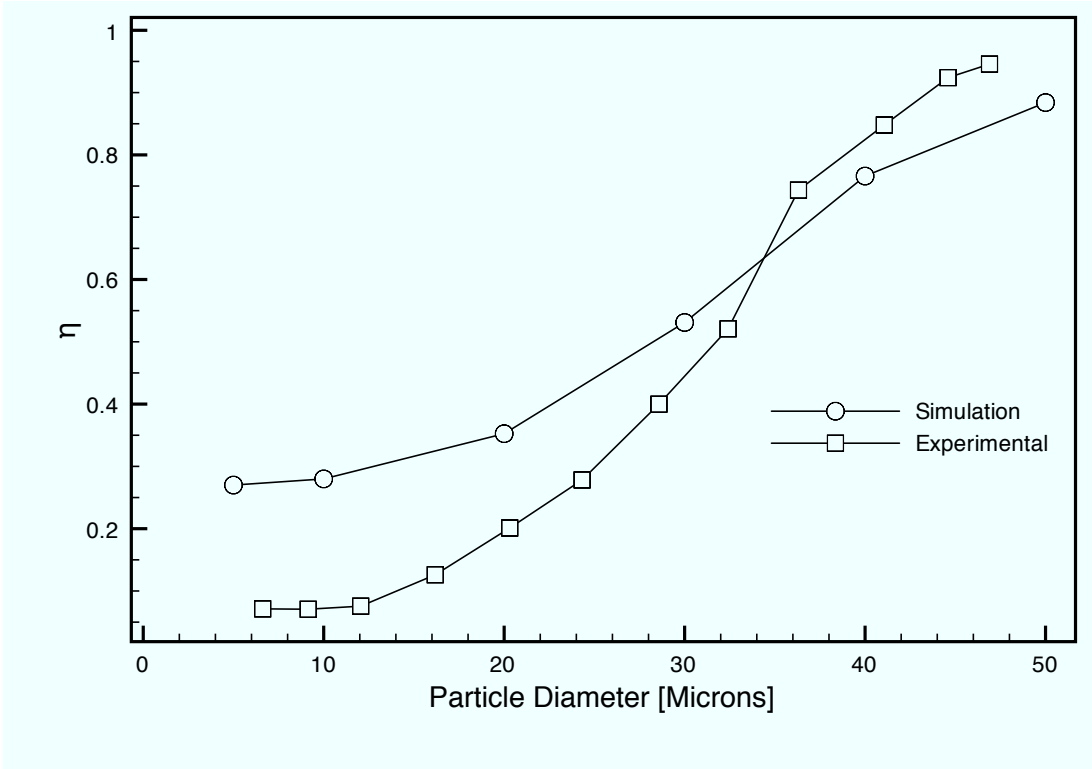

Figure 7.13: Experimental and simulated grade-efficiency curves for Test 4.

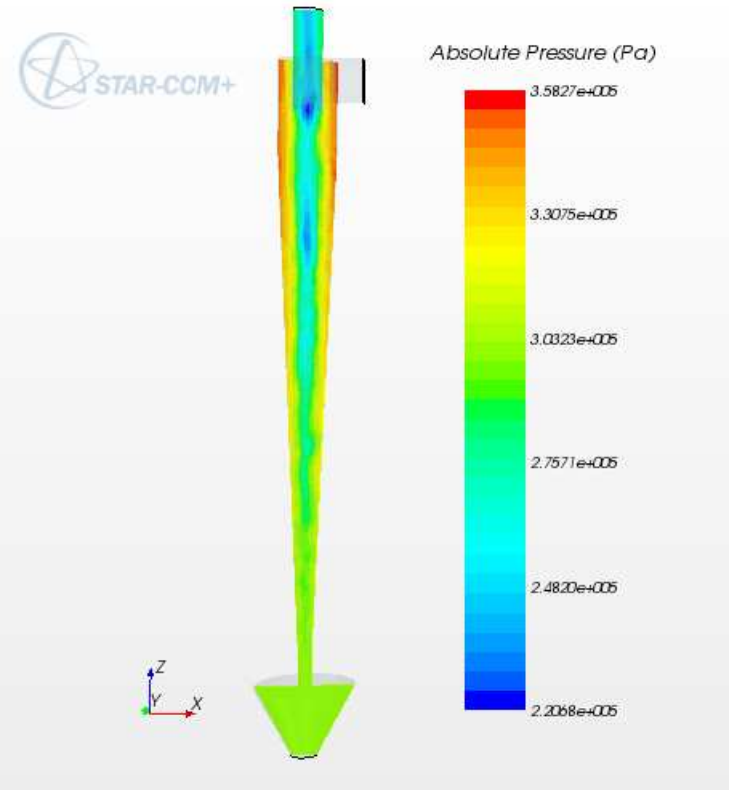

Figure 7.14: Pressure distribution from CFD simulation, 11.3 cP.

7.2.4 Numerical Results Summary

Also the numerical simulations show that the cut size, x_{50}, increases when the viscosity of the liquid carrier fluid is increased. However, it is very easy to see from the grade-efficiency curves that the calculations of the efficiencies are clearly wrong when looking at the efficiencies for the smallest particles. This phenomena was further investigated and it appeared that some of the points on the injection grid always ended up with a capture of the particles.

In Lagrangian particle tracking, the particles are treated as a point without a size relative to the flow field. That means that some of the points that was located at the wall where not affected by the turbulent regions inside the cyclone body. A refinement of the injection grid giving a lower fraction of points located at the walls had a big influence on the separation efficiency on the smallest particle sizes.

The pressure drop calculations from the numerical simulation differ significantly from the experimental results. This was to some extent expected, as the pressure tappings in the experiments were located at different positions than in the CFD model. In the experimental setup the pressure reading for the inlet was done at a circular pipe close to the tangential inlet, while in the simulation it was located in the tangential inlet section. The pressure at the inlet and overflow in the simulation were found from a cell value at the wall.

From Figure 7.10, 7.12 and 7.14 it can be seen that the intensity of the swirl is higher for the lowest viscosity due to a lower pressure in the center region. This is what we expected would happen and it is a good indication for the reduction in pressure drop with increasing viscosity as seen in the experiments.

Chapter 8

Sources of Error

To find a value for the error in the experiments, the pooled variance for some of the parameters used during the tests was calculated. The method for calculating the pooled variance is described in Appendix A.1.

8.0.5 Flow Rate

The error calculations for the measurements on the flow rate is given in Table 8.1:

Table 8.1: Mean and variance values for flow rate measurements.

Test No.	Mean [m^3/h]	Variance [m^6/h^2]
1	5.35	$1.75 \cdot 10^{-4}$
2	5.34	$4.90 \cdot 10^{-5}$
3	6.12	$2.70 \cdot 10^{-5}$
4	5.41	$2.73 \cdot 10^{-4}$
5	5.42	$1.00 \cdot 10^{-6}$

This gives a pooled variance of $1.05 \cdot 10^{-4}$ m^6/h^2 and a pooled standard deviation of $1.02 \cdot 10^{-2}$ m^3/h.
The flow rate from test 1 can then be written as 5.35 ± 0.01 [m^3/h]

8.0.6 Total Efficiency

The error calculations for the total efficiency is given in Table 8.2:

Table 8.2: Mean and variance values for the total efficiencies.

Test No.	Mean	Variance
1	0.75	$7.0 \cdot 10^{-6}$
2	0.65	$4.0 \cdot 10^{-6}$
3	0.44	$1.3 \cdot 10^{-4}$
4	0.24	$3.0 \cdot 10^{-4}$
5	0.18	$3.0 \cdot 10^{-4}$

The pooled variance was $6.0 \cdot 10^{-6}$ and the pooled standard deviation was $2.4 \cdot 10^{-3}$.
The Total Efficiency for test 1 can then be given as 0.75 ± 0.0024.

8.0.7 Size Distributions

The error calculations for 50% size in the size distributions are given in Table 8.3:

Table 8.3: Mean and variance values for the size distributions at the 50% value.

Test No.	Mean [μm]	Variance [μm^2]
1	7.14	$5.32 \cdot 10^{-2}$
2	9.69	$2.59 \cdot 10^{-2}$
3	12.53	$5.71 \cdot 10^{-2}$
4	16.08	$1.56 \cdot 10^{-2}$
5	17.51	$4.00 \cdot 10^{-2}$

The pooled variance calculated was $3.84 \cdot 10^{-2}$ μm^2 and the pooled standard deviation was $1.96 \cdot 10^{-1}$ μm.
The 50% size on the size distribution curve for test 1 can then be given as 7.14 ± 0.20 μm.

8.0.8 Cut size

The error calculations for the 50% size on the grade-efficiency curves are given in Table 8.4:

Table 8.4: Mean and variance values for the cut size obtained from the grade-efficiency curves.

Test No.	Mean [μm]	Variance [μm^2]
2	15.50	$1.20 \cdot 10^{-1}$
4	30.90	1.08
5	34.08	$1.15 \cdot 10^{-1}$

The pooled variance calculated was $9.54 \cdot 10^{-1}$ μm^2 and the pooled standard deviation was $9.77 \cdot 10^{-1}$ μm.
The cut size, x_{50}, for test 2 can then be given as 15.50 ± 0.98 μm.

Chapter 9

Conclusion

An experimental rig suitable for experiments on viscous fluids was designed and commissioned with great success. The rig grants the possibility of obtaining grade-efficiency curves, volumetric flow rate of two of the material streams (where the third can be obtained by a mass balance), pressure drop and flow split distribution. By small modifications, the rig can be modified to test also other geometries, which is an important feature in the continuation.

The conclusion of the results obtained in this thesis can be listed as follows:

- Increasing the viscosity of the carrier fluid leads to an increase in the value for the cut size x_{50}.
- The sharpness of the separation tends to be better for the lowest values of the viscosities.
- Increasing the fluid viscosity leads to a decrease in the pressure drop, at least for the flow rates used in this thesis.
- An increase in fluid viscosity leads to a higher by-pass fraction R_f.

The numerical results shows that more work have to be done to fit the numerical results to the experimental ones.

Chapter 10

Further Discussion

In addition to the experimental results presented and discussed earlier, this thesis had another important part. Before the experiments could be started a test rig suitable for our purpose had to be built and tested to see that it could cope with our expectations.

When the project was started, many of the components planed for the project was already ordered or in place ready for assembly. A schematic drawing of the planed design was ready, and most things seemed ready for the assembly process. As already mentioned in Chapter 4 some of the planed equipment was evaluated to expensive or to big to serve our purpose and there was not decided how to analyze the results from the experiments.

All of this lead to challenges, and the new design proposed by the author was an important break through in the project. The new design worked exactly how we wanted it to do, except that we of course lost the ability of total capture, which was a highly wanted ability. Total capture had been done with great success by others in our research group before, but not on liquid cyclones.

When the system was tested without particles, with only water flowing in the system the measurements of the flow rate worked perfectly. The displays connected to the ultrasonic flowmeters showed a very stable flow rate, and they were quick to catch changes in the flow rate when different parameters were changed. When particles were added to the system for test 1 it was clear that the flowmeters did not handle the situation with particles very well as the displayed flow rate showed a fluctuating value. The flow rate was therefore checked by sampling a volume over a specific time.

Increasing the viscosity lead to problems with the signal on the flow meter placed after the centrifugal pump. The flow meter on the underflow worked, even though it not gave an accurate signal as the parameters for sound velocity was kept constant.

The reason that the flowmeter did not work was because very small air bubbles was being formed in the upstream tank, as the overflow disposed into the air above the level of the suspension. When pure water was used this problem did not occur because the bubbles probably escaped the exit tube in the upstream tank as the buoyancy is more effective on the bubbles in a low viscosity environment. Since the small amount of bubbles entering the cyclone was being separated and discharged through the overflow, the problem did not occur in the flowmeter placed on the underflow.

Appendix C gives an introduction to the working principle of transit time ultrasonic flowmeters. The problem with the flowmeters was that the signal quality was bad even though the signal strength was good. It is clear that solid particles will influence the signals in the flowmeter, and even though the producer of the flowmeter claimed that it

could handle a low amount of solids, the high complexity of the flowmeter makes it very vulnerable for disturbances.

As there was no alternative to the ultrasonic flowmeters at the time the experiments were done, volume sampling was done to measure the flow rates in the system. The other rig used in the PET project experienced the same problems with the ultrasonic flowmeters as the one experienced in this thesis. As mentioned in Chapter 4 the PET rig had a venturi flowmeter installed. It was connected to a differential pressure transducer and worked well for the different viscosities tested in that project. Two venturi flowmeters were ordered from the workshop and they are now ready to be installed before further tests on the system are done. This will make it much more convenient than the present situation with volume sampling.

The sucrose solution used in the experiments had a negative influence on the pressure transducers. Somewhere in between test two and test three the displayed value on the pressure displays dropped and it was clear that the something was wrong as the pressure measured at the inlet was lower than the pressure measured at the overflow. This was the reason why test number three was done at a higher flow rate than the other tests. The pressure transducers were at this point removed and replaced by manometers. Since the pressure readings from test number three was wrong the system was tuned in to the same conditions as in the experiment, and new readings were made with the new pressure devices.

Sucrose turned out to work well as a viscosity modifier. However it is noteworthy that it can get very sticky when it is in contact with a liquid free surface. As long as the sucrose solution moistures a surface it works very well, but at the areas where the suspension is in contact with air it can get sticky and not very delicate. This effect was very well noticed after the pump had been emptied during an inspection of the pipes to see if there was any accumulation of solids in the piping. After the inspection the pump would not start because of a thin layer of sucrose around the impeller. The pump had to be removed and cleaned before it would start again. After this experience, the problem did not occur again as the housing on the centrifugal pump was kept filled up with suspension.

The only equipment needed in addition to a hydrocyclone is as already mentioned a pump. In this thesis a centrifugal pump was used, and in Appendix B, a brief introduction to the effects of solid particles, slurry density and viscosity on the performance of a centrifugal pump are included. In this thesis it was preferable to investigate the influence of viscosities up to the viscosity of Mono-ethylene Glycol, which is around 16.9 cP at 25 °C. The rig showed that it was suitable for that range of viscosities, but keeping in mind the effect the viscosity has on the centrifugal pump, tests have to be performed before we can claim that the rig is suitable for viscosities much higher than what we have experienced in this thesis.

Even though sucrose can be used to obtain high viscosities due to its high solubility in water it is noteworthy that it will increase the density of the suspension significantly and that if the intension is to use the same suspension over time it will get quite sticky and indelicate to work with. Sucrose was chosen as the viscosity modifier in this thesis due to the low cost and high availability. Tests performed on aqueous glycerol solutions during the work with this thesis showed that glycerol acted Newtonian in the same way as the sucrose solution. It also has a significantly lower density then that of sucrose, 1260 kg/m^3 [49] against 1587 kg/m^3 for sucrose. That makes it better for the next experiments and

it will therefore be given as a recommendation in the further work chapter.

Another thing worth mentioned about the sucrose is that it takes time to dissolve it at higher concentrations. As the concentration went above 30 % by mass, the suspension was heated to approximately 50 °C to decrease the time needed for dissolving it. Glycerol is available in a liquid form and is very easy to mix with water.

The sedimentation balance used for the size analyses worked well for the particle sizes used in this thesis. Larger particles were also tested with the sedimentation balance, and when dissolved in water, the result came out wrong, as the height of the suspension, H, was too low. The available height is limited by the geometry of the balance pan. If experiments with higher viscosities are performed by using larger particles, this problem has to be resolved. One option that worked well when tried out is to increase the viscosity of the suspension to decrease the settling velocity of the particles.

Chapter 11

Further Work

This thesis provides valuable results on the influence the viscosity has on hydrocyclone separation performance. Still there is a long way to go before we have the knowledge to apply hydrocyclone technology in the areas that are mentioned earlier. However, with this thesis the first step by obtaining a suitable test rig that have provided us with the first results are ready, and only our imagination can limit what we are able to achieve by continuation of this project.

The results show that the experimental rig is suitable for evaluating the separation performance from viscous medias such as Mono-ethylene glycol. Even though the results are good and the rig works well, there is still room for improvement in the design and measurement techniques.

The ultrasonic flowmeters that are installed in the rig should either be removed and replaced by the venturi flowmeters that are ready to be installed, or connected in parallel with the venturies with the possibility of rerouting the flow for the possibility of comparison of the measured flow rates. The last alternative requires that the small air bubbles mentioned in the previous chapter are removed which is possible by small changes in the design.

To remove the small air bubbles, the overflow piping should be extended into the suspension. This requires a new technique to sample the overflow, and to obtain this a three-way valve should be installed so that the flow can be rerouted when the sampling is done. The same thing can be done with the underflow discharge to get a more convenient sampling location.

Since the target of this thesis was to evaluate the separation from liquids with the same viscosity as Mono-ethylene glycol, the next step should be to design a cyclone that provides good results on such systems. Firstly a CFD model that replicates the results should be obtained, and then the CFD model can be used to test the performance on other geometries.

Starting the next phase of this project by doing CDF on new geometries allows us to collect important information on what parameters in the hydrocyclone design that have the most influence on the results. This is necessary as making new geometries are both time consuming and expensive. When a wide range of geometrical variables has been investigated by CFD, the results can be used as input to a factorial design for an experimental hydrocyclone.

A new hydrocyclone consisting of interchangeable parts should be produced. By using interchangeable parts, a lot of the work involved in making the hydrocyclones

is avoided and the production time will also be greatly reduced. The present setup has a collection chamber made of plexiglass, which is a transparent material. Using a transparent material allows visualization of the flow, and therefore making the parts out of plexiglass is a good idea for the further work.

While the CFD analyses of the design parameters are done, there is also possible to do experiments on even higher viscosities than the ones tested in this thesis. Using glycerol as a viscosity modifier allows high viscosities when the concentration of glycerol is high, and together with a coarser particle suspension results from such experiments can be obtained in a reasonable amount of time.

Appendix A

Variance and Standard Deviation

Experimental results often contain some sort of error. If a sample is measured a given number of times, and the results differ from each other, a stochastic variable is observed [50]. That means that the variable is changing randomly.

To sum up the basic measures for the error, we will first start by introducing the mean value. The mean value is a measure for the average value obtained from a series of experiments. The formula for the mean is given in Equation (A.1):

$$\overline{x} = \frac{\sum_{i=1}^{n} x_i}{n} \tag{A.1}$$

where n is the number of measurements, and x_i is the value for experiment number i.

To measure the spread or the precision of the measurements the most common measures are the variance and the standard deviation. If the variance is a known size without uncertainty, it is denoted by the symbol σ^2. If we have an empirical variance, it is denoted by s^2. The standard deviation is equal to the square root of the variance. The expression for the variance is given in Equation (A.2):

$$s^2 = \frac{\sum_{i=1}^{n} (x_i - \overline{x})^2}{n-1} \tag{A.2}$$

The reason for dividing by $(n-1)$ instead of n in equation A.2 is because the mean value is in the formula. When the mean is calculated, the sum of x is divided by n. Then we loose one degree of freedom, and therefore have one degree of freedom less than n, and have to divide by $(n-1)$.

A.1 Pooled Variance

In statistics it is common that data is collected for a dependent variable over a range of values for an independent variable. In order to get a small variance for the depending variable, numerous repeated tests are required at each value of the independent variable, and the expense of the testing may become prohibitive. By using a pooled variance, reasonable estimates of variance can be determined after repeating each test at a particular independent variable only a few times. It is a method for estimating the variance by pooling the variance from several different samples taken in different circumstances where the mean may vary between the samples, but the true variance is assumed to remain the same. The formula for the pooled variance is given by:

$$s_p^2 = \frac{\sum_{i=1}^{k} \left((n_i - 1)\, s_i^2 \right)}{\sum_{i=1}^{k} (n_i - 1)} \tag{A.3}$$

where s_p^2 is the pooled variance, n_i is the sample size of sample i, s_i^2 is the variance of sample i and k is the number of samples being combined.

The pooled standard deviation is defined in the same way as before, i.e. as the square root of the pooled variance.

Appendix B

Effects of Slurry Properties in Centrifugal Pumps

As mentioned earlier in this thesis, the only equipment needed to be able to operate a hydrocyclone is a pump. The following is a brief review of how the effects of solid particles, density and viscosity of the slurry influences the performance of a centrifugal pump which is the type used in the experiments in this thesis.

B.1 Solid Particles

The effect of solid particles on pump performance is not yet very well described [51]. However, it contributes to the two other phenomena's that we will cover here, namely the density and the viscosity of the slurry. Since the slurry containing particles is denser than water it therefore appears attractive to use the behavior of a denser fluid as a model of slurry behavior although it may be an approximate one. The presence of solid particles introduces more complicated effects than those we will find in a simple fluid with increased viscosity. Although there are some rough qualitative similarities between slurry flow and the flow of a fluid with both increased density and viscosity compared to water.

B.2 Effect of Density

If the fluid density is changed while the viscosity is kept constant, the affinity laws provide a direct method of evaluating the results [51]. The affinity laws are used for point-to-point transfer of test data for one pump size and shaft speed to plot characteristic curves for a pump with another size or speed. At a given discharge, where the size of the pump and the speed is kept constant, the internal flow characteristics within the pump are unchanged. The same is the situation for the efficiency and also the head, when measured in terms of height of the fluid being pumped. If the relative density of the fluid is S_f, the resulting power requirement is S_f times that needed to pump water at an equal flow rate.

On geometrically similar machines, the effect of changed density does not depend on pump size. For a pump of given size and rotational speed, the best efficiency point, BEP, is not influenced by changing the density.

B.3 Effect of Viscosity

If the fluid density is kept constant and the viscosity is increased, the head and efficiency of the pump is lowered, and more power is needed to maintain a constant capacity [51]. The effect is shown in Figure B.1:

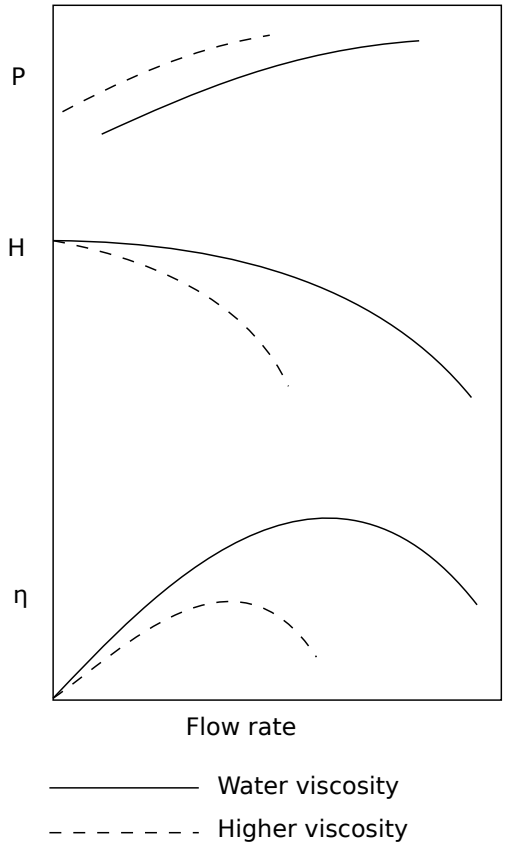

Figure B.1: Effect on fluid viscosity on pump characteristics (schematic).

where P denotes the power requirement, H denotes the Head and η denotes the efficiency.

The effects of increased viscosity are more pronounced at higher flow rates. As a result of that, the flow rate at BEP tends to become smaller as the viscosity is increased. The shift in BEP may not always be significant, but one other effect that is of great importance is the scale effect. An increase in viscosity has a higher influence on small pumps than on large ones.

Appendix C

Ultrasonic Transit Time Flowmeter

An ultrasonic transit time flowmeter may be of a wetted sensor type or a clamp on type [52]. The first type is suitable for single-phase fluids while the latter is preferred for dirty, hostile or multiphase flows. This is simply because the first type have the piezoelectric transducers in contact with the fluid. Figure C.1 below show one of the possible transducer configurations available.

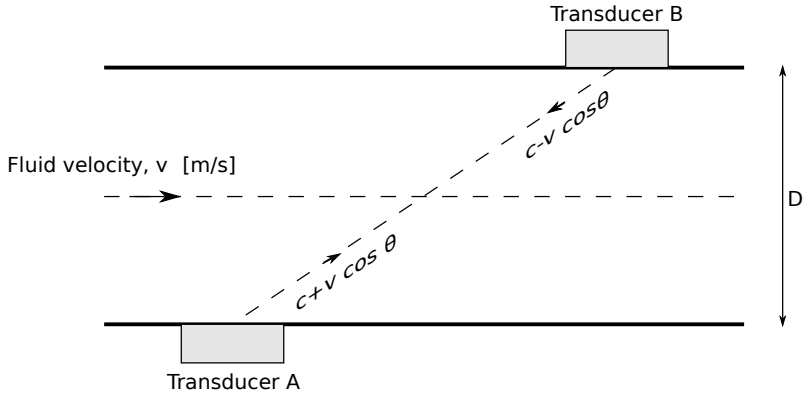

Figure C.1: Possible transducer configuration for an ultrasonic transit time flowmeter (schematic).

Firstly, transducer B acts as transmitter and sends a pulse of ultrasound to transducer A acting as a receiver. The transit time from B to A equals [52]:

$$T_{BA} = \frac{L}{c - v\ cos\ \theta} \tag{C.1}$$

where the length of the path L is given by:

$$L = \frac{D}{sin\ \theta} \tag{C.2}$$

and c is the velocity of sound in the fluid.

If A acts as a transmitter and sends a pulse to B acting as a receiver the corresponding transit time from A to B is equal to:

$$T_{AB} = \frac{L}{c + v\ cos\ \theta} \tag{C.3}$$

Subtracting Equation (C.3) from Equation (C.1) then gives the differential transit time ΔT:

$$\Delta T = T_{BA} - T_{AB} = \frac{D}{sin\,\theta}\left(\frac{L}{c - v\,cos\,\theta} - \frac{1}{c + v\,cos\,\theta}\right) = \frac{2\,D\,cot\,\theta v}{c^2\left(1 - \frac{v^2}{c^2}\,cos^2\theta\right)} \tag{C.4}$$

The ratio v/c is typically 10^{-2} so that $(v^2/c^2)\,cos^2\theta \ll 1$ and Equation (C.4) reduces to:

$$\Delta T = \frac{2\,D\,cot\,\theta}{c^2} v \tag{C.5}$$

From Equation (C.5) we can see that the differential transit time, ΔT, is proportional to the fluid velocity v. Since the differential transit time normally is very small, a very low error in ΔT is necessary to obtain a low measurement error. Often this is obtained by using a sing around system where transducer A and B are continuously switched between transmitter and receiver mode. Then the differential transit time is converted into a frequency difference equal to:

$$\Delta f = (sin\,2\,\theta/D)v \tag{C.6}$$

which is independent of sound velocity c.

Bibliography

[1] Petroleumstilsynet (Ptil), Statens forurensningstilsyn (SFT), Sosial- og helsedirektoratet (SHdir). *Forskrift om utføring av aktiviteter i petroleumsvirksomheten (aktivitetsforskriften)*, x-ii utslipp til ytre miljø, § 59 utslipp av kaks, sand og faste partikler edition, January 2002. 1.1

[2] Folas G K, Kontogeorgis G M, Michelsen M L, and Stenby E H. Vapor-liquid, liquid-liquid and vapor-liquid-liquid equilibrium of binary and multicomponent systems with meg: Modeling with the cpa eos and an eos/ge model. *Fluid Phase Equilibria*, 249(1-2):67–74, 11 2006. 1.2

[3] Mohanty S and Das B. Optimization studies of hydrocyclone for beneficiation of iron ore slimes. *Mineral processing and extractive metallurgy review*, 31(2):86–96, 2010. 1.2.2

[4] Zhao L, Jiang M, and Feng L. Experimental study on the separation performance of air-injected de-oil hydrocyclones. *Chemical Engineering Research and Design*, 88(5-6):772–778, 6 2010. 1.2.2

[5] Klima M S and Kim B H. Dense-medium separation of heavy-metal particles from soil using a wide-angle hydrocyclone. *Journal of environmental science and health part a-toxic/hazardous substances and environmental engineering*, 33(7):1325–1340, 1998. 1.2.2

[6] Barbosa R, Lapa N, Boavida D, Lopes H, Gulyurtlu I, and Mendes B. Co-combustion of coal and sewage sludge: Chemical and ecotoxicological properties of ashes. *Journal of Hazardous Materials*, 170(2-3):902–909, 10 2009. 1.2.2

[7] Adupeasah S P, Diosady L L, and Rubin L J. A multistage hydrocyclone stirred-tank system for countercurrent extraction of canola oil. *Journal of the american oil chemists society*, 70(8):755–762, 8 1993. 1.2.2

[8] Bretney E. *Water Purifier*, us patent 453,105 edition, 1891. 1.2.3

[9] Lynch A J and Rowland C A. *The History of Grinding*. SME, Littleton, Colorado, USA, 2005. 1.2.3

[10] Hoffmann A C and Stein L E. *Gas Cyclones and Swirl Tubes: Principles, Design and Operation*. Number Second Edition. Springer-Verlag Berlin Heidelberg, Berlin, Heidelberg, 2008. 2.1, 2, 2.1, 2.1, 2.1.1, 2.1.2, 2.3.2, 2.4, 2.4, 2.4.1, 2.4.1, 2.5, 2.5, 2.5, 2.5, 2.5.1, 2.6.1, 2.6.3, 2.6.3, 2.6.6, 2.8.2, 2.8.2, 2.8.2, 2.11, 2.11.3

[11] Rushton A, Ward A S, and Holdich R G. *Solid-liquid filtration and separation technology*. Number 2nd, completely rev. ed. Wiley-VCH, Weinheim, 2000. 2.1.1, 2.2, 2.6.5, 2.7.1

[12] Olson T J and Turner P A. Hydrocyclone selection for plant design. *Mineral Processing Plant Design, Operating Practices and Control Proceedings*, Vol 1:880–893, 2002. 2.2, 2.7, 2.7.1, 2.7.2, 2.7.2, 2.7.3, 2.7.4

[13] Svarovsky L. *Solid-liquid separation*. Number 4th ed. Butterworth-Heinemann, Boston, 2000. 2.2.1, 2.3, 2.3.1, 2.3.2, 2.3.3, 2.5, 2.6.5, 2.6.6, 2.7.1, 2.7.2, 2.7.2, 2.8.1, 2.8.3, 2.8.4, 2.8.5, 2.8.6

[14] Bradley D. *The hydrocyclone*. Pergamon Press, Oxford, 1965. 2.3, 2.3.1, 2.3.4, 2.3.5, 2.3.6, 2.3.7

[15] Bird R B, Stewart W E, and Lightfoot E N. *Transport phenomena*. Number 2nd ed. Wiley, New York, 2002. 2.4, 2.5

[16] Clift R, Grace J R, and Weber M E. *Bubbles, drops, and particles*. Academic Press, New York, 1978. 2.5, 2.5

[17] Crowe C T, Tsuji Y, and Sommerfeld M. *Multiphase flows with droplets and particles*. CRC Press, Boca Raton, Fla., 1998. 2.5, 5.1.1, 5.1.1

[18] Rietema K and Verver C G. *Cyclones in industry*. Elsevier, Amsterdam, 1961. 2.6

[19] Svarovsky L. *Solid-liquid separation processes and technology*. Elsevier, Amsterdam, 1985. 2.6.1, 2.6.2, 2.6.3, 2.6.3, 2.6.5

[20] Svarovsky L and Thew M T. *Hydrocyclones: analysis and applications*. Kluwer Academic Publishers, Boston, 1992. 2.6.4

[21] Tue Nenu R K and Yoshida H. Comparison of separation performance between single and two inlets hydrocyclones. *Advanced Powder Technology*, 20(2):195–202, 3 2009. 2.7.2

[22] Martìnez L F, Lavìn A G, Mahamud M M, and Bueno J L. Vortex finder optimum length in hydrocyclone separation. *Chemical Engineering and Processing: Process Intensification*, 47(2):192–199, 2 2008. 2.7.3

[23] Coelho M A Z and Medronho R A. A model for performance prediction of hydrocyclones. *Chemical Engineering Journal*, 84(1):7–14, 9 2001. 2.8.1

[24] Rietema K. Performance and design of hydrocyclones, parts I-IV. *Chemical Engineering Science*, 15(3-4):298–325, 9 1961. 2.8.1

[25] McCabe W L, Harriott P, and Smith J C. *Unit operations of chemical engineering*. Number 7th ed. McGraw-Hill, Boston, 2005. 2.9, 2.9.1, 2.9.1, 2.10

[26] M. Mathlouthi and P. Reiser. *Sucrose: properties and applications*. Blackie, London, 1995. 2.10

[27] Savins J G. Shear thickening phenomena in poly(vinyl)alcohol-borate complexes. *Rheologica Acta*, 7(1):87–93, 1968. 2.10

[28] Ferziger J H and Perić M. *Computational methods for fluid dynamics*. Number 3rd, rev. ed. Springer, Berlin, 2002. 2.11.1, 2.11.2, 2.11.2, 2.11.2

[29] Wesseling P. *Principles of computational fluid dynamics*. Springer, Berlin, 2001. 2.11.2

[30] Sagaut P. *Large Eddy Simulation for Incompressible Flows: An Introduction*. Number Third Edition. Springer-Verlag Berlin Heidelberg, Berlin, Heidelberg, 2006. 2.11.2

[31] Smagorinsky J. General circulation experiments with the primitive equations. *Monthly Weather Review*, 91(3):99–164, 1963. 2.11.2

[32] Deardorff J W. A numerical study of three-dimensional turbulent channel flow at large reynolds numbers. *Journal of Fluid Mechanics*, 41(02):453–480, 1970. 2.11.2

[33] Emami S, Tabil L G, and Tyler R T. Performance comparison of two media during starch–protein separation of chickpea flour using a hydrocyclone. *Journal of Food Process Engineering*, 33(4):728–744, 2010. 3.1

[34] Liancheng R, Zheng L, Gongxiang Z, and Shihui W. A comparative study of the flow field of high viscosity media in conventional/rotary hydrocyclones. *Petroleum Science*, 4(1):81–85, 2007. 3.1

[35] Guo J, Gong D, Zhang J, WANG L, Zheng Z, and Li K. Studies on mechanism of sand removal from crude oil. *Journal of Hydrodynamics, Ser. B*, 18(3, Supplement 1):394–399, 7 2006. 3.1

[36] Wang L, Zheng Z, Guo J, Zhang J, and Tang C. Investigation on separation efficiency of liquid/solid hydrocyclone. *Journal of Hydrodynamics, Ser. B*, 18(3, Supplement 1):400–404, 7 2006. 3.1

[37] Agar G E and Herbst J A. The effect of fluid viscosity on cyclone classification. *Trans. AIMS 235*, pages 145–149, 1966. 3.1, 3.2

[38] Kawatra S K, Bakshi A K, and Rusesky M T. Effect of viscosity on the cut (d50) size of hydrocyclone classifiers. *Minerals Engineering*, 9(8):881–891, 8 1996. 3.1

[39] Trinh T, Monge J J, and Chrusciel W A. Efficiency of particle removal from viscous liquids with a hydroclone. *NASA STI/Recon Technical Report N*, 77, 1976. 3.2

[40] Galmarini M V, Baeza R, Sanchez V, Zamora M C, and Chirife J. Comparison of the viscosity of trehalose and sucrose solutions at various temperatures: Effect of guar gum addition. *LWT - Food Science and Technology*, 44(1):186–190, 1 2011. 3.3

[41] Boguń M and Mikołajczyk T. Sorption and tensile strength properties of selected fibres of cupric alginate. *FIBRES & TEXTILES in Eastern Europe*, Vol. 16(No 4(69)):39–42, 2008. 3.3

[42] Mousavian S M and Najafi A F. Influence of geometry on separation efficiency in a hydrocyclone. *Archive of applied mechanics*, 79(11):1033–1050, 11 2009. 3.4

[43] Lim E W C, Chen Y, Wang C, and Wu R. Experimental and computational studies of multiphase hydrodynamics in a hydrocyclone separator system. *Chemical Engineering Science*, 65(24):6415–6424, 12 2010. 3.4

[44] Brennan M S, Narasimha M, and Holtham P N. Multiphase modelling of hydrocyclones - prediction of cut-size. *Minerals Engineering*, 20(4):395–406, 4 2007. 3.4

[45] Stairmand C J. The design and performance of cyclone separators. *Transactions of the Institution of Chemical Engineers*, 29:356–383, 1951. 4.3.2

[46] Merkus H G, Bellantone M, and Scarlett B. *Particle Size Measurements: Fundamentals, Practice, Quality*. Springer Netherlands, Dordrecht, 2009. 5.1

[47] Khan A U, Mahmood N, and Bazmi A A. Direct comparison between rotational and extrusion rheometers. *Materials Research*, 12:477 – 481, 2009. 5.2.1, 5.2.1

[48] Kawatra S K, Bakshi A K, and Rusesky M T. The effect of slurry viscosity on hydrocyclone classification. *International Journal of Mineral Processing*, 48(1-2):39–50, 11 1996. 7.1.4

[49] Adamenko I I, Bulavin L A, Ilyin V, Zelinsky S A, and Moroz K O. Anomalous behavior of glycerol-water solutions. *Journal of Molecular Liquids*, 127(1-3):90–92, 8 2006. 10

[50] Helbæk M. *Statistikk for kjemikere*. Tapir Akademisk Forlag, Trondheim, Norway, 2001. A

[51] Wilson K C, Addie G R, Clift R, and Sellgren A. *Slurry Transport Using Centrifugal Pumps*. Number Third Edition. Springer Science+Business Media, Inc., Boston, MA, 2006. B.1, B.2, B.3

[52] Bentley J P. *Principles of Measurement Systems*. Number 4th ed. Pearson/Prentice Hall, Harlow, 2005. C, C